POLITECNICO DI MILANO

Scuola di Ingegneria Industriale e dell'Informazione
Corso di Laurea Magistrale in Ingegneria Aeronautica

SKIN FRICTION DRAG REDUCTION IN A TURBULENT CHANNEL FLOW VIA PULSATING FORCING

Relatore: Prof. Maurizio QUADRIO

Tesi di laurea di:
Alessandro MONTI
Matr. 800912

Anno Accademico 2013 - 2014

Dedicata ai miei cari.

Ringraziamenti

Desidero ringraziare tutti coloro che hanno dato un contributo alla realizzazione di questa tesi. Innanzitutto ringrazio il Prof. Quadrio per la sua disponibilità, i suoi insegnamenti e consigli anche per il futuro.

Un ringraziamento speciale va inoltre ai miei genitori, che mi hanno sostenuto in tutto e per tutto senza farmi mai mancare nulla, alle mie nonne che mi sopportano sempre, e a mio fratello che ha sempre creduto in me.

Un pensiero a tutti i miei amici dell'università, che hanno reso questi anni indimenticabili, mi auguro che questa bella amicizia continui anche al di fuori di qui. Grazie ovviamente ai miei amici di sempre che hanno sempre mostrato interesse nel mio lavoro e mi hanno fatto svagare in momenti di grande sforzo.

Alessandro

Sommario

L'effetto dell'applicazione di una forzante periodica su una corrente turbolenta all'interno di un canale piano è stato studiato numericamente attraverso l'utilizzo della simulazione diretta (DNS). L'obiettivo di questo studio preliminare è ottenere una riduzione di resistenza e un risparmio netto di energia. La forzante, ossia l'accelerazione fornita alla corrente nel canale, è stata imposta sotto forma di gradiente di pressione (spazialmente uniforme) lungo la direzione della corrente. La sua ampiezza è stata modulata nel tempo in modo da applicare mediamente nel periodo la stessa forzante impressa alla corrispettiva corrente non controllata. Il numero di Reynolds della corrente, basato sulla velocità d'attrito e su metà altezza del canale (Re_τ), è posto pari a 180. Iwamoto *et al.* hanno condotto uno studio simile [19] a $Re_\tau = 110$; la differenza sostanziale risiede nel fatto che il loro controllo richiede l'utilizzo di un sistema attivo di recupero dell'energia per imporre alla corrente, mediamente nel periodo, la stessa accelerazione del corrispettivo caso non controllato.

Uno studio parametrico è stato condotto per analizzare l'andamento della riduzione di resistenza e del consumo di energia al variare del periodo di azione della forzante e del duty-cycle (ovvero la frazione di tempo in cui la forzante rimane accesa).

Sono stati ottenuti importanti risultati in termini di riduzione d'attrito e di risparmio di energia attraverso questa tecnica, aprendo di fatto la possibilità di approfondire l'argomento per un suo futuro utilizzo.

Parole chiave: riduzione di resistenza, risparmio di energia, DNS, canale piano, corrente pulsata.

Abstract

In this study, drag reduction and power saving of pulsating turbulent channel flow have been numerically examined. Spatially uniform streamwise pressure gradient is modulated in time to generate the pulsating flow; its cycle-averaged value is constrained to be equal to the respective uncontrolled case one. The cycle-averaged Reynolds number, based on skin friction velocity and half channel height (Re_τ), is set to be 180. A similar work was conducted by Iwamoto *et al.* in [19]. They studied drag reduction and power saving of a pulsating channel flow at $Re_\tau = 110$. Their simulation is driven by a spatially uniform streamwise pressure gradient that provides an active energy recovery system to respect the same constraint on the forcing term used in this work.

The pulsating pumping effect has been examined through Direct Numerical Simulation (DNS): a parametric study has been carried out in order to investigate the trend of drag reduction and power saving rates, varying forcing period and duty-cycle. Important results in terms of drag reduction and power saving have been obtained through this control technique, opening the possibility to deepen this topic in future work.

Key words: drag reduction, power saving, DNS, channel flow, pulsating flow.

Estratto della tesi in lingua italiana

La turbolenza ha una grande importanza in molti processi fisici che coinvolgono i fluidi. La corrente di un gas o di un liquido in un tubo, la corrente attorno ad un aereo, i processi di miscelamento che avvengono all'interno dei motori, lo strato limite e la scia attorno a corpi tozzi, i fenomeni atmosferici e la corrente sanguigna all'interno del corpo umano sono solo alcuni esempi della grande varietà di situazioni di vita quotidiana in cui si incontrano le correnti turbolente. Ecco spiegato il forte interesse dei ricercatori nella fluidodinamica e nella turbolenza.

La profonda comprensione delle correnti turbolente è tutt'oggi un grande problema irrosolto della fisica classica. La difficoltà di formulare un'unica e semplice definizione di turbolenza già fornisce un'idea della sua complessità. È un ramo critico della fluidodinamica, dove molti sforzi nella ricerca devono ancora essere effettuati, dove anche lo sviluppo di strumenti di analisi, sia teorici, che sperimentali, che numerici può risultare molto difficile.

Negli ultimi vent'anni si è assistito al rapido sviluppo della ricerca su un particolare tema della fluidodinamica: il flow control. Questo ramo riguarda la possibilità di cambiare le caratteristiche di una corrente turbolenta per ottenere dei vantaggi dal punto di vista ingegneristico. Nel campo dell'ingegneria aerospaziale, i principali obiettivi sono la riduzione della resistenza, l'aumento della portanza, l'aumento della miscelazione all'interno dei motori e l'eliminazione del rumore. Per raggiungerli, sono state sviluppate negli ultimi anni numerose tecniche, classificabili in attive o passive, a seconda della richiesta o meno di energia dall'esterno.

Tra gli obiettivi appena visti sopra, la riduzione di resistenza è quello principale di questa tesi. Per ottenerlo si è valutato il possibile utilizzo delle correnti turbolente pulsate, le quali sono caratterizzate da instazionarietà ottenuta attraverso la sovrapposizione di un forzamento periodico nel tempo alla corrente stazionaria. La loro rilevanza può essere trovata in molte applicazioni ingegneristiche: esempi vanno dalle correnti di tipo biologico alle correnti di tipo ambientale. Nonostante ciò, gli studi condotti su questo tipo di correnti sono stati molto pochi, a causa della loro elevata complessità da un punto di vista fisico. Il poco si riduce quasi al nulla se si considera il loro utilizzo nell'ambito del flow control.

In questa tesi, la corrente pulsata viene generata attraverso l'applicazione di un particolare tipo di forzamento, che imprime, periodicamente nel tempo, ad una corrente turbolenta all'interno di un canale piano, a numero di Reynolds basato sulla velocità d'attrito e su metà altezza del canale, Re_τ, pari a 180, una violenta accelerazione per breve tempo e, successivamente, spegnendo il forzamento, una decelerazione altrettanto violenta. Tutto questo viene fatto in modo tale da imporre mediamente nel periodo la stessa forzante impressa alla corrispettiva corrente non controllata. La forzante è applicata in termini di gradiente di pressione, spazialmente uniforme, costante a tratti nel tempo, lungo la direzione della corrente.

Per verificare come variano i parametri di riduzione della resistenza e di risparmio di energia, è stato quindi condotto uno studio parametrico variando il periodo di forzamento della corrente e il duty-cycle della forzante (ovvero la frazione di tempo in cui la forzante rimane accesa). Non essendo utilizzato nessuno strumento di controllo esterno rispetto al caso non controllato, questa tecnica può essere classificata come passiva. Nonostante ciò, bisogna tenere in conto che il consumo di energia della pompa per muovere la corrente nel canale non sarà lo stesso del caso non controllato corrispondente.

Uno studio simile è stato condotto da Iwamoto *et al.* in [19] i quali hanno analizzato il comportamento di una corrente turbolenta a $Re_\tau = 110$, all'interno di un canale piano, sottoposta ad un forzamento periodico imposto attraverso un'onda quadra di gradiente di pressione lungo la direzione della corrente. La differenza sostanziale, al di là del numero di Reynolds, risiede nel fatto che il loro controllo richiede l'utilizzo di un sistema attivo di recupero dell'energia per imporre, mediamente nel periodo, la stessa forzante impressa alla corrispettiva corrente non controllata. Per cui quando viene valutata la riduzione di resistenza, bisogna tenere conto del costo del controllo.

Lo studio presentato in questa tesi è stato sviluppato attraverso l'uso di un codice di simulazione diretta, sviluppato dal Professor Maurizio Quadrio e dal Professor Paolo Luchini, implementato con la forzante instazionaria descritta in precedenza.

Il dominio di calcolo scelto è abbastanza grande ($L_x = 4\pi\delta$, $L_y = 2\delta$, $L_z = 2\pi\delta$). Essendo infatti uno studio preliminare, non si era certi del funzionamento di questa tecnica di controllo e la scelta di un dominio più piccolo avrebbe potuto portare a risultati fuorvianti. Ciò ha incrementato notevolmente il costo computazionale delle simulazioni. Si è comunque cercato di risparmiare da questo punto di vista discretizzando la direzione normale alla parete con soli 100 punti e, per verificarne l'influenza sui risultati, sono state avviate due simulazioni su un dominio più piccolo rispetto a quello presentato in precedenza in lunghezza e larghezza, ma con uguale dimensione L_y, discretizzata prima con 100 e poi con 200 punti. Da un confronto tra le quantità ottenute dalle due simulazioni, si evince che i risultati sono scarsamente influenzati dal numero di punti di discretizzazione almeno da un punto di vista qualitativo. Comunque il costo computazionale delle simulazioni rimane molto alto e per questo motivo, date le tempistiche stringenti, lo studio parametrico è stato troncato dopo soli dieci cicli (cinque per il caso con periodo minore poiché fino a quel momento non sono stati ottenuti risultati promettenti).

Nonostante la limitata quantità di dati analizzata, sono stati ottenuti risultati di rilievo. Infatti, considerando ogni singolo ciclo, è stata raggiunta una riduzione di resistenza pari addirittura al 74.4% e un risparmio di energia pari al 67.1% per il caso con periodo pari a $T^+ = 14400$ e duty-cycle $\zeta = 2.50\%$. Considerando invece la media su tutti i cicli utili (escludendo il primo ciclo che è di transizione) sono stati ottenuti risultati decisamente più bassi in termini di riduzione della resistenza e di risparmio di energia, ma comunque positivi, soprattutto per le simulazioni con periodi maggiori. Inoltre, poiché le simulazioni sono state troncate dopo una decina di cicli, non è detto che la corrente ottenuta sia a regime, per cui il valore di riduzione d'attrito e di risparmio di energia potrebbe tendere ad un valor medio ben maggiore di quello ottenuto.

List of Figures

1 Imposed pressure gradient P_x, normalized with the uncontrolled field value P_{x0} vs time normalized with the forcing period T. Duty-cycle is imposed equal to $\zeta = 10.00\%$. 24

1.1 Classification scheme of flow control methods. Figure taken from [11]. 28

1.2 Control loops for active flow control. Figure taken from [11]. . . . 29

1.3 Pumping energy vs inconvenience (operational time) for different input conditions. Here $()^*$ indicates dimensional quantities. Figure taken from [8]. 31

1.4 Total energy vs inconvenience (operational time) for different input conditions. Here $()^*$ indicates dimensional quantities. Figure taken from [8]. 32

3.1 Channel flow. Figure taken from [38]. 42

3.2 Negative pressure gradient normalized with the uncontrolled field value vs time normalized with the forcing period T. For the present case, duty-cycle ζ is equal to 2.50%. The red curve represents the forcing term of Iwamoto *et al.* [19], whereas the green curve represents the uncontrolled flow. 44

4.1 Flow rate Q normalized with the uncontrolled field value Q_0 vs time normalized with forcing period T. This figure shows a comparison (for one chosen cycle) of the effect of the duty-cycle ζ for each forcing period. Top: $T^+ = 3600$ during the V cycle. Middle: $T^+ = 10800$ during the X cycle. Bottom: $T^+ = 14400$ during the X cycle. 52

4.2 Streamwise shear stress τ_{w} at $y = 0$ normalized with the uncontrolled field value $\tau_{\mathrm{w}0}$ vs time normalized with forcing period T. This figure shows a comparison (for one chosen cycle) of the effect of duty-cycle ζ for each forcing period studied. Top: $T^+ = 3600$ during the V cycle. Middle: $T^+ = 10800$ during the X cycle. Bottom: $T^+ = 14400$ during the X cycle. 53

4.3 Re_b vs Re_c. The markers help understanding flow phases during forcing cycle. They will be held the same in section 4.3. 55
4.4 Top: mean velocity profile in semi-logarithmic scale of present uncontrolled case and Vreman *et al.* simulation [62] vs wall-normal coordinate. Bottom: turbulent fluctuations of present uncontrolled case (black curves) and Vreman *et al.* simulation [62] (red curves) vs wall-normal coordinate. 58
4.5 Streamwise flow rate normalized with the uncontrolled field value Q_0 vs time normalized with the forcing period T. 59
4.6 Top: mean velocity profiles during forcing period vs wall-normal coordinate. Bottom: mean velocity profiles during the rise of the flow instability vs wall-normal coordinate. The black curves (kn1 and kn2) represent the flow condition just before the knee, whereas the gray ones (kn3 and kn4) the condition soon after. For both figures, the green curve refers to uncontrolled flow. 60
4.7 Cycle-averaged mean velocity profile in semi-logarithmic scale vs wall-normal coordinate. The green curve refers to uncontrolled flow. 61
4.8 RMS of the diagonal components of Reynolds stress tensor during forcing period vs wall-normal coordinate. The left part is normalized with ${u_{\tau}}_0^2$, whereas the right one with instantaneous u_τ^2. The green curve refers to uncontrolled flow. The legend, that is the same of the top picture of figure 4.6, here has been omitted to lighten the image. 63
4.9 Focus around the knee: RMS of the diagonal components of Reynolds stress tensor during forcing period, vs wall-normal coordinate. The left part is normalized with ${u_{\tau}}_0^2$, whereas the right one with instantaneous u_τ^2. The green curve refers to uncontrolled flow. The legend, that is the same of the bottom picture of figure 4.6, here has been omitted to lighten the image. 64
4.10 Off-diagonal components of Reynolds stress tensor during forcing period vs wall-normal coordinate. The left part is normalized with ${u_{\tau}}_0^2$, whereas the right one with instantaneous u_τ^2. The green curve refers to uncontrolled flow. The legend, that is the same of the top picture of figure 4.6, here has been omitted to lighten the image. . 65
4.11 Focus around the knee: off-diagonal components of Reynolds stress tensor varying the time phase vs wall-normal coordinate. The left part is normalized with ${u_{\tau}}_0^2$, whereas the right one with instantaneous u_τ^2. The green curve refers to uncontrolled flow. The legend, that is the same of the bottom picture of figure 4.6, here has been omitted to lighten the image. 66
4.12 Streamwise shear stress vs wall-normal coordinate. Here, tss stands for total shear stress and Rss for Reynolds component shear stress. The green curve refers to uncontrolled flow. 67

4.13 Streamwise shear stress during forcing period vs wall-normal coordinate. The bottom figure shows the quantities around the knee. The green curve refers to uncontrolled flow. 68

A.1 Flow rate normalized with the uncontrolled field value Q_0 vs time normalized with the forcing period T. 72
A.2 Turbulent kinetic energy per unit mass integrated over the wall-normal direction $K = \int_0^2 k \,\mathrm{d}y$, normalized with the uncontrolled field value K_0 vs time normalized with the forcing period T. . . . 72
A.3 Streamwise shear stress at $y = 0$, normalized with the uncontrolled field value $\tau_{\mathrm{w}0}$ vs time normalized with the forcing period T. . . . 73
A.4 Negative streamwise shear stress at $y = 2$, normalized with the uncontrolled field value $-\tau_{\mathrm{w}0}$ vs time normalized with the forcing period T. 73
A.5 Flow rate normalized with the uncontrolled field value Q_0 vs time normalized with the forcing period T. This figure shows its trend during time history for each couple of parameters (ζ,$T^+ = 3600$). 74
A.6 Flow rate normalized with the uncontrolled field value Q_0 vs time normalized with the forcing period T. This figure shows its trend during time history for each couple of parameters (ζ,$T^+ = 3600$). 75
A.7 Streamwise shear stress at $y = 0$, normalized with the uncontrolled field value $\tau_{\mathrm{w}0}$ vs time normalized with the forcing period T. This figure shows its trend during time history for each couple of parameters (ζ,$T^+ = 3600$). 76
A.8 Streamwise shear stress at $y = 0$, normalized with the uncontrolled field value $\tau_{\mathrm{w}0}$ vs time normalized with the forcing period T. This figure shows its trend during time history for each couple of parameters (ζ,$T^+ = 3600$). 77
A.9 Negative streamwise shear stress at $y = 2$, normalized with the uncontrolled field value $-\tau_{\mathrm{w}0}$ vs time normalized with the forcing period T. This figure shows its trend during time history for each couple of parameters (ζ,$T^+ = 3600$). 78
A.10 Negative streamwise shear stress at $y = 2$, normalized with the uncontrolled field value $-\tau_{\mathrm{w}0}$ vs time normalized with the forcing period T. This figure shows its trend stress during time history for each couple of parameters (ζ,$T^+ = 3600$). 79
A.11 Turbulent kinetic energy per unit mass integrated over the wall-normal direction $K = \int_0^2 k \,\mathrm{d}y$, normalized with the uncontrolled field value K_0 vs time normalized with the forcing period T. This figure shows its trend during time history for each couple of parameters (ζ,$T^+ = 3600$). 80

A.12 Turbulent kinetic energy per unit mass integrated over the wall-normal direction $K = \int_0^2 k \, \mathrm{d}y$, normalized with the uncontrolled field value K_0 vs time normalized with the forcing period T. This figure shows its trend during time history for each couple of parameters (ζ,$T^+ = 3600$). 81

A.13 Flow rate normalized with the uncontrolled field value Q_0 vs time normalized with the forcing period T. This figure shows its trend during time history for each couple of parameters (ζ,$T^+ = 10800$). 82

A.14 Flow rate normalized with the uncontrolled field value Q_0 vs time normalized with the forcing period T. This figure shows its trend during time history for each couple of parameters (ζ,$T^+ = 10800$). 83

A.15 Streamwise shear stress at $y = 0$, normalized with the uncontrolled field value τ_{w0} vs time normalized with the forcing period T. This figure shows its trend during time history for each couple of parameters (ζ,$T^+ = 10800$). 84

A.16 Streamwise shear stress at $y = 0$, normalized with the uncontrolled field value τ_{w0} vs time normalized with the forcing period T. This figure shows its trend during time history for each couple of parameters (ζ,$T^+ = 10800$). 85

A.17 Negative streamwise shear stress at $y = 2$, normalized with the uncontrolled field value $-\tau_{\mathrm{w0}}$ vs time normalized with the forcing period T. This figure shows its trend during time history for each couple of parameters (ζ,$T^+ = 10800$). 86

A.18 Negative streamwise shear stress at $y = 2$, normalized with the uncontrolled field value $-\tau_{\mathrm{w0}}$ vs time normalized with the forcing period T. This figure shows its trend during time history for each couple of parameters (ζ,$T^+ = 10800$). 87

A.19 Turbulent kinetic energy per unit mass integrated over the wall-normal direction $K = \int_0^2 k \, \mathrm{d}y$, normalized with the uncontrolled field value K_0 vs time normalized with the forcing period T. This figure shows its trend during time history for each couple of parameters (ζ,$T^+ = 10800$). 88

A.20 Turbulent kinetic energy per unit mass integrated over the wall-normal direction $K = \int_0^2 k \, \mathrm{d}y$, normalized with the uncontrolled field value K_0 vs time normalized with the forcing period T. This figure shows its trend during time history for each couple of parameters (ζ,$T^+ = 10800$). 89

A.21 Flow rate normalized with the uncontrolled field value Q_0 vs time normalized with the forcing period T. This figure shows its trend during time history for each couple of parameters (ζ,$T^+ = 14400$). 90

A.22 Streamwise shear stress at $y = 0$, normalized with the uncontrolled field value $\tau_{\mathrm{w}0}$ vs time normalized with the forcing period T. This figure shows its trend during time history for each couple of parameters (ζ,$T^+ = 14400$). 91
A.23 Negative streamwise shear stress at $y = 2$, normalized with the uncontrolled field value $-\tau_{\mathrm{w}0}$ vs time normalized with the forcing period T. This figure shows its trend during time history for each couple of parameters (ζ,$T^+ = 14400$). 92
A.24 Turbulent kinetic energy per unit mass integrated over the wall-normal direction $K = \int_0^2 k \,\mathrm{d}y$, normalized with the uncontrolled field value K_0 vs time normalized with the forcing period T. This figure shows its trend during time history for each couple of parameters (ζ,$T^+ = 14400$). 93
A.25 Negative streamwise shear stress τ_{w} at $y = 2$, normalized with the uncontrolled field value $-\tau_{\mathrm{w}0}$ vs time normalized with the forcing period T. This figure shows a comparison (for one chosen cycle) of the effect of the duty-cycle ζ for each forcing period. Top: $T^+ = 3600$ during the V cycle. Middle: $T^+ = 10800$ during the X cycle. Bottom: $T^+ = 14400$ during the X cycle. 94
A.26 Turbulent kinetic energy per unit mass integrated over wall-normal direction $K = \int_0^2 k \,\mathrm{d}y$, normalized with the uncontrolled field value K_0 vs time normalized with the forcing period T. This figure shows a comparison (for one chosen cycle) of the effect of the duty-cycle ζ for each forcing period. Top: $T^+ = 3600$ during the V cycle. Middle: $T^+ = 10800$ during the X cycle. Bottom: $T^+ = 14400$ during the X cycle. 95

B.1 Target velocity profile U_γ normalized with U_b vs wall-normal coordinate. 98
B.2 The effect on the negative streamwise pressure gradient of the body force turning on. 100
B.3 The effect on the turbulent kinetic energy per unit mass, integrated over the wall-normal direction $K = \int_0^2 k \,\mathrm{d}y$, of the body force turning on. 100

List of Tables

3.1 Channel domain. 46
3.2 Parametric study. 47

4.1 R_D at $T^+ = 3600$. This table shows the value of drag reduction for each cycle, varying the duty-cycle. 50
4.2 R_D at $T^+ = 10800$. This table shows the value of drag reduction for each cycle, varying the duty-cycle. 51
4.3 R_D at $T^+ = 14400$. This table shows the value of drag reduction for each cycle, varying the duty-cycle. 51
4.4 R_P at $T^+ = 3600$. This table shows the value of power saving for each cycle, varying the duty-cycle. 56
4.5 R_P at $T^+ = 10800$. This table shows the value of power saving for each cycle, varying the duty-cycle. 57
4.6 R_P at $T^+ = 14400$. This table shows the value of power saving for each cycle, varying the duty-cycle. 57

A.1 Channel domain for studying resolution problem in y-direction. . 71

Contents

Introduction **23**

1 Flow control **27**
- 1.1 Flow control science 27
- 1.2 Flow control strategies 28
- 1.3 Some definitions 29
  - 1.3.1 Skin friction coefficient 29
  - 1.3.2 Drag reduction and power saving rates 30

2 Pulsating flows **35**
- 2.1 Previous studies 35
- 2.2 Regime classification 37
- 2.3 Accelerating/decelerating flows 39

3 DNS of a channel flow with pulsating forcing **41**
- 3.1 Channel flow: model problem 41
  - 3.1.1 Discretization 42
- 3.2 Pulsating forcing 44
- 3.3 Domain characterization 45
- 3.4 Parametric study 46
- 3.5 Some definitions 47
  - 3.5.1 Skin friction coefficient 47
  - 3.5.2 Drag reduction and power saving rates 47

4 Results **49**
- 4.1 Drag reduction 49
  - 4.1.1 The importance of knee in flow rate diagram for R_D 50
  - 4.1.2 The influence of forcing period 54
  - 4.1.3 The effect of duty-cycle 54
- 4.2 Power saving 56
- 4.3 Turbulence statistics 56
  - 4.3.1 Uncontrolled flow 56
  - 4.3.2 Controlled flow: mean velocity profile 59

4.3.3 Controlled flow: turbulent fluctuations 61
4.4 Streamwise shear stress 62

5 Conclusions and future work 69

A Other figures 71
A.1 DNS code validation 71
A.1.1 Resolution check 71
A.2 Parameters comparison 73

B Manipulation of the velocity profile 97
B.1 Model problem 97
B.2 Numerical method 98
B.3 Results 99

Bibliography 101

Introduction

Turbulence has a great importance in many physical processes involving fluids. The flow of a gas or liquid in a pipe, the flow around an aircraft, the mixing processes that take place in engines, the boundary layer and wake around bluff bodies, atmospheric phenomena and blood flow in human body are some examples of the great variety of everyday-life situations in which turbulent flows can be encountered. Else, the interest of researchers in fluid dynamics and turbulence can be easily understood.

The true understanding of turbulent flows is nowadays a great unsolved problem of classical physics. The difficulty to state a simple and unique definition of turbulence and of its features gives an idea of its complexity. It remains a critical branch of fluid dynamics, where a lot of research effort has to be done yet.

According to Pope [37], the state of art of turbulent flows study and research can be divided in the three main fronts:

- theoretical comprehension of properties and dynamics of turbulent flows, which allows further developments in turbulence modelling and prediction;
- experimental campaigns, both numerical and practical which allows the discovery of qualitative and quantitative data on several turbulent flows;
- flow control techniques, which allows the achievement of particular engineering goals through the change of particular flow characteristics.

Before introducing the main subject of this work, namely the turbulent channel flow subjected to a pulsating forcing, a survey about the third research branch, which studies the flow control, is needed.

Flow control technologies have the objective to manipulate the flow field to obtain specific behaviours. Nowadays is a highly multi-disciplinary research activity. Concerning the aerospace engineering field, four fundamental objectives are drag reduction, lift enhancement, mixing augmentation in engine, noise suppression. To reach them, many strategies have been developed during the last years. These can be divided into active or passive techniques, according to the requirement of external energy and control loop implication.

Among the goals just presented above, the drag reduction is the main objective in this work which is achieved through the use of pulsating turbulent flows. These are characterized by flow unsteadiness determined by a periodic time-varying forcing superposed onto a stationary component. Their relevance can be found in many engineering applications: examples concern biological flows, like pulmonary ventilation or blood flow in aortic and coronary arteries, and environmental flows like flow over the ocean bed or sediment transport in coastal water.

A novel approach presented here for a pulsating turbulent channel flow concerns the use of a particular type of forcing term, characterized by a strong flow acceleration, followed by an equally strong flow deceleration, with the constraint of imposing the same cycle-averaged acceleration of the respective uncontrolled flow. This is made in terms of time-dependent streamwise pressure gradient, which module is P_x, that is uniform in all spatial directions (the waveform of the forcing term varying time is given in figure 1). A parametric study, varying forcing period and duty-cycle, that is the percentage of one period in which a signal is active, has been conducted to verify how the drag reduction rate changes with them. The use of any external device permits to classify this control technique as a passive strategy. Nevertheless the net energy consumption for moving the pump has to be considered.

This study has been done by using the Direct Numerical Simulation (DNS) code developed by Professor Quadrio M. and Luchini P., implemented with the pulsating forcing just presented above.

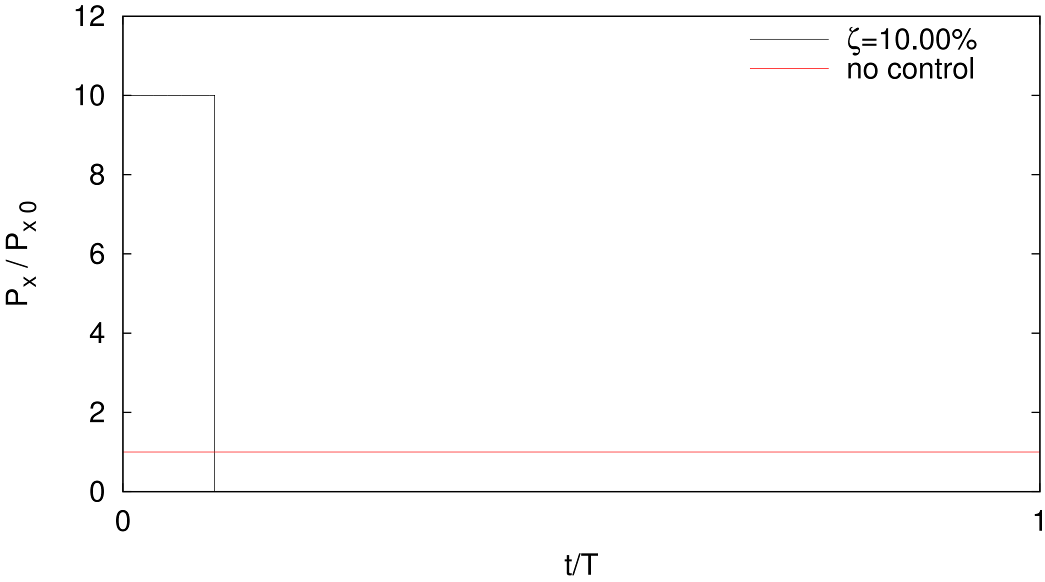

Figure 1: Imposed pressure gradient P_x, normalized with the uncontrolled field value P_{x0} vs time normalized with the forcing period T. Duty-cycle is imposed equal to $\zeta = 10.00\%$.

The work is structured as follows:

- INTRODUCTION.
- CHAPTER 1: FLOW CONTROL.

  Firstly a brief introduction on the flow control is presented. After that, some definitions, recalled many times in the work, are introduced.
- CHAPTER 2: PULSATING FLOWS.

  This chapter is focused on pulsating turbulence flows, since their centrality in this work. Successively, an introduction to accelerating and decelerating flows is reported because the forcing term implemented will be modelled through these ones.
- CHAPTER 3: DNS OF A CHANNEL FLOW WITH PULSATING FORCING.

  Chapter 3 describes the channel flow and the set of equations that governs it. After that, the pulsating forcing that moves the flow is presented with a brief discussion on what type of control strategy it implicates. Then it follows the description of the numerical domain implemented and the parametric campaign conducted in this work. Finally, the definitions given in Chapter 1 will be adjusted for the pulsating flows.
- CHAPTER 4: RESULTS.

  Here the discussion of the results obtained in terms of drag reduction and power saving is presented. Finally the turbulent statistics are discussed.
- CHAPTER 5: CONCLUSIONS AND FUTURE WORK.
- APPENDIX A: OTHER FIGURES.

  Here some figures concerning the pulsating channel flow just presented before have been added to deepen important aspects simply mentioned in Chapter 4.
- APPENDIX B: MANIPULATION OF THE VELOCITY PROFILE.

  In this appendix, an attempt to implement an active technique for a channel flow, that changes the morphology of the velocity profile through the introduction of a body force, has been done. It has drag reduction as goal.

Chapter 1

Flow control

Flow control is a branch of fluid dynamics that concerns the possibility to change the characteristics of a turbulent flow to obtain from it advantages from engineering view-point. In this chapter, a survey about flow control inspired by Gad-el-Hak's book [11] is presented.

1.1 Flow control science

The science of flow control arose with Prandtl in 1904, who introduced the boundary-layer theory, explained the physics of the separation phenomena, and described several experiments in which a boundary layer was controlled.

In the last years, flow control has become a highly multi-disciplinary research activity encompassing theoretical, computational and experimental fluid dynamics, acoustics, control theory, physics, chemistry, biology and mathematics.

In the field of aerospace engineering, several goals has to be considered in flow control:

- drag reduction,
- lift enhancement,
- mixing augmentation in engines,
- noise suppression.

Each goal may be achieved through delay or advancement of transition from laminar to turbulent flow, prevention or provocation of flow separation, suppression or enhancement of turbulence levels. But it has to be done by using a simple device that is inexpensive to build as well as to operate, so that the expense for flow manipulation would result in a significant net positive power saving. Unfortunately, it is very difficult to reach all these goals together, rather it is easier that one badly influences the others. Thus, an engineer has to get off at a compromise.

1.2 Flow control strategies

In order to give an exhaustive view on flow control methods, we have to remark that flow control techniques are usually divided into categories. These are dictated by some considerations, one of which considers energy expenditure and control loop involved, as shown in figure 1.1.

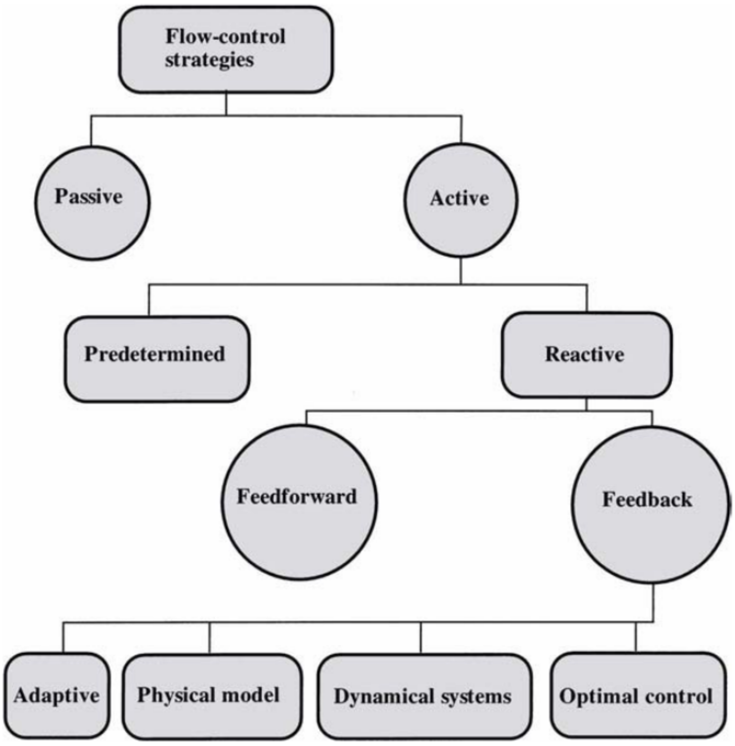
Flow-control strategies
Passive
Active
Predetermined
Reactive
Feedforward
Feedback
Adaptive
Physical model
Dynamical systems
Optimal control

Figure 1.1: Classification scheme of flow control methods. Figure taken from [11].

A control device can be passive, thus requiring no auxiliary energy and no control loop, the net energy saving being equal to energy saved, or active, hence requiring some energy expenditure, thus the net energy saving being equal to the energy saved minus the energy spent to apply the control. Moreover, active control requires a control loop and is further divided into predetermined or reactive. Predetermined control is an open-loop control that doesn't require any measure of the flow state, being independent from it (figure 1.2a). Instead, reactive control depends on flow state and the control action is continuously adjusted based on measurements of some kind. Reactive control can be feedforward (figure 1.2b) or feedback (figure 1.2c). In the former case, measured and controlled variables differ among them, whereas feedback control necessitates the controlled variable be measured, fed back and compared with a target input.

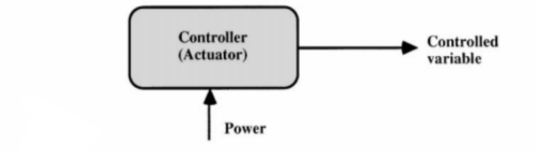
Controller
(Actuator)
Controlled variable
Power

(a) *Predetermined*

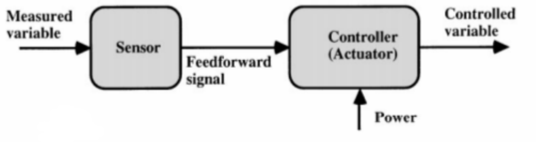
Measured variable
Sensor
Feedforward signal
Controller
(Actuator)
Controlled variable
Power

(b) *Reactive: feedforward loop*

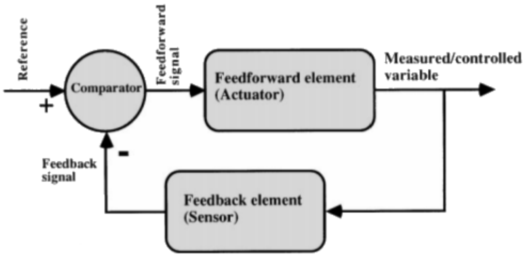
Reference
+
Comparator
Feedforward signal
Feedforward element
(Actuator)
Measured/controlled variable
-
Feedback signal
Feedback element
(Sensor)

(c) *Reactive: feedback loop*

Figure 1.2: Control loops for active flow control. Figure taken from [11].

1.3 Some definitions

To understand the effect of a control strategy, some fundamental parameters have to be introduced. In this section some definitions concerning drag reduction goal will be provided. Moreover, these will be referred to a channel flow because is the geometry used in this work.

1.3.1 Skin friction coefficient

The streamwise shear stress for a channel flow is defined as

$$\tau = \rho\nu \frac{\partial\langle u\rangle}{\partial y} - \rho\langle u'v'\rangle, \tag{1.1}$$

where, ν is the kinematic viscosity and ρ is the fluid density, whereas, hereinafter, the superscript $'$ indicates the fluctuations of velocity and $\langle\quad\rangle$ the time and spatial (over the streamwise x and spanwise z direction) averaged operator, defined as

$$\langle\quad\rangle = \frac{1}{(t_2 - t_1)} \frac{1}{L_z L_x} \int_{t_1}^{t_2} \int_{L_z} \int_{L_x} \quad \mathrm{d}x\,\mathrm{d}z\,\mathrm{d}t. \tag{1.2}$$

Here L_x and L_z are the streamwise and spanwise length respectively and $t_2 > t_1$ are two time instants.

At wall, due to no-slip condition, the Eq. (1.1) reduces to the following expression

$$\tau_{\mathrm{w}} = \rho\nu \frac{\partial\langle u\rangle}{\partial y}\bigg|_{\mathrm{w}}. \tag{1.3}$$

Since top and bottom wall are present, we have two wall shear stresses, $\tau_{\mathrm{w},t}$ and $\tau_{\mathrm{w},b}$, respectively. So their averaged value is the significant quantity

$$\widetilde{\tau}_{\mathrm{w}} = \frac{\tau_{\mathrm{w},t} + \tau_{\mathrm{w},b}}{2}. \tag{1.4}$$

Hereinafter we refer with τ_{w} to $\widetilde{\tau}_{\mathrm{w}}$ for lightening the notation. Equally, the skin friction coefficient based on bulk velocity can be written as

$$C_f = \frac{2\tau_{\mathrm{w}}}{\rho U_b^2} = \frac{C_{f,t} + C_{f,b}}{2}, \tag{1.5}$$

where $C_{f,t}$ and $C_{f,b}$ are the skin friction coefficient at top and bottom wall respectively and U_b is the bulk velocity, defined as

$$U_b = \frac{1}{L_y}\int_{L_y} \langle u\rangle \, \mathrm{d}y, \tag{1.6}$$

where L_y is the wall-normal length.

1.3.2 Drag reduction and power saving rates

The drag reduction rate R_D has to be evaluated as

$$R_D = \frac{C_{f,0} - C_f}{C_{f,0}} \times 100, \tag{1.7}$$

that is the relative change in skin friction coefficient, between uncontrolled ($C_{f,0}$) and controlled (C_f) case in percentage value. R_D has to be a positive value in order that the control strategy brings advantages.

In order to give a clear-cut definition of power saving rate, we define the power input that is necessary to drive the flow as

$$P = Q\left\langle \frac{\partial p}{\partial x} \right\rangle_V, \tag{1.8}$$

where Q is the volume flow rate per unit length, defined as $Q = \int_{L_y} \langle u\rangle \, \mathrm{d}y = L_y U_b$, $\partial p/\partial x$ is the streamwise component of pressure gradient and, hereinafter, $\langle \quad \rangle_V$ is the volume averaged value defined as

$$\langle \quad \rangle_V = \frac{1}{L_y}\int_{L_y} \langle \quad \rangle \, \mathrm{d}y. \tag{1.9}$$

As for skin friction coefficient, a power coefficient based on bulk velocity can be defined as

$$C_P = \frac{2P}{\rho U_b^3}. \tag{1.10}$$

It is now possible to define the power saving rate R_P as

$$R_P = \frac{C_{P,0} - C_P}{C_{P,0}} \times 100, \tag{1.11}$$

that is the relative change in power coefficient between uncontrolled ($C_{P,0}$) and controlled (C_P) case in percentage value. As for R_D, a positive value of R_P means that the control strategy brings advantages.

In DNS, the control performance can be evaluated while keeping constant in time either the pressure gradient (CPG) or the flow rate (CFR) (constant power input CPI, described by Hasegawa *et al.* in [15], is contemplated too). In the former case, to obtain a drag reduction and a net savings, the flow rate has to increase, as evident from Eqs. (1.5), (1.7) and from the definition of flow rate Q. In the latter case, instead, the mean pressure gradient has to decrease. In this regard, Frohnapfel *et al.* in [8] have shown the previous reasoning in terms of pumping energy and convenience (figure 1.3). This will be briefly reported below.

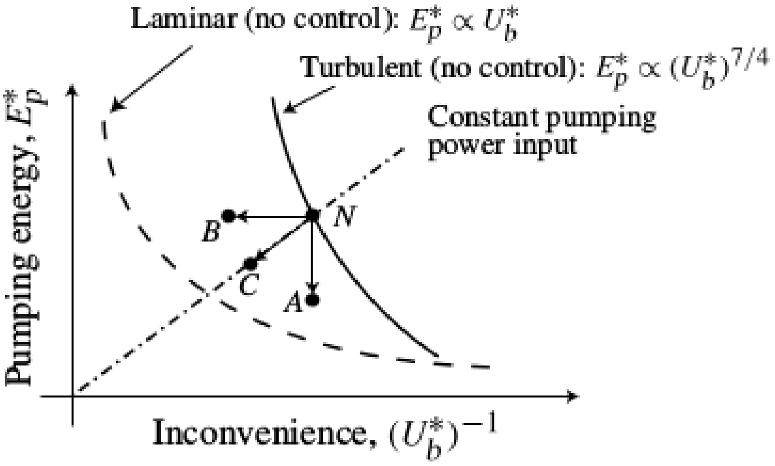
Laminar (no control): $E_p^* \propto U_b^*$
Turbulent (no control): $E_p^* \propto (U_b^*)^{7/4}$
Constant pumping power input
Pumping energy, E_p^*
Inconvenience, $(U_b^*)^{-1}$
N
B
C
A

Figure 1.3: Pumping energy vs inconvenience (operational time) for different input conditions. Here $()^*$ indicates dimensional quantities. Figure taken from [8].

Suppose control is applied to the non-controlled flow state, labelled as N in figure 1.3. When the bulk mean velocity is kept constant (CFR condition), the control shifts N along the vertical arrow to A. The percentage reduction of the pumping energy, visualized by the distance $|NA|$ between points N and A, is equivalent to drag reduction rate. On the other hand, under the CPG condition, successful control shifts N along the horizontal arrow to B, as discussed before. The dash-dotted line connecting the origin and flow state N represents the locus of points where the pumping power, i.e. the pumping energy divided by the operating time, remains constant. A shift to point C along the arrow therefore corresponds to a controlled state that requires the same power input as the non-controlled state (constant power input, CPI), while providing at the same time larger flow rate and smaller pumping energy.

A problem arises when an active control strategy is used. In fact the previous considerations don't include the energetic cost of control. In [8] an effective wall friction τ_{w}^e based on the total power consumption is introduced

$$\tau_{\mathrm{w}}^e = \tau_{\mathrm{w}} + \frac{P_c}{U_b}, \tag{1.12}$$

so that a new bulk skin friction coefficient can be defined as

$$C_f^e = \frac{2\tau_{\mathrm{w}}^e}{\rho U_b^2}. \tag{1.13}$$

Moreover in order to account for the energetic cost of control E_c, figure 1.3 with just pumping energy E_p is replaced by figure 1.4, where the total energy $E_t = E_p + E_c$ is used on the vertical axis.

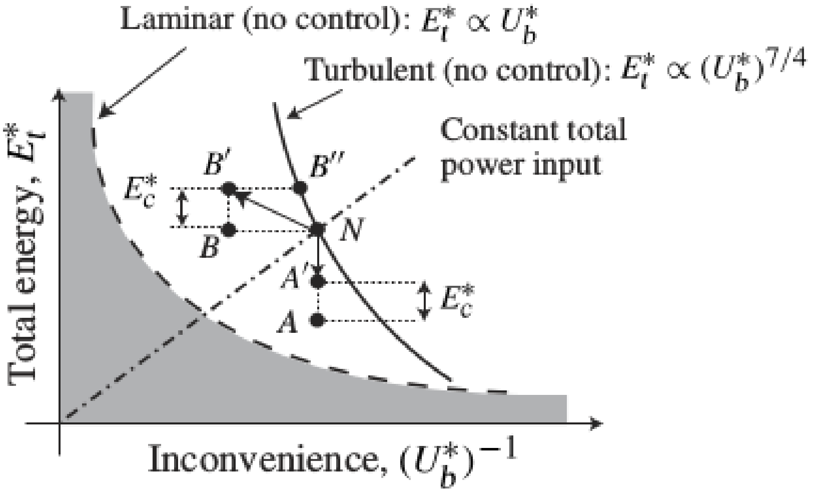
Laminar (no control): $E_t^* \propto U_b^*$
Turbulent (no control): $E_t^* \propto (U_b^*)^{7/4}$
Constant total power input
Total energy, E_t^*
Inconvenience, $(U_b^*)^{-1}$
B'
B''
E_c^*
B
N
A'
A
E_c^*

Figure 1.4: Total energy vs inconvenience (operational time) for different input conditions. Here $()^*$ indicates dimensional quantities. Figure taken from [8].

The additional control energy input E_c is reflected in figure 1.3 by the shift of points A and B in the vertical direction to A' and B', respectively. In this plot the distance $|NA|$, corresponds to the conventional drag reduction rate R_D

under CFR, while $|NA'|$ reflects the net energy savings. In a similar manner, $|NB|$ explains the decrease in C_f achieved under CPG owing to the increase in flow rate, whereas $|B'B''|$ quantifies the portion of that increase that is due to successful flow control and $|NB| - |B'B''|$ is the remaining portion due to the increase in pumping energy.

In figure 1.4 is also shown the limit for drag reduction, depicted by the grey region. In fact, according to Bewley [3] and Fukagata *et al.* [10], the total energy consumption at a given flow rate is minimized when the flow becomes laminar, so no flow state can be collocated below the laminar curve. This result is known as a fundamental performance limitation.

Chapter 2

Pulsating flows

In this chapter will be presented the flow type studied in this thesis: the *pulsating* flows. These result from the superposition of an unsteady pulsation (actually one or more) on a steady shear flow. Examples of relevant applications concern biological flows like pulmonary ventilation or blood flow in aortic and coronary arteries and environmental flows like flow over the ocean bed or sediment transport in coastal water. The oscillatory component of motion may be generated artificially by a rotating or poppet valve, like those present in variable-displacement pumps, or it may be result from an interaction problem. The steady flow is usually associated with a stationary pressure forcing.

The oscillatory component of motion notably increases the complexity of this kind of flows. For this reason, despite their great relevance, little is known about the physics of pulsating turbulent flows, even in simple geometries.

In the following section, the state of art concerning the pulsating flows is presented, taking the cue from the work of Manna *et al.* [32].

2.1 Previous studies

Many analytical, numerical and experimental studies have had as main topic the pulsating flows. Analytical solutions to pulsed laminar flows in pipes and channels has been determined by Uchida in [60] and Telionis in [56], respectively. Several theoretical studies on plane Poiseuille flow have shown that a periodic flow modulation may stabilize the mean flow: it depends on amplitude and frequency of modulation itself. For example, Hall and von Kerczek in [14] and [61] respectively have shown that very high frequencies have a destabilizing effect on the plane Poiseuille flow whereas a stabilizing effect of sinusoidal pulsations at very low frequencies was described by Singer *et al.* in [50]. With regard to the stability of pulsating pipe flows, the available literature is more limited. In [57] Tozzi and von Kerczek have shown that low-frequency oscillatory Hagen-Poiseuille flow is slightly more stable to axisymmetric disturbances than the steady flow.

From experimental standpoint instead, the pulsating pipe flows have been subjected to many studies. Gilbrech and Coombs in [12] and Sarpkaja in [43] indicate that both amplitude and frequency of the pulsation increase the critical Reynolds number as long as local flow reversal does not occur. Laminar to turbulent transition studies on pulsatile pipe flows were firstly experimentally carried out by Yellin in [63]. He demonstrated that neither the mean nor the instantaneous Reynolds number provided a sufficient criterion for determining the laminar to turbulent transition boundary. Moreover, he introduced the concept of *relaxation time* to interpret the effect of a periodic component superposed onto the mean flow and, through this concept, showed that slowly oscillating flows of large amplitude tend to suppress or destroy the turbulence downstream of the disturbance source. Other important contributions come from the studies of Ramaprian and Tu in [41], Shemer and Kit in [49], Shemer in [48] and Stettler and Hussain in [53]. Ramaprian and Tu [41], dealing with transitional pipe flows at low Reynolds numbers, indicated that flow pulsations increase the critical Reynolds number. The occurrence and extent of laminarization was, however, found to depend on factors such as the intermittency of turbulent puffs in the mean quasi-steady flow and the frequency of oscillation. Shemer [48] concluded that the transition phenomenon is primarily governed by the instantaneous Reynolds number. Stettler and Hussain [53] performed an intensive experimental study and provided a three-dimensional map of stability–transition regimes, suggesting that transition in pipes is mainly associated with plugs of turbulence that can grow or shrink in size. The measurements of Lodahl *et al.* in [27] showed that the laminar to turbulent transition boundary is influenced by large values of the oscillating amplitude and frequency. The results of the DNS of Tuzi and Blondeaux shown in [59], obtained in a pipe characterized by small superficial wall imperfections, are in qualitative agreement with those of Lodahl *et al.* [27]. Discrepancies were attributed to the different level of flow perturbations present in the experimental apparatus with respect to those introduced in the numerical simulation by the wall imperfections.

Few studies have been carried out on these flows with drag reduction and his mechanism as goals. The first probably was conducted by Mao and Hanratty [33] in 1986, in which they investigated the interaction between the imposed flow oscillation and the turbulence fluctuations. Other studies have been carried out by Lodahl *et al.* [27], Manna and Vacca [31], Iwamoto *et al.* [19], [20] and Souma *et al.* [52]. Only Iwamoto *et al.* in [19] and [20] and Souma *et al.* in [52] have studied the effects on power saving rate too.

It would be interesting to study more in depth this part of the pulsating flows literature. For this reason, the present work has the goal to research a possible effect of this kind of flows on drag reduction and power saving.

2.2 Regime classification

The oscillatory component of motion increases the relevant similarity parameters from one, in case of the steady flow, to three. In [32], Manna *et al.* proposed several kinds of regimes based on different choices of the three dimensionless parameters.

They consider the incompressible pulsating flow through a circular pipe with diameter $D = 2R$ and axial length L_z driven by a time-varying harmonic body force of prescribed mean, amplitude and frequency. The resulting flow is characterized by a volume-averaged velocity consisting of a steady component U_b and a harmonically time-varying one, with amplitude U_0 and pulsation $\omega = 2\pi/T$, T being the oscillation period. Then they reported many different choices of parameters: for example, firstly they proposed the choice due to Yellin in [63]

$$Re_b = \frac{U_b D}{\nu}, \quad \Omega = \frac{R}{\delta}, \quad \beta = \frac{U_0}{U_b}, \tag{2.1}$$

where $\delta = \sqrt{2\nu/\omega}$ is the Stokes layer thickness, with ν the kinematic viscosity, and Ω the Stokes number. Using this choice, they define two different regimes:

- *current-dominated* regime, $\beta < 1$,
- *wave-dominated* regime, $\beta > 1$.

Other triplets proposed are:

$$Re_b = \frac{U_b D}{\nu}, \quad \Omega_t = \frac{\omega D}{u_\tau}, \quad U_m/U_b, \quad \text{Ramaprian and Tu [42]}, \tag{2.2}$$

$$Re_c = \frac{U_c D}{\nu}, \quad \omega^+ = \frac{2}{\delta^{+2}}, \quad U_m/U_c, \quad \text{Tardu and Binder [54]}, \tag{2.3}$$

$$Re_b = \frac{U_b D}{\nu}, \quad Re_\omega = \frac{U_m^2}{\omega\nu}, \quad U_m/U_b, \quad \text{Lodahl \textit{et al.} [27]}, \tag{2.4}$$

with U_c the mean centreline velocity and U_m the maximum value of the oscillatory flow at the centre of the pipe, u_τ is the friction velocity, defined as $u_\tau = \sqrt{\tau_{\mathrm{W}}/\rho}$, and the superscript + indicates the inner variables scaling, based on friction velocity and kinematic viscosity.

Nearly the entire literature has dealt with pulsating pipe or channel flows with β values less than one (current-dominated regime) (Ramaprian and Tu [41], [42]; Tu and Ramaprian [58]; Shemer and Kit [49]; Shemer [48]; Mao and Hanratty [33], [34]; Stettler and Hussain [53]; Tardu and Binder [54]; Tardu *et al.* [55]; Scotti and Piomelli [45]; Bhaganagar [4]; He and Jackson [16]).

In [42], Ramaprian and Tu proposed several regimes (diffently from Yellin) based on the value of Ω_t:

- *type I* or quasi-steady regime ($\Omega_t \leq 10^{-1}$). The flow behaves as a steady flow and there will be neither velocity overshoot nor phase lag of the ensemble-averaged quantities compared to the steady values obtained with a corresponding time constant pressure gradient. The turbulent structure changes within the oscillating period, but it can be described as a sequence of steady states, since at all times turbulence can relax to the local (in time) equilibrium;

- *type II* or low-frequency regime ($10^{-1} \leq \Omega_t \leq 1$). This regime exhibits appreciable differences from the quasi-steady behaviour all across the pipe diameter, although the time mean flow will not be significantly different from that obtained with a quasi-steady analysis. The turbulence structure is not modified by the flow unsteadiness and it remains quasi-steady since the oscillation frequency f does not interact with the characteristic turbulent bursting frequency f_{burst}. This issue has been investigated in [35] by Mizuchina *et al.*, who provided for the lower, mean and upper values of the bursting frequency approximate power-law correlations, in a moderate Reynolds number range;

- *type III* or intermediate-frequency regime ($1 \leq \Omega_t \leq 10$). This regime is characterized by some interaction between the imposed unsteadiness and the turbulent structure. The latter will be affected, the changes being more pronounced as the oscillation frequency is increased. Also the turbulent equilibrium conditions will break down during part of the cycle and, as for the previous two regimes, the time mean flow does not significantly differ from the quasi-steady one, especially at the low end of the frequencies;

- *type IV* or high-frequency regime ($\Omega_t \sim O(10)$ or higher). Here the imposed oscillation strongly interacts with the turbulent bursting process at the wall, and the turbulent structure is substantially altered. The time mean radial distribution of all quantities will differ from the corresponding quasi-steady one, sometimes through the appearance of inflection points in the near-wall region. Time-varying flow quantities will undergo significant changes in a near-wall thin layer while a solid-body-like oscillation condition will occur elsewhere. The turbulent structure will exhibit a remarkable departure from the equilibrium conditions in a small fraction of the pipe radius close to the wall, while it remains practically frozen in the outer part of the shear layer, where it shows an essentially flat streamwise velocity profile.

- *type V* or rapid oscillation ($\Omega_t \sim 10^2$). The interaction between the imposed oscillation and the turbulent structure will be very strong, although confined to a very thin near-wall layer. Very little information is available in this regime.

For a more thorough discussion about other subdivision of flow regimes in pulsating condition, the interest reader is referred to [32]. These subdivisions are considered for pulsating flows that have *only one pulsation* in the oscillating term. In this work instead the forcing term contains many frequencies, so it is not possible to collocate the resulting flow into the regimes presented.

Similar flows to which described in this work have been studied by Seddighi *et al.* in [47] and [46], He *et al.* in [18] and [17], Ariyaratne *et al.* in [1] and Chung in [6]. In fact they described an unsteady (not periodic) turbulent channel/pipe flow subjected to acceleration or deceleration. A more detailed description follows in the next section.

2.3 Accelerating/decelerating flows

Unsteady turbulent flows in pipes and channels include periodic and non-periodic flows. Both cases have been studied experimentally as well as theoretically, but greater attention has been focused on periodic flows, as also shown in the previous section. This is justified by many practical applications involving pulsations. However, non-periodic flows with uniform acceleration/deceleration have advantages for unravelling the non-equilibrium behaviour of turbulence dynamics in unsteady flows. Seddighi *et al.* in [47] performed a DNS of a linearly accelerating channel flow starting from an initially statistically steady turbulent flow. They show that response of the accelerating flow is fundamentally the same of step-change transient flow described by He and Seddighi [17]. They explained how the flow structure behaves like a boundary layer bypass transition, undergoing three distinct phases, namely:

- *pre-transition.* The flow is laminar-like and the pre-existing turbulent structures are modulated resulting in elongated streaks leading to a strong and continuous increase in the streamwise fluctuating velocity, but to a little change in the other two components;
- *transition.* The flow undergoes transition when isolated turbulent spots are generated which spread and merge with each other;
- *fully turbulent.* These turbulent spots cover the entire surface of the wall when the flow is fully turbulent.

Ariyaratne *et al.* in [1] studied the response of the wall shear stress to a deceleration. They show that this exhibits some features in common with responses in accelerating flows, but also strong differences. Turbulence delays are shown to be important, causing, in effect, a frozen-turbulence response at early times. At larger times, instead, flow reversal and increasing turbulence time-scales prevent the development of asymptotic conditions. In [46] Seddighi *et al.* have performed a DNS of a turbulent channel flow subjected to a step change in pressure gradient to facilitate a direct comparison between ramp-up and ramp-down flows. Strong differences are found between behaviours of turbulence in the two flows. The wall shear stress in the ramp-up flow first overshoots, and then strongly undershoots the quasi-steady value in the initial stage of the excursion, before approaching the quasi-steady value. In a strongly decelerating flow, the wall shear stress tends to first undershoot but then overshoot the quasi-steady value. They imputed these behaviours to the slow response of turbulence as well as flow inertia. The three phase described before for the uniformly accelerating flows have been again observed in the ramp-up flow, but the transition between the various stages is more gradual. In a strongly decelerating flow, instead, they found that response of turbulence exhibits a two-stage development.

Finally, Chung in his work [6] has investigated a turbulent flow subjected to a sudden change in pressure gradient. He found that there are two different relaxations: a fast relaxation at the early stage and a slow one at the later stage.

Basing on these studies about the unsteady flows in general, in this thesis a DNS of a pulsating (periodic) flow with a sudden strong acceleration followed by a strong deceleration, due to the forcing shut down, will be performed.

Chapter 3

DNS of a channel flow with pulsating forcing

In this chapter we describe the flow control strategy conceived in this thesis. First of all an introduction of channel flow and a brief description of the numerical method designed for the DNS code (see also [38]), is needed. After that, chapter is oriented to the description of the forcing term acting on channel flow (with a brief discussion about which type of control strategy implicates) and its implementation inside the DNS code. In addition, it follows the characterization of channel box and initial flow field. The last part, finally, relates the presentation of the parametric study and an adaptation to pulsating flows of quantities described in section 1.3.

3.1 Channel flow: model problem

The channel flow is a flow between two parallel, infinite plates placed at distance $L_y = 2\delta$. As outlined in figure 3.1, a Cartesian coordinate system is introduced, where x, y and z denote the streamwise, wall-normal and spanwise directions, respectively. The velocity field is composed by the streamwise, wall-normal and spanwise components u, v and w. The pressure field is denoted by p. Due to the infinite extent of walls, two statistically homogeneous direction can be identified, namely x and z, so that the mean streamwise velocity $\langle u \rangle$ depends only on the wall-normal coordinate y. Thus the flow is assumed to be periodic for computation in streamwise and spanwise directions, with periodic boundary conditions on the unbounded portion of the domain.

The non-dimensional equations that govern the flow are the incompressible Navier-Stokes equations (iNSEs) in cartesian coordinates

$$\begin{cases} \dfrac{\partial \mathbf{u}}{\partial t} + (\mathbf{u} \cdot \boldsymbol{\nabla})\mathbf{u} = -\boldsymbol{\nabla} p + \dfrac{1}{Re}\Delta \mathbf{u}, \\ \boldsymbol{\nabla} \cdot \mathbf{u} = 0. \end{cases} \tag{3.1}$$

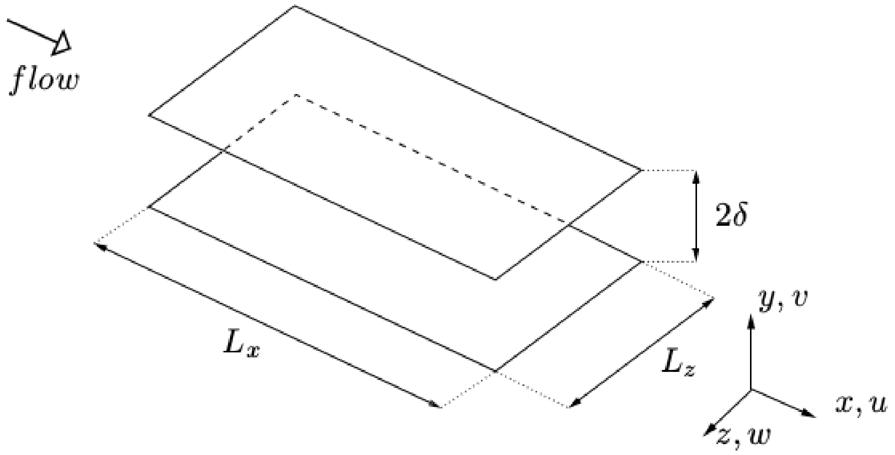

Figure 3.1: Channel flow. Figure taken from [38].

The equations are normalized with a reference velocity U, a reference length l and a reference kinematic viscosity ν, so that the Reynolds number can be defined as

$$Re = \frac{Ul}{\nu}. \tag{3.2}$$

The differential problem is closed when an initial condition for all the fluid variables is specified.

Most of the problems connected to the solution of iNSEs relate the imposition of continuity equation and the determination of correct boundary and compatibility conditions. Luckily, for a channel flow, the four original scalar equations of the set (3.1) can be reduced to two scalar equations (v-η formulation) for wall-normal velocity v and wall-normal vorticity η, defined as

$$\eta = \frac{\partial u}{\partial z} - \frac{\partial w}{\partial x}. \tag{3.3}$$

3.1.1 Discretization

The existence of two statistically homogeneous directions and the consequent imposition of cyclic boundary condition at the sides of the domain, suggests the possibility to represent the solution $v(x, y, z, t)$ and $\eta(x, y, z, t)$ in terms of a complete expansion that automatically respects such boundary condition. The natural choice is the truncated Fourier series expansion in the two homogeneous directions x and z, leading to the following expressions for v and η

$$v(x,y,z,t) = \sum_{h=-N_x/2}^{N_x/2} \sum_{l=-N_z/2}^{N_z/2} \widehat{v}_{l,h}(y,t) e^{\iota \alpha t} e^{\iota \beta t}, \tag{3.4}$$

$$\eta(x,y,z,t) = \sum_{h=-N_x/2}^{N_x/2} \sum_{l=-N_z/2}^{N_z/2} \widehat{\eta}_{l,h}(y,t) e^{\iota \alpha t} e^{\iota \beta t}, \tag{3.5}$$

where N_x and N_z are the higher wavenumbers at which the discrete Fourier transform has been truncated (before the de-aliasing process for the numerical evaluation of the non linear terms), while $\alpha = 2\pi h/L_x = h\alpha_0$ and $\beta = 2\pi l/L_z = l\beta_0$ represent respectively the streamwise and spanwise wavenumbers. Here, α_0 and β_0 are the fundamental wavenumbers, while h and l are integers that spans the Fourier space for the two directions, defined in terms of streamwise and spanwise lengths $L_x = 2\pi/\alpha_0$ and $L_z = 2\pi/\beta_0$, of computational domain. So the equations for v-η can be expressed in terms of Fourier modes $\widehat{v}_{h,l}$ and $\widehat{\eta}_{h,l}$.

In present code, the mesh in non-homogeneous direction y has been generated with the stretching function

$$y = \frac{\tanh a\overline{y}}{a}, \tag{3.6}$$

where a is an adjustable parameter, used to modify the mesh deformation, and $\overline{y}$ is a mesh grid with constant spacing coming from lower to upper wall. To evaluate the spatial derivatives in y-direction, a finite difference compact scheme has been used.

Time integration of these equations has been approached via a partially-implicit method, paying attentions to memory requirements (by exploiting the finite-difference discretization of wall-normal direction). This is made through a higher-accuracy Runge-Kutta scheme for explicit parts of the equations (the non linear terms), and through an implicit second-order Crank-Nicholson scheme. The latter has been chosen for the viscous part, the most stability-limiting part of the equations, relieving the stability requirement on the time-step size Δt. The program can work with both fixed and variable time step Δt. The condition used for the estimation of a proper Δt is a standard condition on CFL number.

The procedure to solve these discrete equations is made by two steps. The first one, consists in the assembling routine of the RHSs corresponding to the explicitly integrated parts. The second step involves, for each pair (α,β), the solution of a set of two ODEs, derived from the implicit formulation of viscous terms. This second step proceeds per wall-normal lines, since the simultaneous knowledge of the RHS in all y positions is required. The approach outlined grants excellent parallelization performances, in that a compact difference discretization in wall-normal direction allows to distribute the variables in wall-parallel slices and perform direct and inverse FFTs locally at each machines.

3.2 Pulsating forcing

The forcing term that moves the flow is imposed in terms of streamwise pressure gradient. So, channel flow in DNS is driven by CPG condition, that refers to a mean streamwise pressure gradient, uniform in all spatial directions, constant in time

$$\boldsymbol{\nabla} p = P_x \hat{\mathbf{x}} + \boldsymbol{\nabla} p', \tag{3.7}$$

where $\hat{\mathbf{x}}$ is the versor in streamwise direction, P_x refers to mean pressure gradient module and is a constant value, and superscript $'$ indicates the fluctuation component.

In this work, the steady condition has been replaced by an unsteady periodic forcing. The resulting pulsating channel flow will be moved by an initial strong acceleration, followed by an equal strong deceleration caused by the turning off of the pump (from physical standpoint). In DNS code, this translates into a piecewise in time CPG condition, acting on channel flow with a forcing period T.

A mathematical representation is given

$$P_x = \begin{cases} A & 0 \leq t < \zeta T \\ 0 & \zeta T \leq t < T, \end{cases} \tag{3.8}$$

where $A < 0$ is the amplitude of streamwise pressure gradient imposed and ζ is the duty-cycle, or the percentage of the time period in which a signal is active. The value of A is computed from the constraint that the cycle-averaged acceleration imposed to the flow is the same of the uncontrolled case (see the example in figure 3.2).

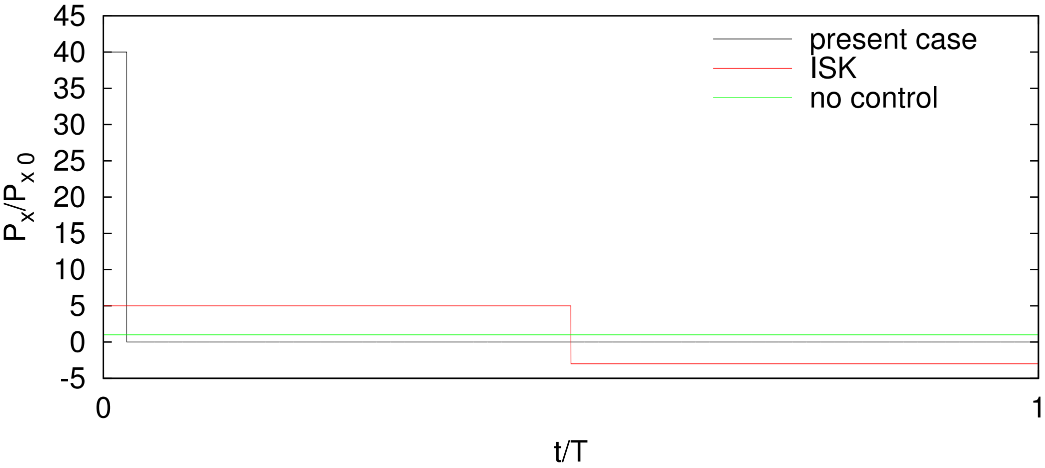

Figure 3.2: Negative pressure gradient normalized with the uncontrolled field value vs time normalized with the forcing period T. For the present case, duty-cycle ζ is equal to 2.50%. The red curve represents the forcing term of Iwamoto *et al.* [19], whereas the green curve represents the uncontrolled flow.

Iwamoto *et al.* in their work [19] studied a similar problem but with different forcing term. In fact they have imposed duty-cycle equal to 50%, the forcing resulting in a square-wave superposed onto the stationary component (see figure 3.2). They conducted a parametric study varying the forcing period T and the deceleration pressure gradient α_d to achieve an optimum value for drag reduction. The acceleration pressure gradient α_a is imposed with the law $\alpha_a = 2 - \alpha_d$, for respecting the same constraint on the cycle-averaged flow acceleration just described above. This operating principle would request an energy recovery system to achieve the maximum energy saving.

In this thesis, the choice of the waveform of the forcing term is due to ease of a possible application. In fact, addition of any new facilities beyond the pump is not requested.

Passive or active control?

As shown in Chapter 1, a control technique could be active or passive, depending on energy expenditure and control loop involved.

Defining the kind of this control strategy could be complex since it exhibits some aspects of both cases. For instance it may be regarded as an active strategy because, imposing the same cycle-averaged forcing of the uncontrolled case, the pump requires more or less power for moving the flow. Conversely, it could be considered as a passive technique because it doesn't require any external device that imposes an additional control energy to the flow. Therefore, we consider the present control strategy as passive.

However the energy cost will be taken into account in this work evaluating the power saving rate R_P.

3.3 Domain characterization

Different Reynolds numbers can be defined for a channel flow. One is based on the channel half-height δ and the reference bulk velocity U_b as

$$Re_b = \frac{U_b \delta}{\nu}. \tag{3.9}$$

Moreover, a Reynolds number can be defined, based on the channel half-width and the centreline velocity $U_c = \langle u \rangle \big|_{y=\delta}$, obtaining:

$$Re_c = \frac{U_c \delta}{\nu}. \tag{3.10}$$

In the laminar case the relation $U_c = 3/2 U_b$ holds. Choosing the skin friction velocity u_τ, defined in Chapter 2, as reference velocity leads to the definition of another Reynolds number

$$Re_\tau = \frac{u_\tau \delta}{\nu}. \tag{3.11}$$

The flow is driven by a constant piece-wise in time streamwise pressure gradient, as discussed in the previous section. Hence, Reynolds number Re_τ based on u_τ becomes the natural choice. In fact, if pressure gradient is fixed, then streamwise shear stress is fixed and hence u_τ is fixed too.

The initial field is a fully turbulent channel flow at $Re_{\tau 0} = 180$ (where the subscript 0 refers to the uncontrolled field), that corresponds to $Re_{b0} = 2800$. Simulations have been run with same Reynolds number of initial field. Iwamoto *et al.* in [19] have setted the uncontrolled field at $Re_{\tau 0} = 110$.

Unless otherwise indicated, the quantities reported hereinafter are scaled by δ, $u_{\tau 0}$ and ρ.

The computational domain chosen in present work, whose schematic is presented in figure 3.1, has a streamwise length of $L_x = 4\pi$ and a spanwise width of $L_z = 2\pi$. The domain has been discretized with a Fourier expansion of 192×160 modes for streamwise and spanwise directions, and 100 points in wall-normal direction. The parameter of the stretching function a is setted equal to 1.6.

An overview of these choices is given in table 3.1.

Quantity	Value
L_x	4π
L_y	2
L_z	2π
N_x	192
N_y	100
N_z	160
a	1.6

Table 3.1: Channel domain.

3.4 Parametric study

The performed parametric study has taken as parameters forcing period T^+ (where superscript + refers to normalization with $u_{\tau 0}$ and ν unless otherwise indicated) and duty cycle ζ. The values of these two parameters are shown in table 3.2. The choices have been done keeping as guidelines Iwamoto *et al.*' work [19] and Launder's work [24], in which they show, respectively, the importance of a long forcing period and of a severe acceleration for *relaminarization*.

Periodic flow condition suggests to limit the simulations at the end-time of a cycle. Only ten cycles have been considered because these simulations are very demanding in terms of computational resources. The total integration time varies from one simulation to another: this is related to the variable Δt that follows from the imposed constraint that the maximum value of the CFL number is unit.

ζ		T^+	
	3600	10800	14400
10.00%	✓	✓	
5.00%	✓	✓	✓
3.75%		✓	
2.50%	✓	✓	✓
1.25%	✓	✓	
0.50%	✓	✓	

Table 3.2: Parametric study.

Each simulation has been run in parallel mode (see [29] for detailed description of parallel strategy) on the dedicated parallel computing system at the Università di Salerno.

3.5 Some definitions

The definitions just presented in section 1.3 for channel flows will be adjusted for pulsating channel flows.

3.5.1 Skin friction coefficient

The streamwise shear stress, defined in Eq. (1.1), becomes for unsteady periodic flows

$$\big[\tau\big]_T = \rho\nu\left[\frac{\partial\langle u\rangle}{\partial y}\right]_T - \rho\big[\langle u'v'\rangle\big]_T, \tag{3.12}$$

where $\big[\quad\big]_T$ is the cycle-averaged operator, defined as

$$\big[\quad\big]_T = \frac{1}{T}\int_T \quad \mathrm{d}t. \tag{3.13}$$

It follows that the cycle-averaged value of the bulk skin friction coefficient is defined as

$$\big[C_f\big]_T = \frac{2\big[\tau_{\mathrm{W}}\big]_T}{\rho\big[U_b\big]_T^{\,2}}. \tag{3.14}$$

3.5.2 Drag reduction and power saving rates

According to the previous definitions, the measure of drag reduction rate R_D (Eq. 1.7) for pulsating flows becomes

$$R_D = \frac{C_{f,0} - \big[C_f\big]_T}{C_{f,0}} \times 100, \tag{3.15}$$

that is the relative change in skin friction coefficient, between the uncontrolled $C_{f,0}$ and the cycle-averaged controlled $\big[C_f\big]_T$ case.

As just discussed in 1.3.2, if an active control technique is used, the energetic cost of control has to be considered. So a new cycle-averaged bulk skin friction coefficient can be defined as

$$\big[C_f^e\big]_T = \frac{2\big[\tau_{\mathrm{w}}^e\big]_T}{\rho\big[U_b\big]_T^{\,2}}, \tag{3.16}$$

in which $\big[\tau_{\mathrm{w}}^e\big]_T$ takes into account the control energy cost.

Concerning power saving rate, the cycle-averaged power input, necessary to drive the flow, has to be redefined as

$$\big[P\big]_T = \left[Q\left\langle\frac{\partial p}{\partial x}\right\rangle_V\right]_T, \tag{3.17}$$

where Q is the volume flow rate per unit length and $\partial p/\partial x$ is the streamwise component of pressure gradient. Hence, the bulk power coefficient (Eq. (1.10)) becomes for pulsating flows

$$\big[C_P\big]_T = \frac{2\big[P\big]_T}{\rho\big[U_b\big]_T^{\,3}}. \tag{3.18}$$

It is now possible to define a new power saving rate R_P as

$$R_P = \frac{C_{P,0} - \big[C_P\big]_T}{C_{P,0}} \times 100, \tag{3.19}$$

that is the relative change in power coefficient between uncontrolled $C_{P,0}$ and cycle-averaged controlled $\big[C_P\big]_T$ case.

Chapter 4

Results

The aim of this chapter is the presentation of parametric study results. Outcomes on drag reduction and power saving will be illustrated in sections 4.1 and 4.2 respectively. In section 4.3 instead, turbulence statistics will be analysed for one chosen cycle.

Given the high computational cost, only ten cycles (actually only five for simulations having forcing period $T^+ = 3600$), for each couple of parameters (ζ,T), have been computed with the DNS. They are insufficient to obtain a realistic trend on achievable drag reduction and power saving, but suffice for this exploratory study. The main goal is to verify the possible future use of this control strategy.

Hereinafter the superscript + represents the normalization for $u_{\tau 0}$ and ν, where the subscript 0 refers to the uncontrolled field, unless otherwise indicated. Operator $\left[\quad\right]$, instead, indicates a quantity evaluated through time-averaged (on whole time history, except the first cycle) bulk velocity.

4.1 Drag reduction

Drag reduction measures the effectiveness of flow control technique. Values of R_D greater than zero assess the possibility to reach a suitable energy balance condition.

Tables 4.1, 4.2, 4.3 show cycle-averaged drag reduction rate obtained for each cycle. Considering a couple of parameters (ζ, T), it can be noted that this quantity varies a lot among different cycles. It can reach a value over 70% (proving that this control strategy can operate very well) and, immediately after, it can be negative (for instance, see table 4.3, VIII and IX cycles with $\zeta = 2.50\%$); it seems that drag reduction rate follows a random trend, so that the actual value to take into account is the mean value (the last row of tables 4.1, 4.2, 4.3). However it has to consider that ten cycles are insufficient to assess the actual trend; drag reduction rate could tend to an asymptotic value evolving the simulations.

The first cycle has been dealt with separately; in fact drag reduction rate in this cycle shows a strange behaviour compared with the other ones. This is because this cycle represents a transient phase, in which the control technique is directly applied to the fully turbulent flow; so it hasn't to be considered.

Since simulations ran with piece-wise in time CPG condition, drag reduction implies an increase of the flow rate as evident from Eqs. (3.15), (3.16) and from the definition of flow rate given in section 1.3. Figure 4.1 shows, for one chosen cycle (the last of each simulation), the flow rate trend varying duty-cycle and forcing period (whole time history can be found in the Appendix A).

A consideration has to be done on knee shown in figure 4.1 during deceleration phase. It can be attributed to the quasi-laminar decelerating flow that abruptly transitions and becomes turbulent. This is confirmed also by the peak of streamwise shear stress at top and bottom walls, as shown in figure 4.2 (its behaviour at $y = 2$ is reported in Appendix A). An initial increase due to sudden acceleration and then a decrease due to strong deceleration takes place. Near the knee, a sudden increase in streamwise shear stress at wall appears. This is an index that confirms a probable changing of flow state.

Also turbulent kinetic energy confirms this observation. In fact it shows sudden increase at the same time in which knee appears in figure 4.1 (see Appendix A).

ζ cycle	10.00%	5.00%	3.75%	2.50%	1.25%	0.50%
I	19.0	18.7	-	18.8	19.0	18.5
II	2.1	0.7	-	2.1	-0.1	1.3
III	1.3	-1.4	-	-1.1	1.5	0.7
IV	-1.6	-0.4	-	1.9	0.5	1.1
V	-2.6	-1.6	-	0.3	1.8	-0.5
[ ]	-0.2	-0.7	-	0.8	0.9	0.6

Table 4.1: R_D at $T^+ = 3600$. This table shows the value of drag reduction for each cycle, varying the duty-cycle.

4.1.1 The importance of knee in flow rate diagram for R_D

The presence of knee is important for drag reduction; in fact the later it appears, the greater cycle-averaged flow rate is, so the greater drag reduction rate is obtained. It means that probably a change of flow state is rising: the passage from

ζ cycle	10.00%	5.00%	3.75%	2.50%	1.25%	0.50%
I	-32.8	-42.2	-44.4	-47.4	-49.3	-48.2
II	52.8	54.4	13.9	49.7	38.4	16.0
III	-32.3	11.0	28.0	-16.3	-16.7	51.9
IV	14.0	-5.5	6.6	0.1	-9.6	5.6
V	11.3	55.9	0.0	61.8	7.8	19.7
VI	-19.3	-3.8	42.6	-33.6	40.3	21.3
VII	-20.5	55.1	-9.5	43.6	24.7	65.9
VIII	-21.5	-18.2	-7.7	27.3	10.5	-25.7
IX	-9.5	40.8	48.5	12.4	17.0	56.6
X	-2.1	21.6	14.2	10.0	-12.0	-22.1
[ ]	3.1	31.1	19.0	25.8	14.6	30.9

Table 4.2: R_D at $T^+ = 10800$. This table shows the value of drag reduction for each cycle, varying the duty-cycle.

ζ cycle	10.00%	5.00%	3.75%	2.50%	1.25%	0.50%
I	-	-79.3	-	-87.6	-	-
II	-	55.3	-	74.2	-	-
III	-	42.4	-	-22.6	-	-
IV	-	63.2	-	71.1	-	-
V	-	25.8	-	17.4	-	-
VI	-	46.9	-	72.2	-	-
VII	-	46.2	-	-31.2	-	-
VIII	-	48.9	-	74.4	-	-
IX	-	57.7	-	-27.7	-	-
X	-	15.2	-	73.5	-	-
[ ]	-	47.1	-	54.9	-	-

Table 4.3: R_D at $T^+ = 14400$. This table shows the value of drag reduction for each cycle, varying the duty-cycle.

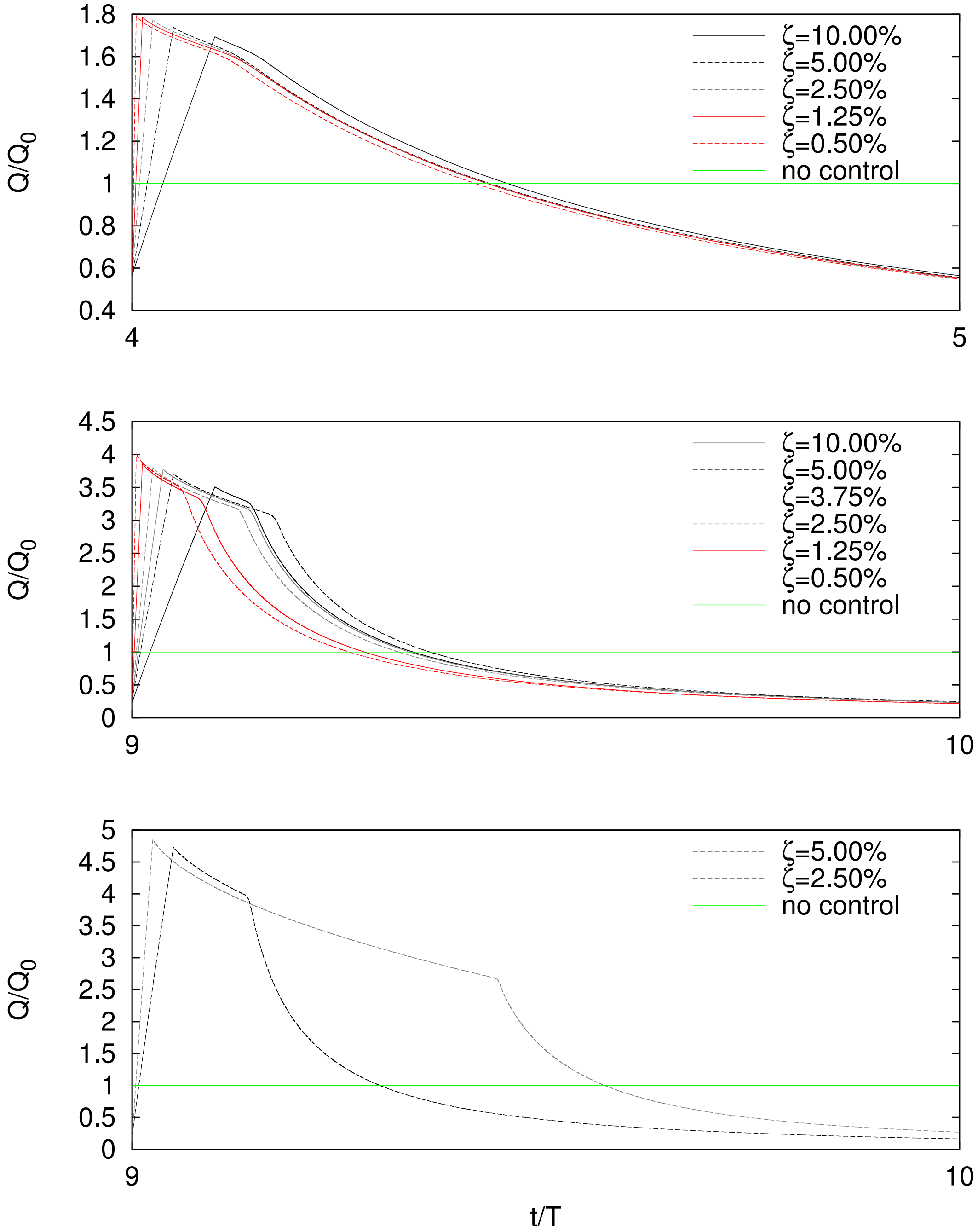

Figure 4.1: Flow rate Q normalized with the uncontrolled field value Q_0 vs time normalized with forcing period T. This figure shows a comparison (for one chosen cycle) of the effect of the duty-cycle ζ for each forcing period. Top: $T^+ = 3600$ during the V cycle. Middle: $T^+ = 10800$ during the X cycle. Bottom: $T^+ = 14400$ during the X cycle.

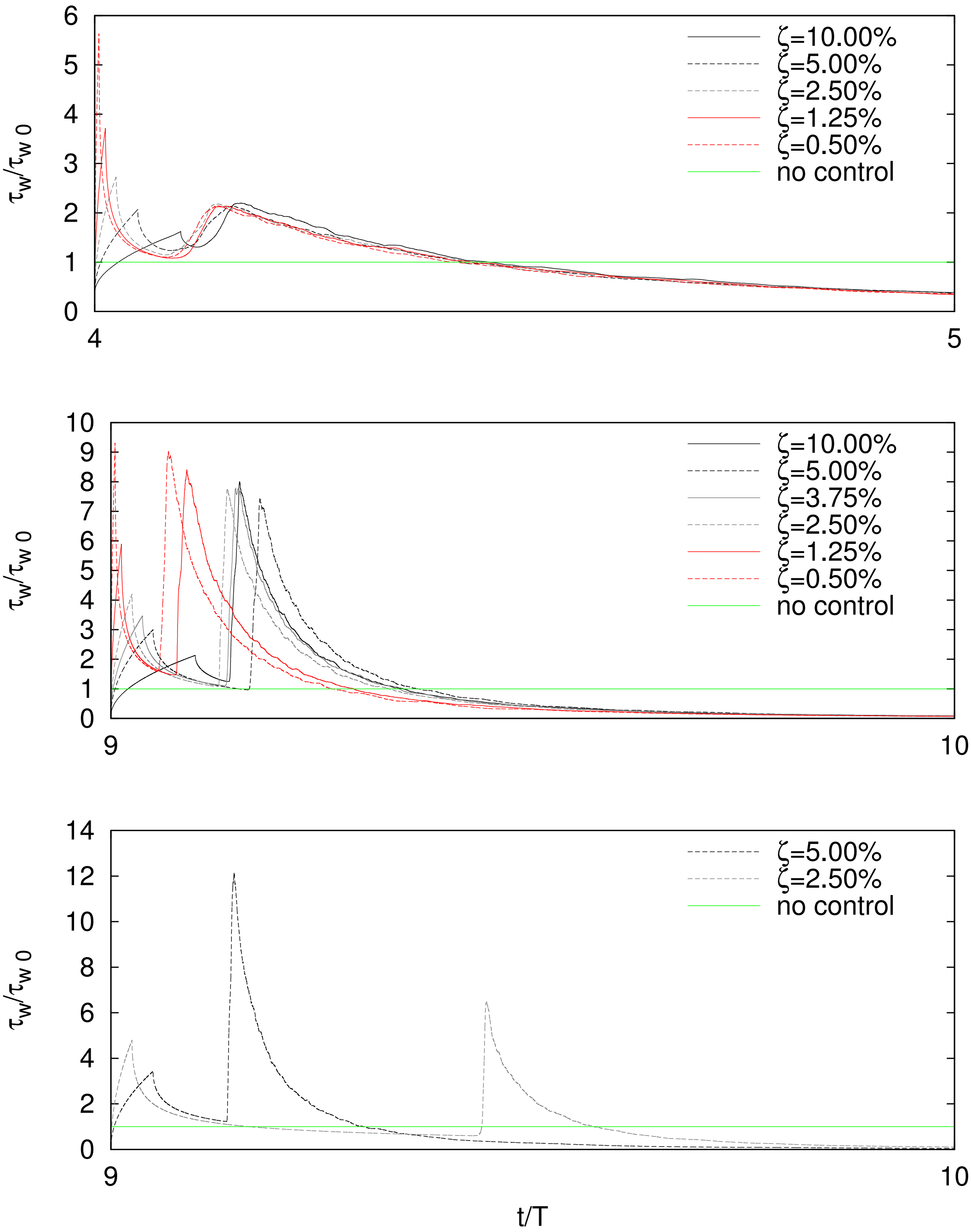

Figure 4.2: Streamwise shear stress τ_{w} at $y = 0$ normalized with the uncontrolled field value τ_{w0} vs time normalized with forcing period T. This figure shows a comparison (for one chosen cycle) of the effect of duty-cycle ζ for each forcing period studied. Top: $T^+ = 3600$ during the V cycle. Middle: $T^+ = 10800$ during the X cycle. Bottom: $T^+ = 14400$ during the X cycle.

unsteady laminar state to unsteady turbulent one. Figure 4.3 (referred to the case analysed in section 4.3) shows this change, in fact it indirectly represents the shape of velocity profile. The upper line stands for $Re_b = Re_c$; it means that velocity profile has a plug shape, whereas the lower line stands for Poiseuille flow, in which velocity profile has the typical parabolic shape. In present case, the initial acceleration corresponds to a linear growth of Re_b with Re_c as similar as plug profile. Then, when the deceleration phase starts, Re_b suddenly decreases whereas Re_c tends to keep constant-like value, that means velocity profile is taking parabolic-like shape; this is the laminar state described above. As Re_c suddenly decreases, flow instability arises and velocity profile tends to return plug-like. This phenomena will be described more in depth in section 4.3. The hysteresis of this curve could be considered as an indicator of the drag reduction. The larger is the area inside this curve, the larger drag reduction rate is. Moreover it proves an a-symmetry between acceleration and deceleration phase too, as already observed by Seddighi *et al.* in [46] and He *et al.* and Aryaratne *et al.* in [18] and [1] respectively, albeit they considered a different situation from this one.

4.1.2 The influence of forcing period

The tables 4.1, 4.2 and 4.3 show an important trend: the possibilities that this control technique operates well augment with increasing forcing period T. In fact the greatest values of drag reduction R_D have been obtained with $T^+ = 14400$. Instead, for cases with forcing period $T^+ = 3600$, its trend is bad: it seems that control technique is failing for this forcing period (for this reason, these simulations stop at the end of fifth cycle).

4.1.3 The effect of duty-cycle

Duty-cycle and, hence, intensity of flow acceleration doesn't play the same key role of forcing period. Decreasing duty-cycle ζ (increasing the negative pressure gradient intensity A), a gain in terms of drag reduction rate is not so obvious. In fact, tables 4.2 and 4.3 show that the largest gain is obtained with $\zeta = 5.00\%$ for $T^+ = 10800$ and $\zeta = 2.50\%$ for $T^+ = 14400$, as regards the time-averaged value $\left[R_D\right]$, while, considering a single cycle, the largest value is effectively obtained with the smallest duty-cycle. Instead it's clear that a too large duty-cycle causes the worst behaviour of control strategy (see $\zeta = 10.00\%$).

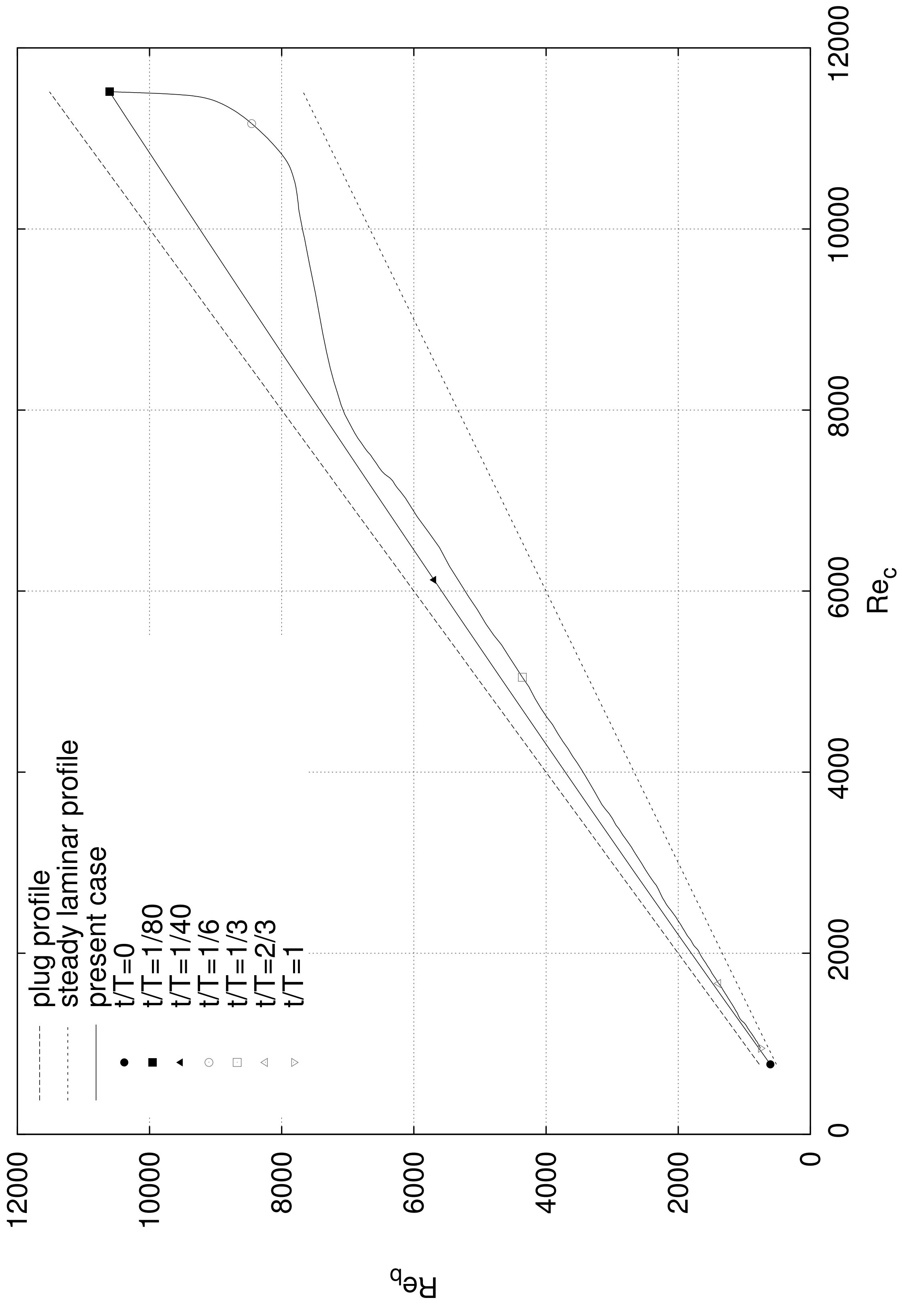

Figure 4.3: Re_b vs Re_c. The markers help understanding flow phases during forcing cycle. They will be held the same in section 4.3.

4.2 Power saving

The energy saving rate does not present as good trend as drag reduction. This is shown in tables 4.4, 4.5 and 4.6. It seems at first view that no gain from this control technique is achieved. In fact there are many cycles in which R_P is strongly negative. But there are also some cycles in which this value is strongly positive. Considering instead time-averaged value $\left[R_P\right]$, positive values are achieved only for the simulations with forcing period $T^+ = 14400$ (that highlights the considerations on forcing period influence done in previous section). It has to remember that ten cycles are insufficient to evaluate it; $\left[R_P\right]$ could reach a larger value evolving the simulations. However this important result proves that this control technique could have a good potential.

ζ cycle	10.00%	5.00%	3.75%	2.50%	1.25%	0.50%
I	-11.4	-15.5	-	-16.6	-16.4	-16.6
II	-13.6	-17.0	-	-15.3	-20.6	-19.0
III	-13.0	-17.9	-	-18.3	-14.2	-15.8
IV	-17.3	-15.6	-	-12.4	-14.9	-15.9
V	-18.6	-18.3	-	-15.6	-12.8	-14.5
$\left[\ \right]$	-15.7	-17.3	-	-15.7	-16.2	-17.9

Table 4.4: R_P at $T^+ = 3600$. This table shows the value of power saving for each cycle, varying the duty-cycle.

4.3 Turbulence statistics

In order to understand the phenomenology of this flow, this section will show the main statistical quantities that are commonly employed to describe a turbulent flow. First of all, the statistics concerning the uncontrolled flow will be shown. After that, a case in which this control technique operates with good results will be chosen (couple ($\zeta = 2.50\%$,$T^+ = 10800$) during seventh cycle) and will be analysed.

4.3.1 Uncontrolled flow

The uncontrolled flow has been evaluated by imposing a steady forcing to a turbulent channel flow at $Re_{\tau 0} = 180$. It has been compared with the simulation

ζ cycle	10.00%	5.00%	3.75%	2.50%	1.25%	0.50%
I	-247.2	-331.9	-356.8	-387.6	-412.6	-414.7
II	37.8	39.3	-59.5	28.3	2.0	-56.9
III	-201.4	-72.1	-23.1	-162.3	-165.2	30.9
IV	-52.7	-115.5	-83.1	-102.6	-136.3	-95.8
V	-61.7	41.9	-100.4	52.0	-81.7	-47.5
VI	-151.0	-118.2	13.0	-227.7	5.1	-43.9
VII	-153.3	40.3	-134.6	15.0	-35.8	58.0
VIII	-157.0	-164.1	-124.5	-28.2	-75.5	-207.2
IX	-120.0	9.3	26.0	-68.5	-56.8	40.7
X	-98.3	-40.4	-63.8	-74.7	-144.3	-189.6
[ ]	-83.9	-15.2	-47.1	-31.3	-63.1	-20.9

Table 4.5: R_P at $T^+ = 10800$. This table shows the value of power saving for each cycle, varying the duty-cycle.

ζ cycle	10.00%	5.00%	3.75%	2.50%	1.25%	0.50%
I	-	-598.5	-	-723.9	-	-
II	-	26.1	-	66.6	-	-
III	-	-10.5	-	-260.3	-	-
IV	-	44.2	-	60.5	-	-
V	-	-62.5	-	-97.6	-	-
VI	-	3.3	-	62.5	-	-
VII	-	0.7	-	-297.6	-	-
VIII	-	8.5	-	67.1	-	-
IX	-	30.9	-	-283.5	-	-
X	-	-97.5	-	65.4	-	-
[ ]	-	3.5	-	21.6	-	-

Table 4.6: R_P at $T^+ = 14400$. This table shows the value of power saving for each cycle, varying the duty-cycle.

of channel flow at the same Reynolds number computed by Vreman *et al.* in [62]. This turbulent field has been chosen as initial condition of the simulations run with the pulsating forcing and will be used in the next sections as reference case for evaluating the action of control strategy. The top and bottom pictures of figure 4.4 show, respectively, the mean velocity profile $\langle u \rangle$ and the turbulent fluctuations.

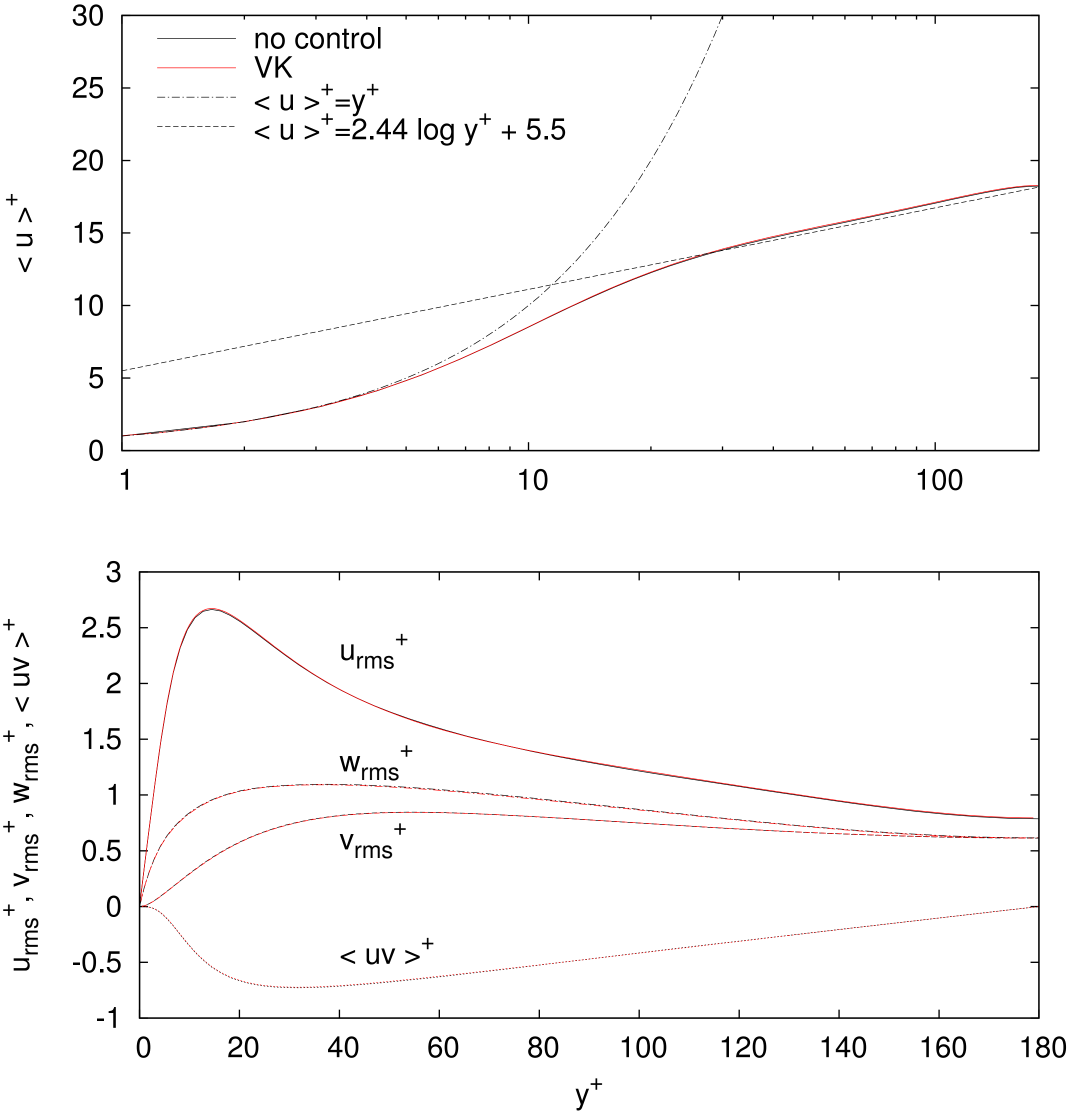

Figure 4.4: Top: mean velocity profile in semi-logarithmic scale of present uncontrolled case and Vreman *et al.* simulation [62] vs wall-normal coordinate. Bottom: turbulent fluctuations of present uncontrolled case (black curves) and Vreman *et al.* simulation [62] (red curves) vs wall-normal coordinate.

4.3.2 Controlled flow: mean velocity profile

Before dealing with the turbulence statistics of the controlled flow, to help the reader identify the phase during the cycle at which statistics are being considered, we show the figure with markers (that will be held the same in the subsequent figures) of the flow rate trend for the analysed case (figure 4.5).

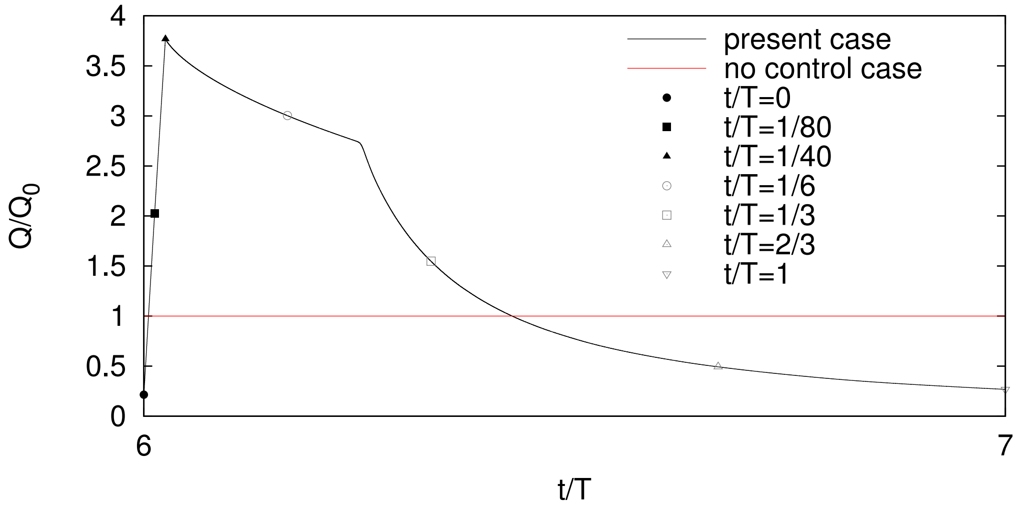

Figure 4.5: Streamwise flow rate normalized with the uncontrolled field value Q_0 vs time normalized with the forcing period T.

Mean velocity profiles $\langle u \rangle$ at various time instants are shown in figure 4.6. During the acceleration phase (black curves), these profiles are very plug-like. The third curve represents the mean velocity profile at the end of the acceleration phase, in which the maximum centreline velocity is reached ($U_c/u_{\tau 0} = 63.97$). After that, the first part of deceleration phase is characterized by a slow decrease of the centreline velocity whereas the mean velocity profile assumes a parabolic-like shape (see the fourth curve in figure 4.6, top picture): it corresponds to the laminar state. Past the knee, the profiles tend to return plug-like. The bottom picture of figure 4.6 shows the same profile at time instants in closely proximity of the transition instant. These considerations are also reflected in figure 4.3.

Another important consideration regards the near wall behaviour. The slope of profiles tends to increase during acceleration phase, while during deceleration it decreases. A particular tendency is shown between the laminar phase and the turbulent one (i.e. before and after the rise of the flow instability). In fact the laminar profile has a lower slope than the turbulent one; it means that, immediately before and after the knee instant, the slope tends to an initial increase and then decreases up to the minimum value at the end of the cycle, as confirmed in figure 4.6, bottom picture. This reflects the behaviour of the wall shear stress described in the previous section and shown in figure 4.2.

A last consideration regards the difference between cycle-averaged and uncontrolled mean velocity profiles. It directly shows how much this control technique increments streamwise flow rate (important for drag reduction and power saving).

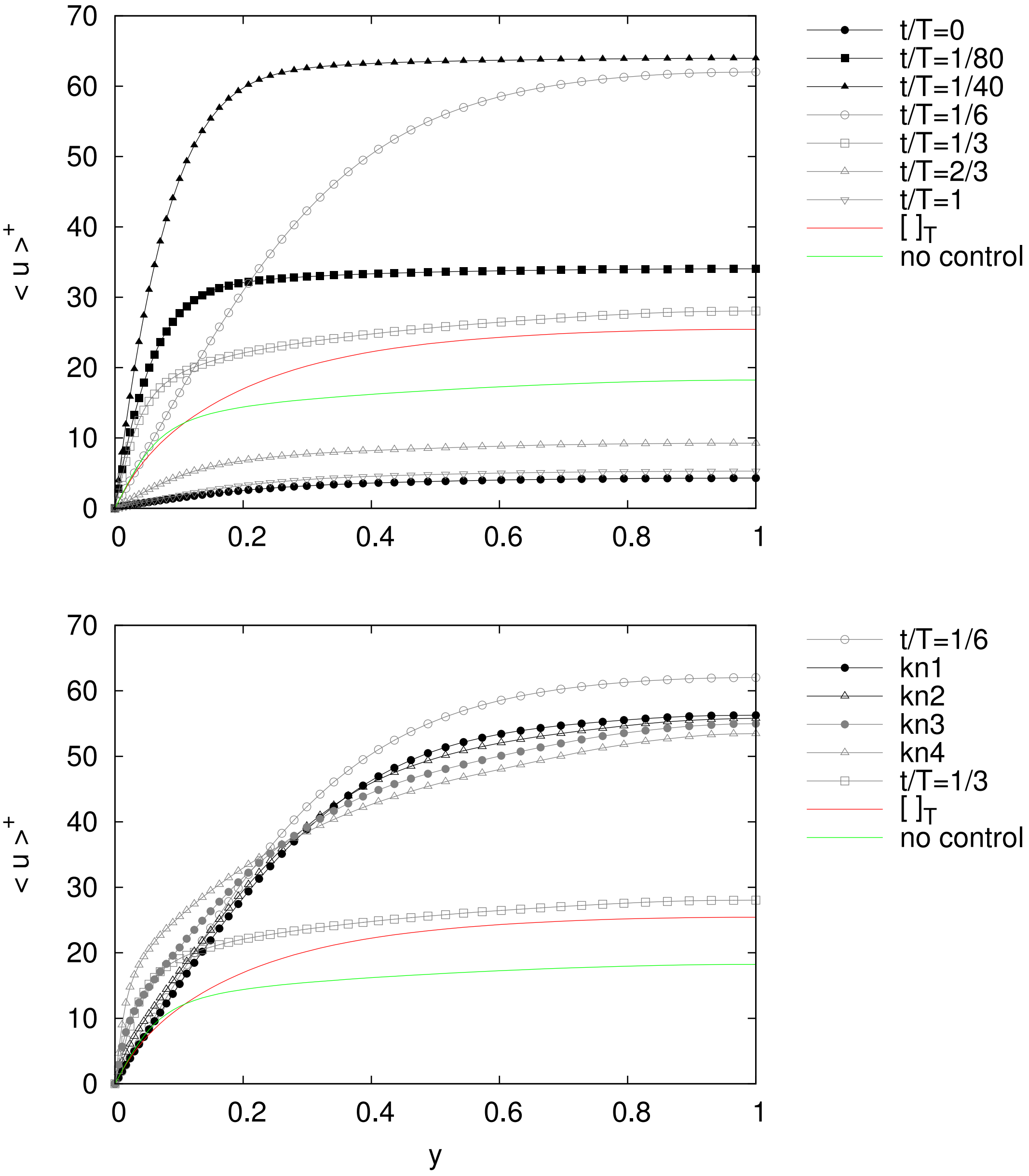

Figure 4.6: Top: mean velocity profiles during forcing period vs wall-normal coordinate. Bottom: mean velocity profiles during the rise of the flow instability vs wall-normal coordinate. The black curves (kn1 and kn2) represent the flow condition just before the knee, whereas the gray ones (kn3 and kn4) the condition soon after. For both figures, the green curve refers to uncontrolled flow.

Figure 4.7 shows cycle-averaged mean velocity profile in semi-logarithmic scale. This figure shows that mean velocity profile of the uncontrolled case is more plug-like than present one. This last doesn't follow the logarithmic law $\langle u\rangle^+ = (1/\kappa)\log y^+ + B$, with $\kappa = 0.41$ and $B = 5.5$, but still shows a logarithmic region with a slope $1/\kappa$ ($\kappa = 0.129$) and with an offset $B = -10.9$. Moreover the figure shows how the profile in the linear sublayer closely follows the classic law-of-the-wall behaviour $\langle u\rangle^+ = y^+$. It means that control strategy doesn't act on cycle-averaged velocity profile in this region. This is a non-trivial result that shows the particularity of this flow type.

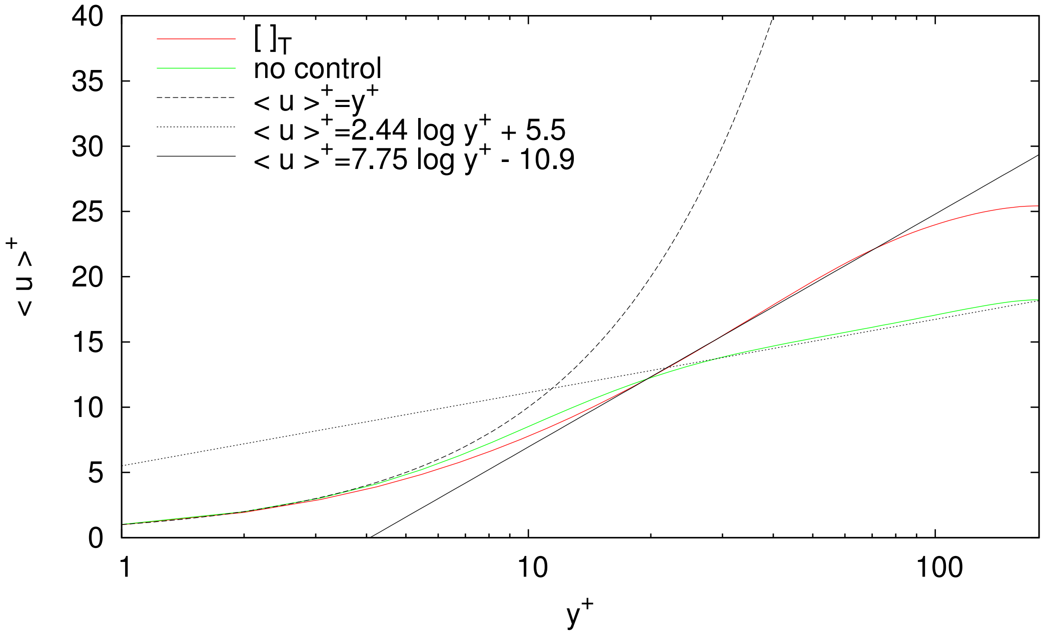

Figure 4.7: Cycle-averaged mean velocity profile in semi-logarithmic scale vs wall-normal coordinate. The green curve refers to uncontrolled flow.

4.3.3 Controlled flow: turbulent fluctuations

In figures 4.8 and 4.9, comparison between the wall-normal profiles of rms (root-mean-square) values of velocity fluctuations is presented as a function of wall-normal distance. Normalization has been made first with respect to the initial friction velocity $u_{\tau 0}$ (figures 4.8 and 4.9, on the left), then with respect to the instantaneous friction velocity u_τ (figures 4.8 and 4.9, on the right).

The cycle-averaged curve is of particular interest: in fact it seems qualitatively close to uncontrolled case one (although more shifted towards the wall and smaller in log-law region) for wall-normal and spanwise components, whereas it radically changes concerning the streamwise one. This last is particularly affected by what happens during laminar phase. For the other components, instead, their value during this phase is the smallest reached during the cycle, while suddenly rises when flow instability develops itself (figure 4.9).

Figures 4.10 and 4.11, instead, show the off-diagonal components of Reynolds stress tensor. The normalization has been again made first with respect to the square initial friction velocity ${u_\tau}_0^2$ (left part), then with respect to the square instantaneous friction velocity u_τ^2 (right part).

Particular attention needs to be paid to $\left[u'v'\right]_T$, that represents the turbulent component of streamwise shear stress. Figure 4.10 shows how the control strategy drastically reduces its value in the log-law region (a more in depth discussion about this theme follows in the next section).

A last consideration concerns the acceleration phase: all these figures show, as expected, how strong acceleration suppresses the turbulent fluctuations.

4.4 Streamwise shear stress

Figure 4.12 shows the comparison between cycle-averaged and uncontrolled flow streamwise shear stress. The former is estimated through relation Eq. 3.12, whereas the latter through Eq. 1.1. There is a big difference between the Reynolds shear stress in present case and in uncontrolled one; it means that this control increases the viscous component of the shear stress breaking down the turbulent one. The little difference between total component and respective analytical curve, instead, can be attributed to numerical approximation error due to the short time (forcing period), respect with the strong variation of the flow quantities, over which the mean velocity profile is averaged.

Figure 4.13 shows how the shear stress varies during the forcing period. It highlights that, during the acceleration phase, the maximum value is reached at wall, whereas during the deceleration this is not true (this is clear in bottom figure 4.13). Moreover top figure 4.13 follows the same trend obtained by Iwamoto *et al.* in [19].

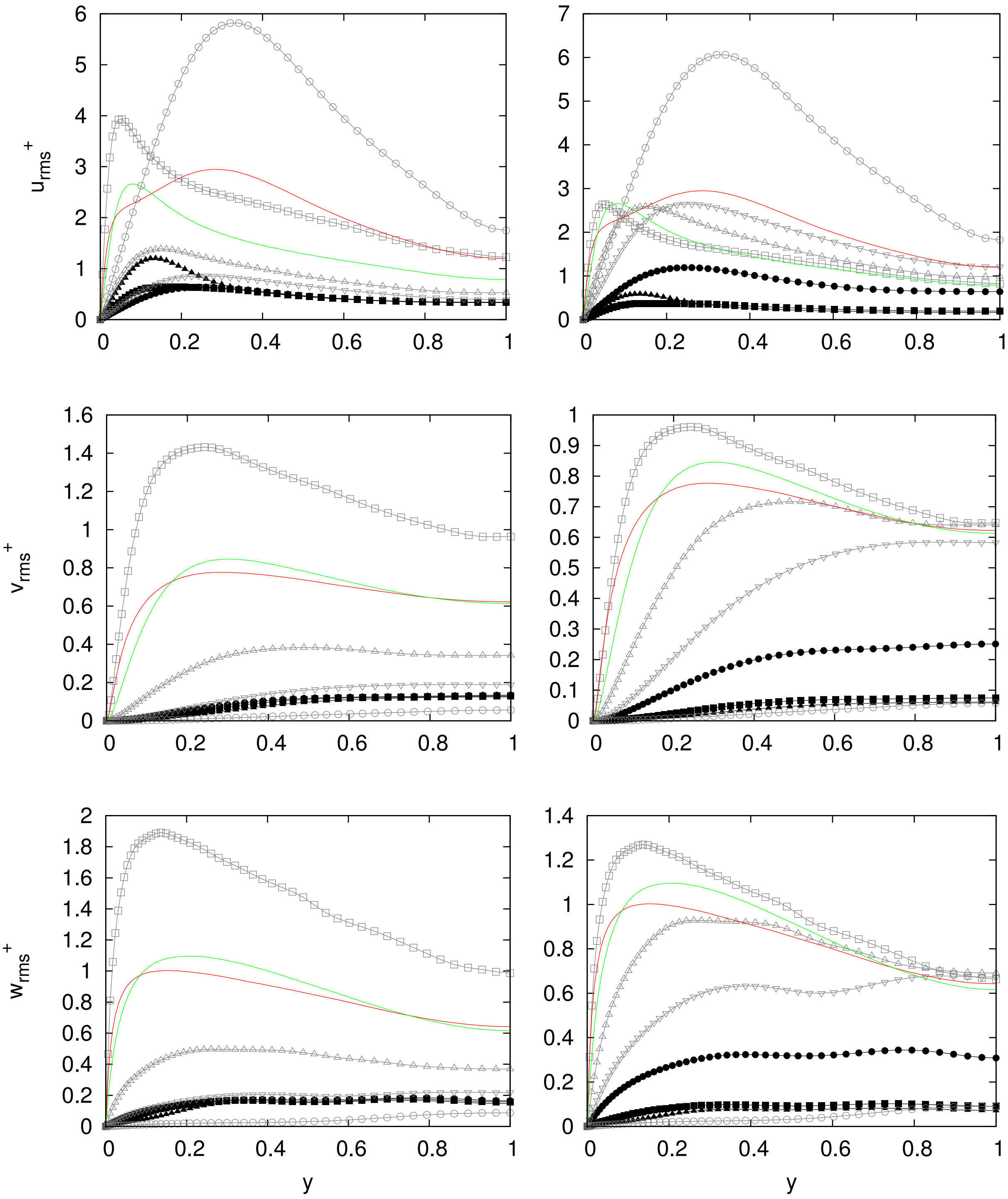

Figure 4.8: RMS of the diagonal components of Reynolds stress tensor during forcing period vs wall-normal coordinate. The left part is normalized with $u_{\tau 0}^2$, whereas the right one with instantaneous u_τ^2. The green curve refers to uncontrolled flow. The legend, that is the same of the top picture of figure 4.6, here has been omitted to lighten the image.

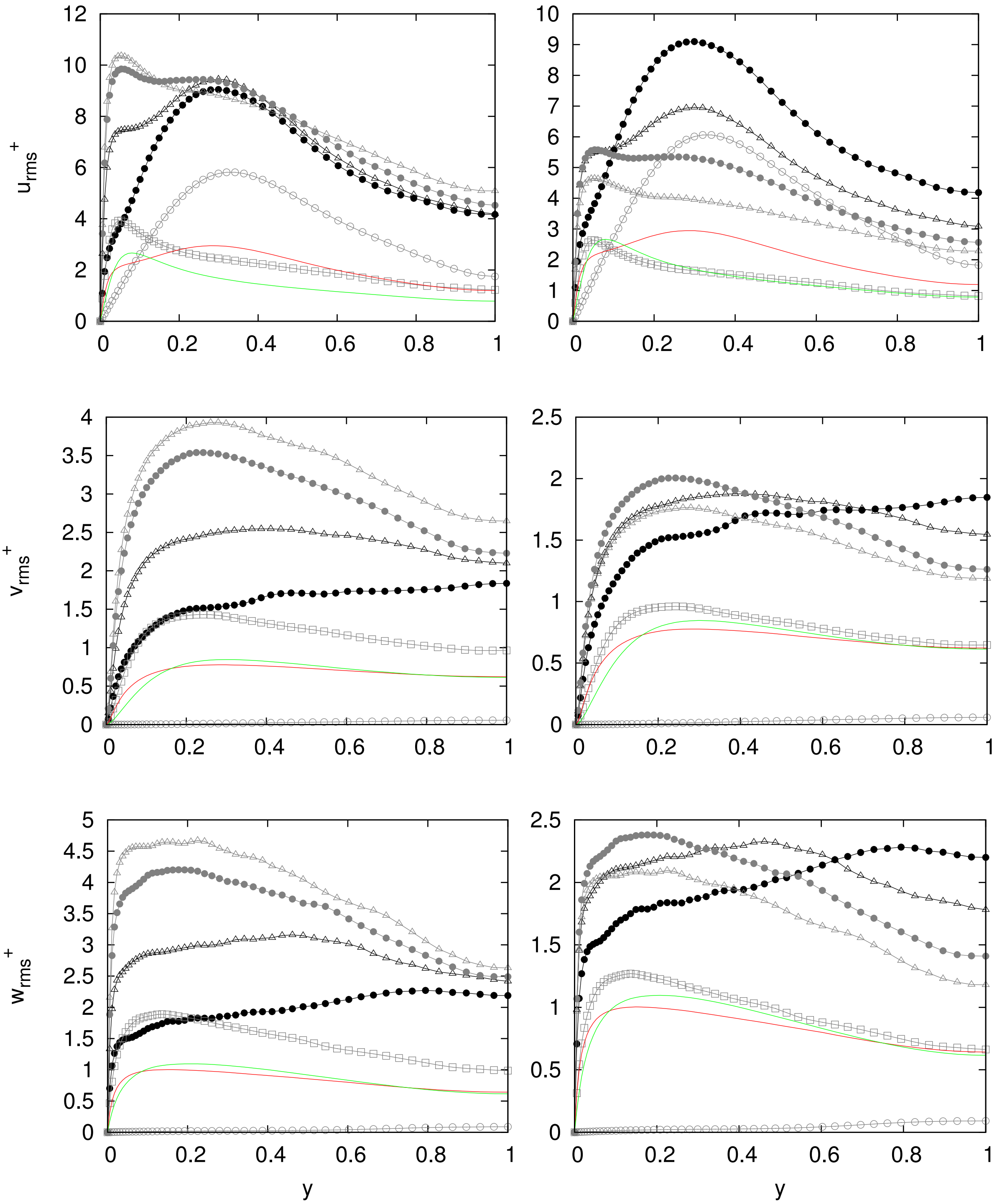

Figure 4.9: Focus around the knee: RMS of the diagonal components of Reynolds stress tensor during forcing period, vs wall-normal coordinate. The left part is normalized with ${u_{\tau 0}}^2$, whereas the right one with instantaneous u_τ^2. The green curve refers to uncontrolled flow. The legend, that is the same of the bottom picture of figure 4.6, here has been omitted to lighten the image.

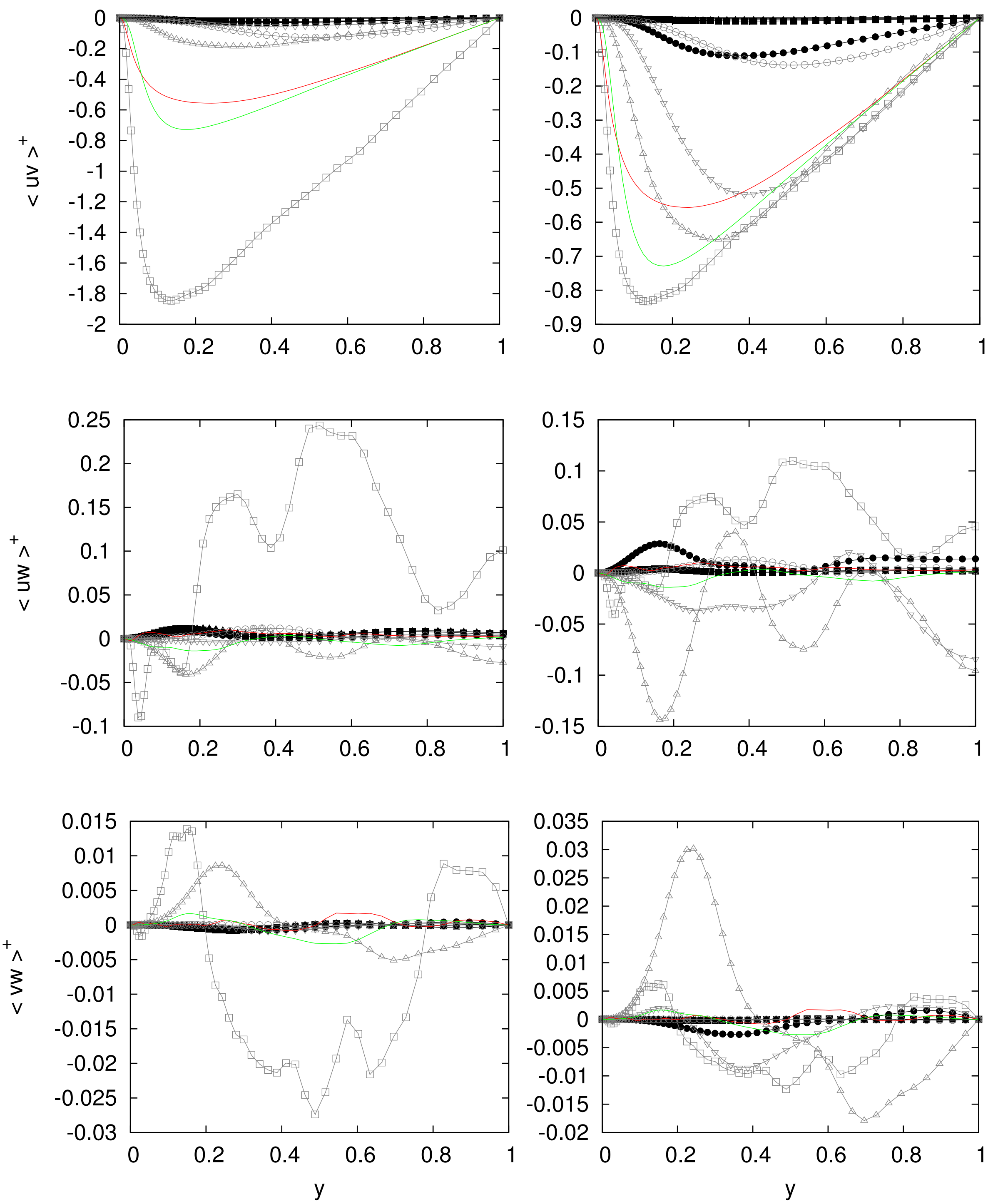

Figure 4.10: Off-diagonal components of Reynolds stress tensor during forcing period vs wall-normal coordinate. The left part is normalized with $u_{\tau 0}^2$, whereas the right one with instantaneous u_τ^2. The green curve refers to uncontrolled flow. The legend, that is the same of the top picture of figure 4.6, here has been omitted to lighten the image.

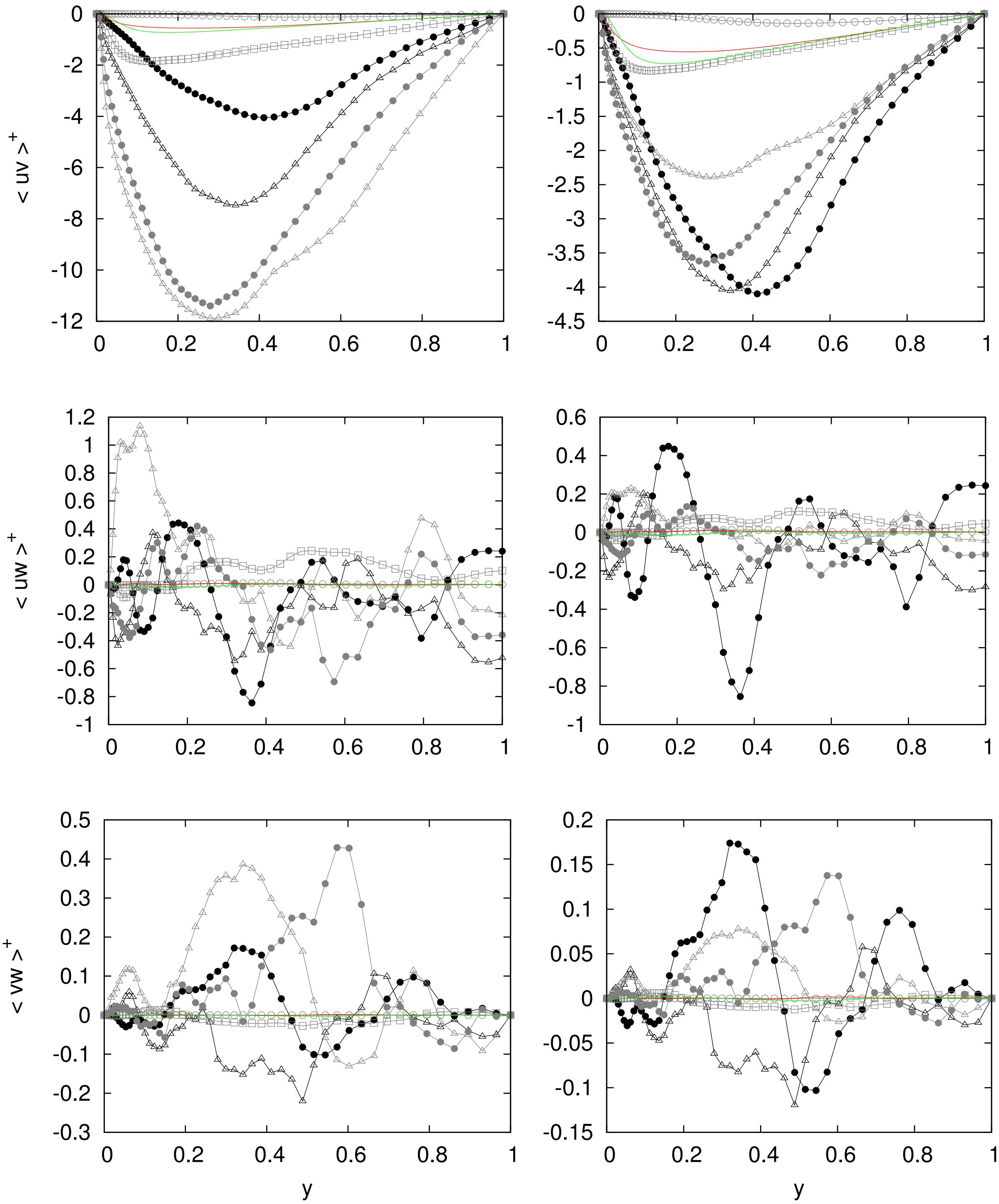

Figure 4.11: Focus around the knee: off-diagonal components of Reynolds stress tensor varying the time phase vs wall-normal coordinate. The left part is normalized with ${u_{\tau 0}}^2$, whereas the right one with instantaneous u_τ^2. The green curve refers to uncontrolled flow. The legend, that is the same of the bottom picture of figure 4.6, here has been omitted to lighten the image.

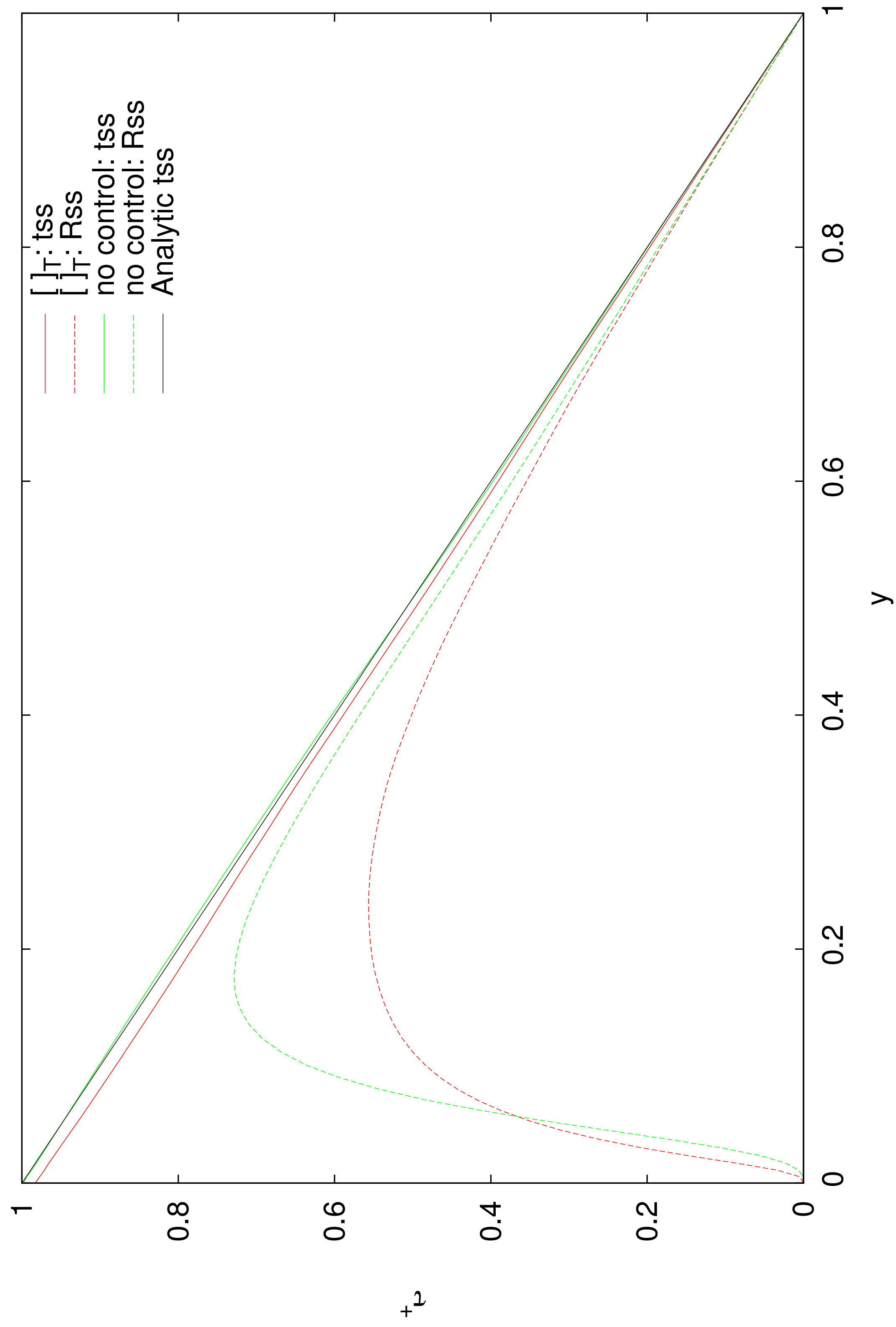

Figure 4.12: Streamwise shear stress vs wall-normal coordinate. Here, tss stands for total shear stress and Rss for Reynolds component shear stress. The green curve refers to uncontrolled flow.

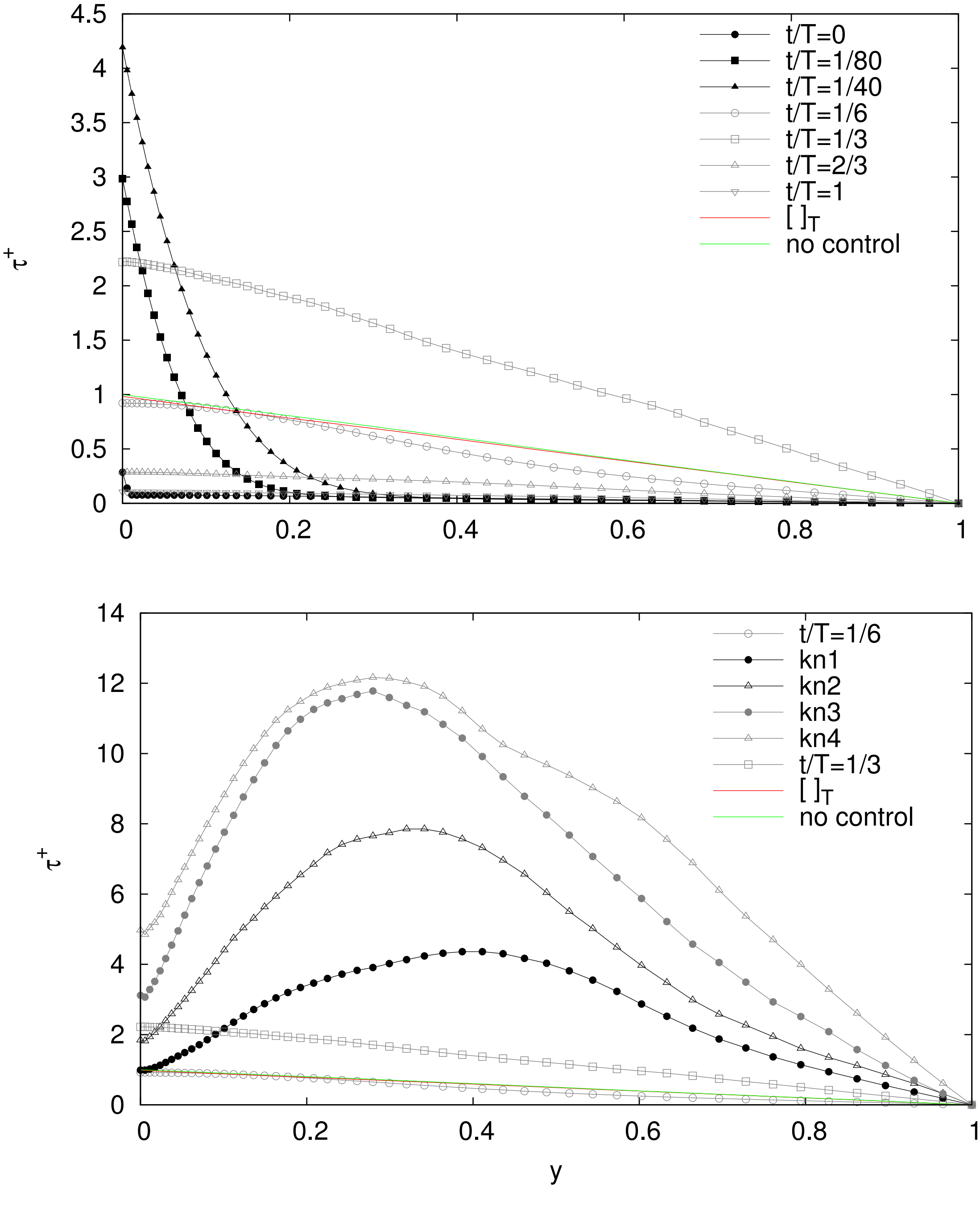

Figure 4.13: Streamwise shear stress during forcing period vs wall-normal coordinate. The bottom figure shows the quantities around the knee. The green curve refers to uncontrolled flow.

Chapter 5

Conclusions and future work

The present study has dealt with the response of a turbulent channel flow to a pulsating pressure gradient. The time evolution of the forcing follows a step function, and its amplitude has been designed such that the cycle-averaged forcing is unchanged respect with the uncontrolled flow.

A parametric study has been carry out to investigate the effects of forcing period and forcing amplitude (equivalent to duty-cycle) and to understand how this control strategy acts on the turbulent flow. The study has been done through Direct Numerical Simulations, run at $Re_\tau = 180$. Their computational cost is exceeding large, owing to their duration, as the effective forcing periods are long and there is a need for averaging results over a number of them. Discretization effects have been preliminarily considered and so far it seems that the qualitative picture we are obtaining is reliable. It has been possible to compute only ten forcing cycles for the most interesting cases, so that, overall, performance figures should be interpreted with care.

Besides limited statistical sampling, another limitation of the present study is the limited relevant information that is available in the open literature, concerning pulsating flows with drag reduction and power saving. In fact only Iwamoto *et al.*, in [19] and [20], and Souma *et al.*, in [52], have addressed these possibilities, although in a setting which is significant different from ours. More relevant, but only for a spatial aspect of the study, are those studies that concern accelerating and decelerating flows.

Overall, the goal set for this work was to verify the interest of this concept, and this goal has been fully achieved. Although the parameter set is very large and we have set sampled it very sparsely, we already observed drag reduction and net savings of about 70% for single forcing cycles, and smaller but still very interesting values after whole time-averaging. A preliminary analysis of a few flow statistics suggests that the working mechanism of this control technique resides in an hysteresis loop between the laminar flow created during the acceleration phase and the turbulent flow that takes place at some time during the deceleration stage.

Much remains to be done. For example, only a much longer run time would give reliable figures for drag reduction and net savings. It is probable that different parameters allow much better performance, but the parameter space has to be scanned thoroughly. Another possible development consists in modifying the simple step-function forcing shape, aiming at a ramp-down deceleration to possibly retard the development of the flow instability. Finally, interesting work should consist in analysing behaviour of this control technique at high Reynolds numbers with using LES or RANS, to verify its potential for industrial applications.

Appendix A

Other figures

A.1 DNS code validation

A.1.1 Resolution check

At Reynolds number $Re_{\tau 0} = 180$, the grid chosen in y-direction could be coarse. So two simulations which differ only in N_y have been launched, starting from the same initial field, to verify the results aren't qualitatively influenced by mesh resolution in y-direction.
In table A.1 the parameters used in the two simulations are shown.

	Simulation	
	1	2
L_x	$3/2\pi$	$3/2\pi$
L_y	2	2
L_z	π	π
N_x	96	96
N_y	100	200
N_z	96	96
a	1.6	1.6

Table A.1: Channel domain for studying resolution problem in y-direction.

The domain size used here is smaller than one described above. In this way it is possible to use a smaller number of modes in homogeneous directions and hence to reduce the very expensive computational cost. It is important to keep in mind that, here, unique real interest is to evaluate influence of the number of points used in wall-normal direction.

For these simulations a pulsating forcing (Eq. (3.8)) with period $T^+ = 5400$ (where the time superscripted + hereinafter stands for the normalization with $u_{\tau 0}$ and ν) and duty-cycle $\zeta = 2.50\%$ is imposed.

Comparison of flow quantities

In figure A.1, the mean flow rate is shown for the two simulations. It is worth noticing that the two curves are qualitatively the same. Only second and third cycles are little bit different. This trend is also confirmed for turbulent kinetic energy (integrated over wall-normal direction) and streamwise shear stress at both walls (figures A.2 and A.3, A.4 respectively).

It can be concluded that choosing $N_y = 100$ won't qualitatively influence reliability of simulation outcomes.

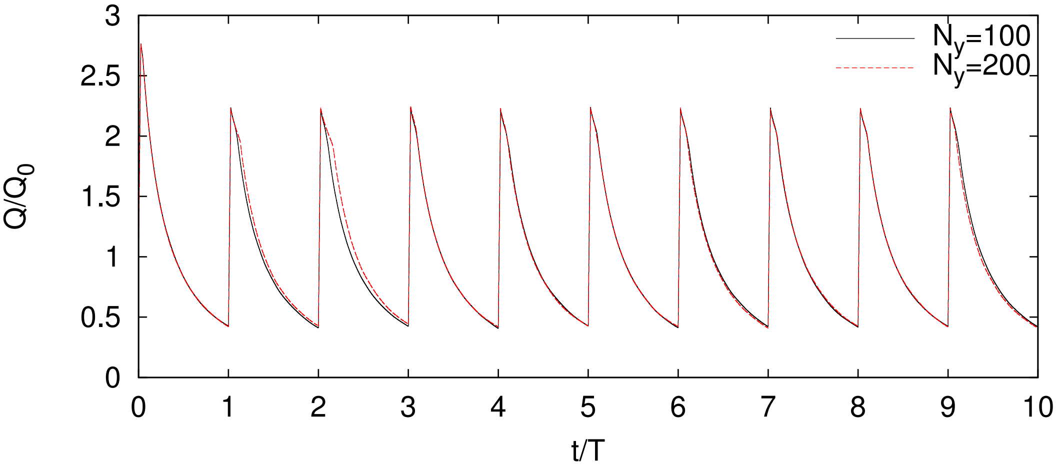

Figure A.1: Flow rate normalized with the uncontrolled field value Q_0 vs time normalized with the forcing period T.

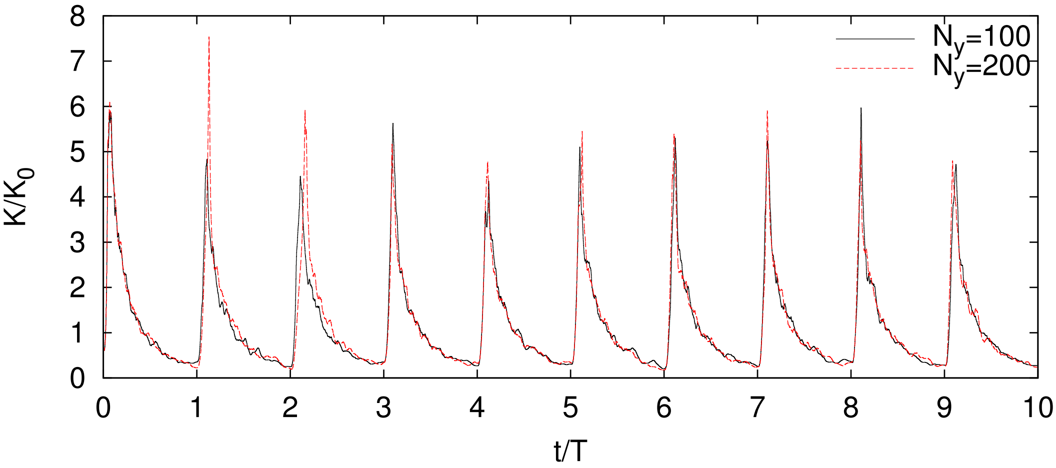

Figure A.2: Turbulent kinetic energy per unit mass integrated over the wall-normal direction $K = \int_0^2 k \, \mathrm{d}y$, normalized with the uncontrolled field value K_0 vs time normalized with the forcing period T.

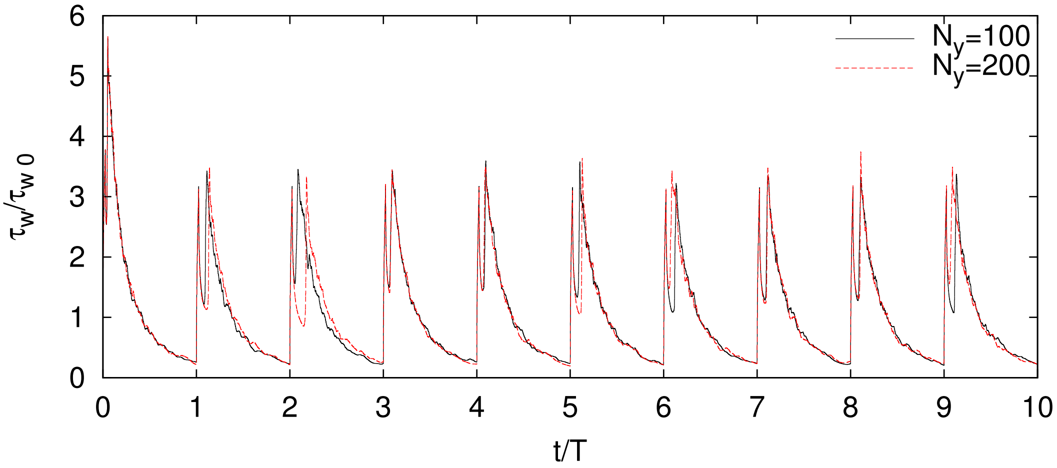

Figure A.3: Streamwise shear stress at $y = 0$, normalized with the uncontrolled field value $\tau_{\mathrm{w}0}$ vs time normalized with the forcing period T.

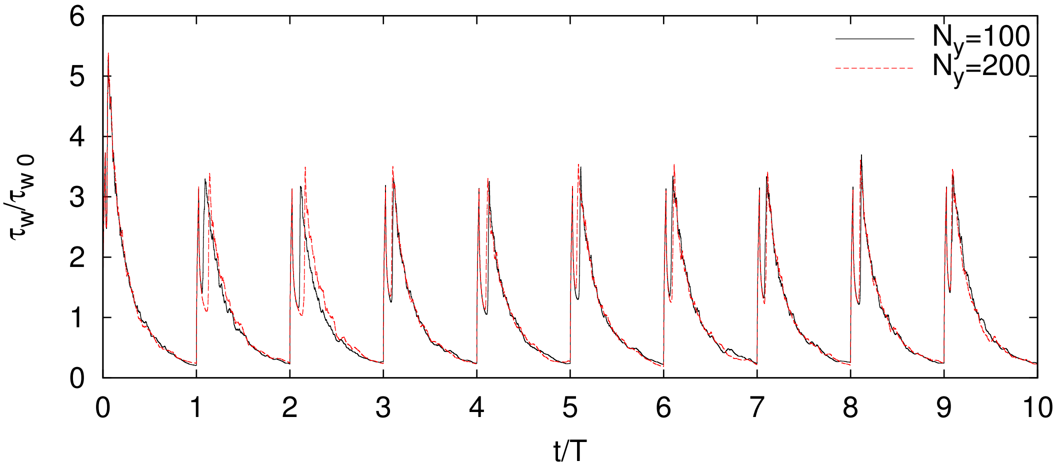

Figure A.4: Negative streamwise shear stress at $y = 2$, normalized with the uncontrolled field value $-\tau_{\mathrm{w}0}$ vs time normalized with the forcing period T.

A.2 Parameters comparison

In this section, the time history of flow quantities will be firstly presented for each couple of parameters (ζ,T). The first cycle hasn't to be considered because it represents a firstly transient condition, in which the control technique is directly applied to the fully turbulent flow. Then, for one chosen cycle, a direct comparison varying duty-cycle ζ and forcing period T will be shown for streamwise shear stress at $y = 2$ (figure A.25) and turbulent kinetic energy (figure A.26).

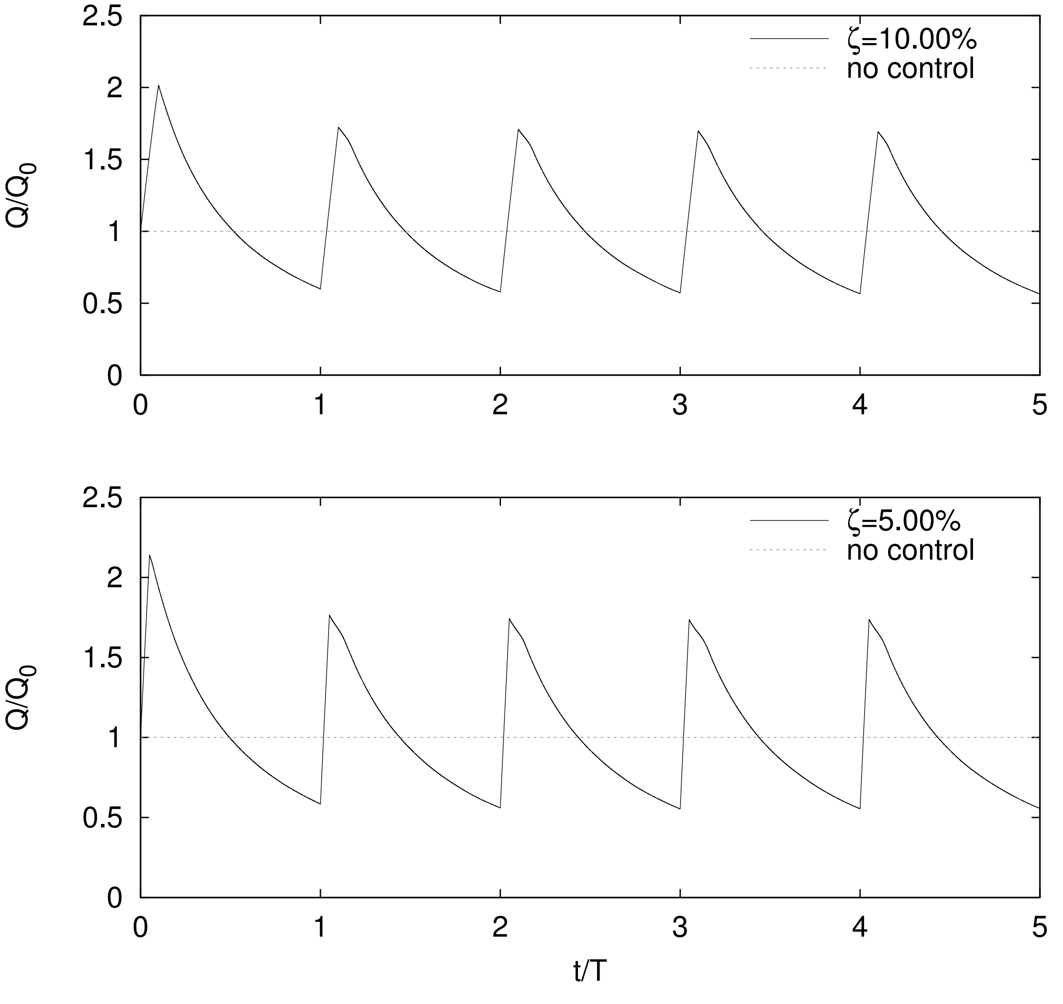

Figure A.5: Flow rate normalized with the uncontrolled field value Q_0 vs time normalized with the forcing period T. This figure shows its trend during time history for each couple of parameters (ζ,$T^+ = 3600$).

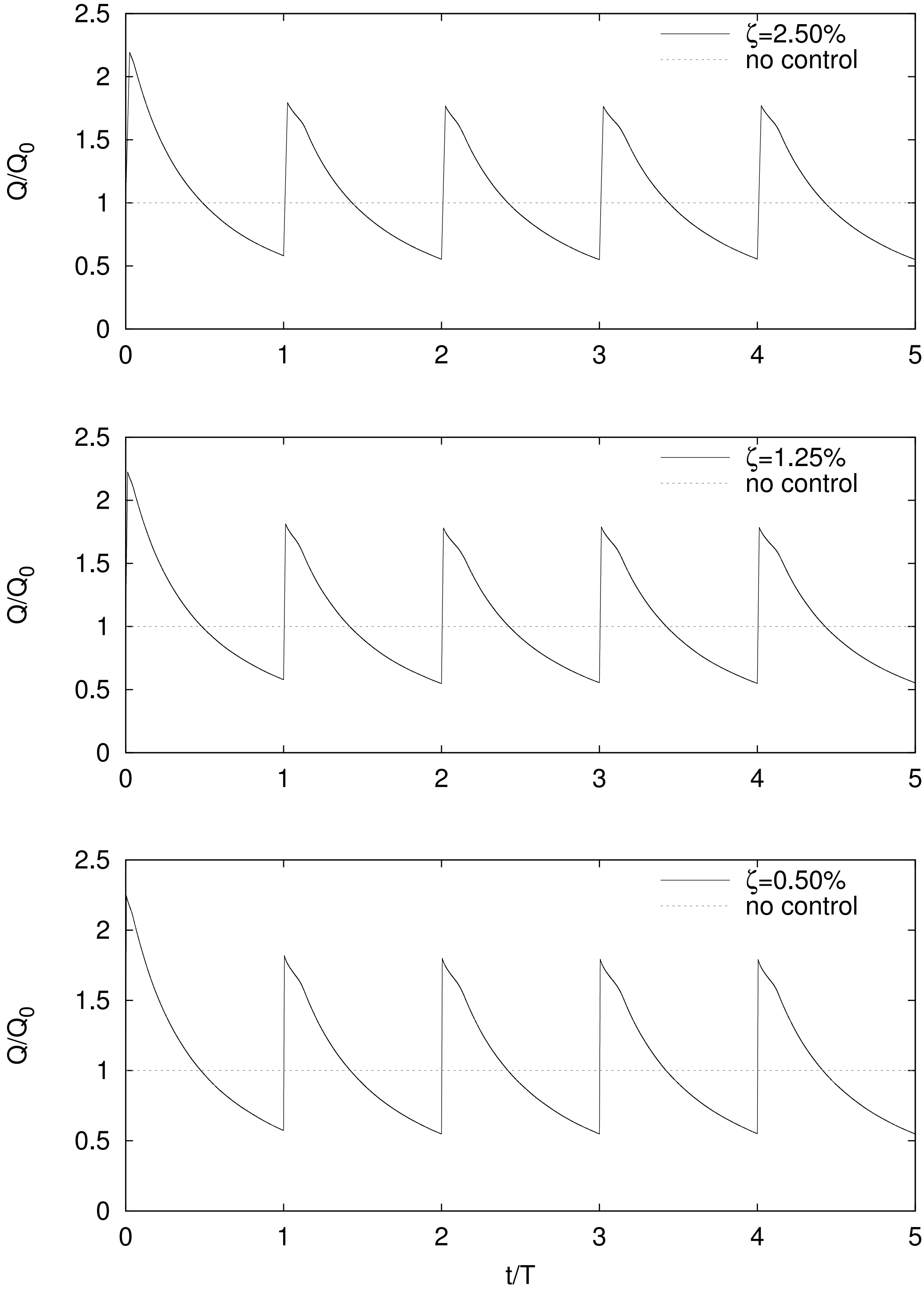

Figure A.6: Flow rate normalized with the uncontrolled field value Q_0 vs time normalized with the forcing period T. This figure shows its trend during time history for each couple of parameters (ζ,$T^+ = 3600$).

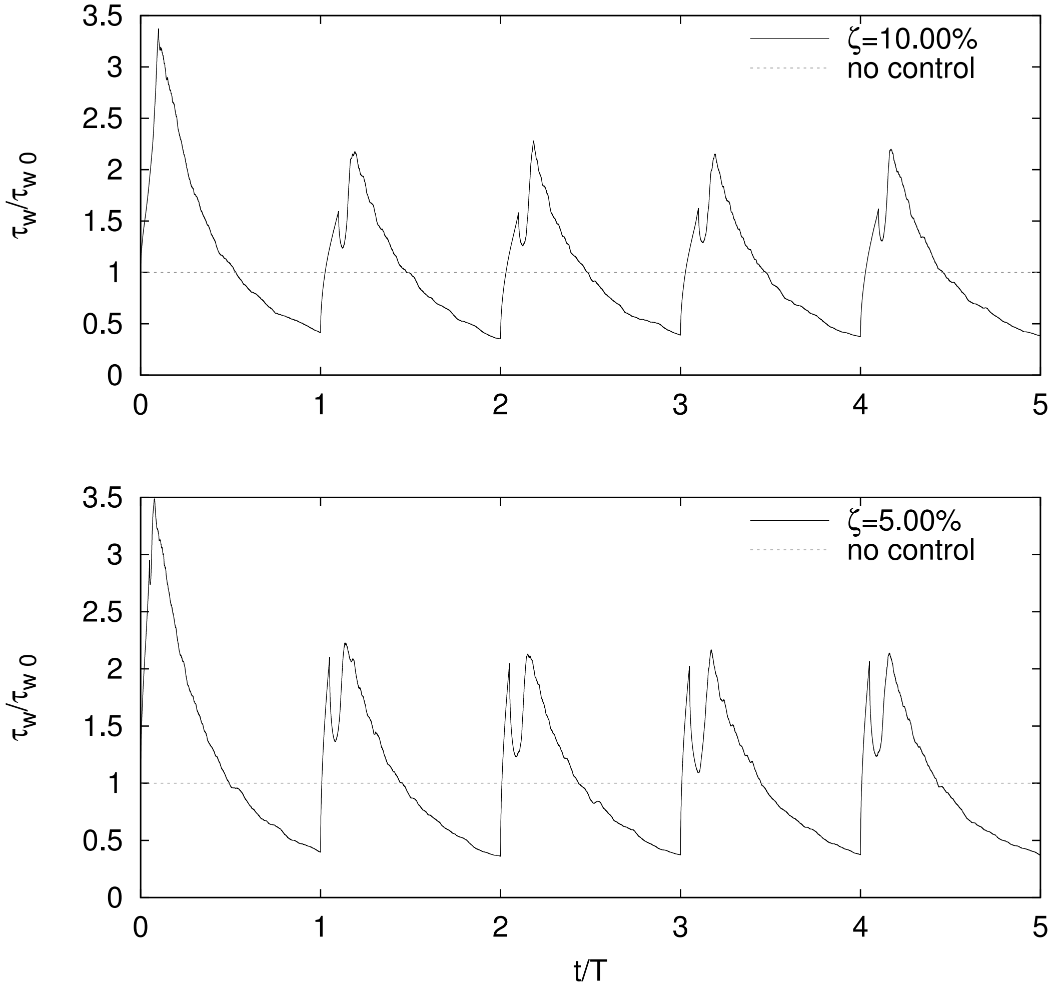

Figure A.7: Streamwise shear stress at $y = 0$, normalized with the uncontrolled field value $\tau_{\mathrm{w}0}$ vs time normalized with the forcing period T. This figure shows its trend during time history for each couple of parameters (ζ,$T^+ = 3600$).

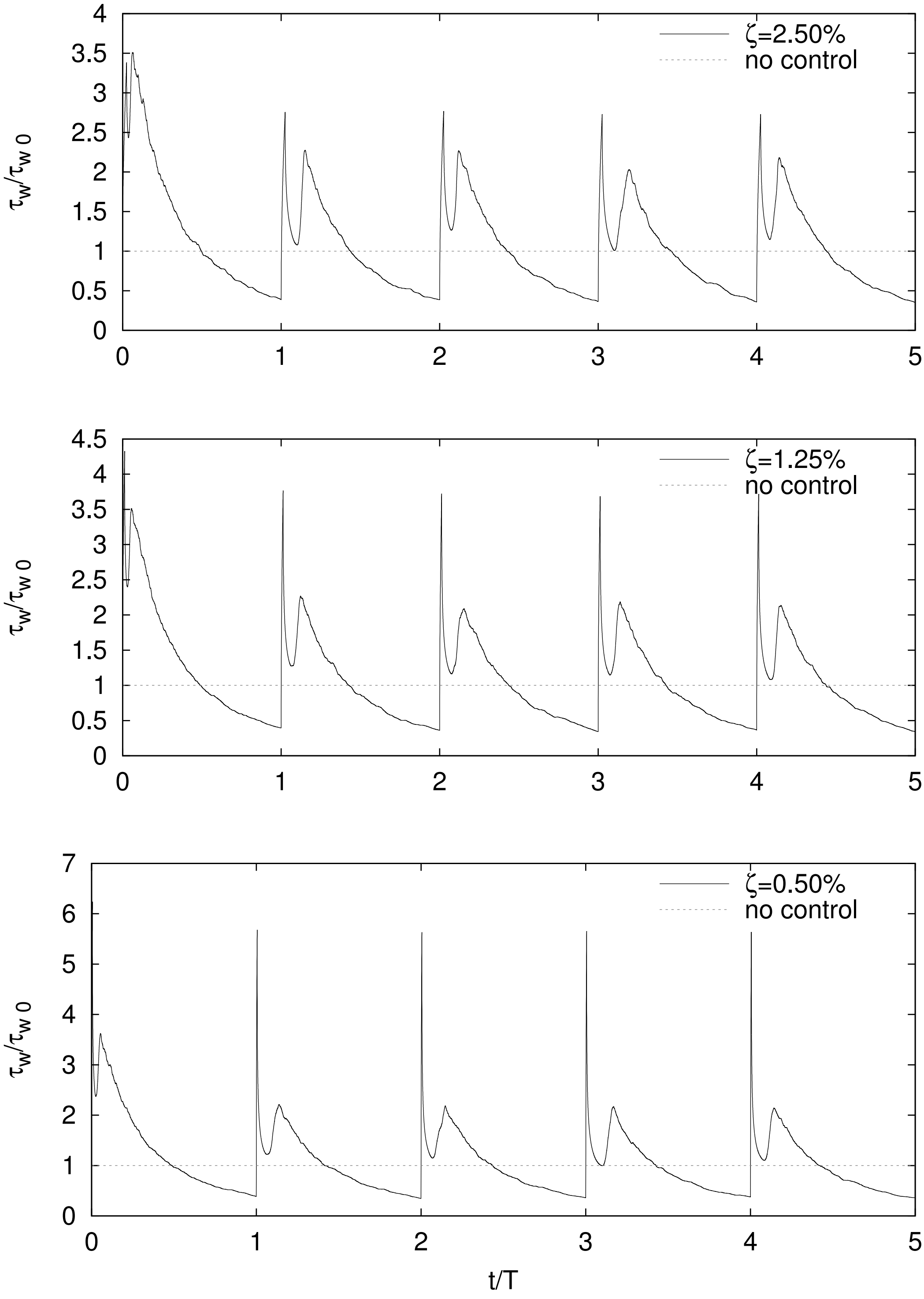

Figure A.8: Streamwise shear stress at $y = 0$, normalized with the uncontrolled field value τ_{w0} vs time normalized with the forcing period T. This figure shows its trend during time history for each couple of parameters (ζ,$T^+ = 3600$).

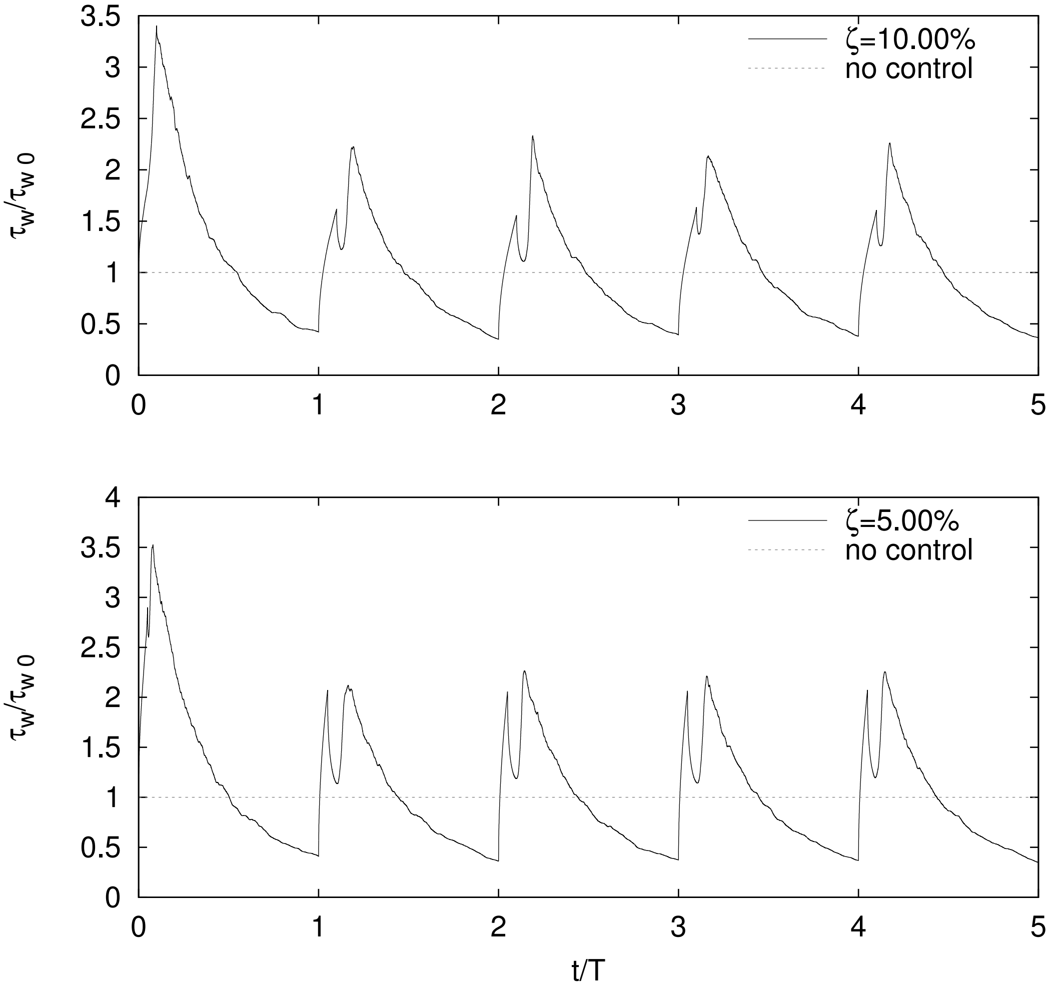

Figure A.9: Negative streamwise shear stress at $y = 2$, normalized with the uncontrolled field value $-\tau_{\mathrm{w}0}$ vs time normalized with the forcing period T. This figure shows its trend during time history for each couple of parameters (ζ,$T^+ = 3600$).

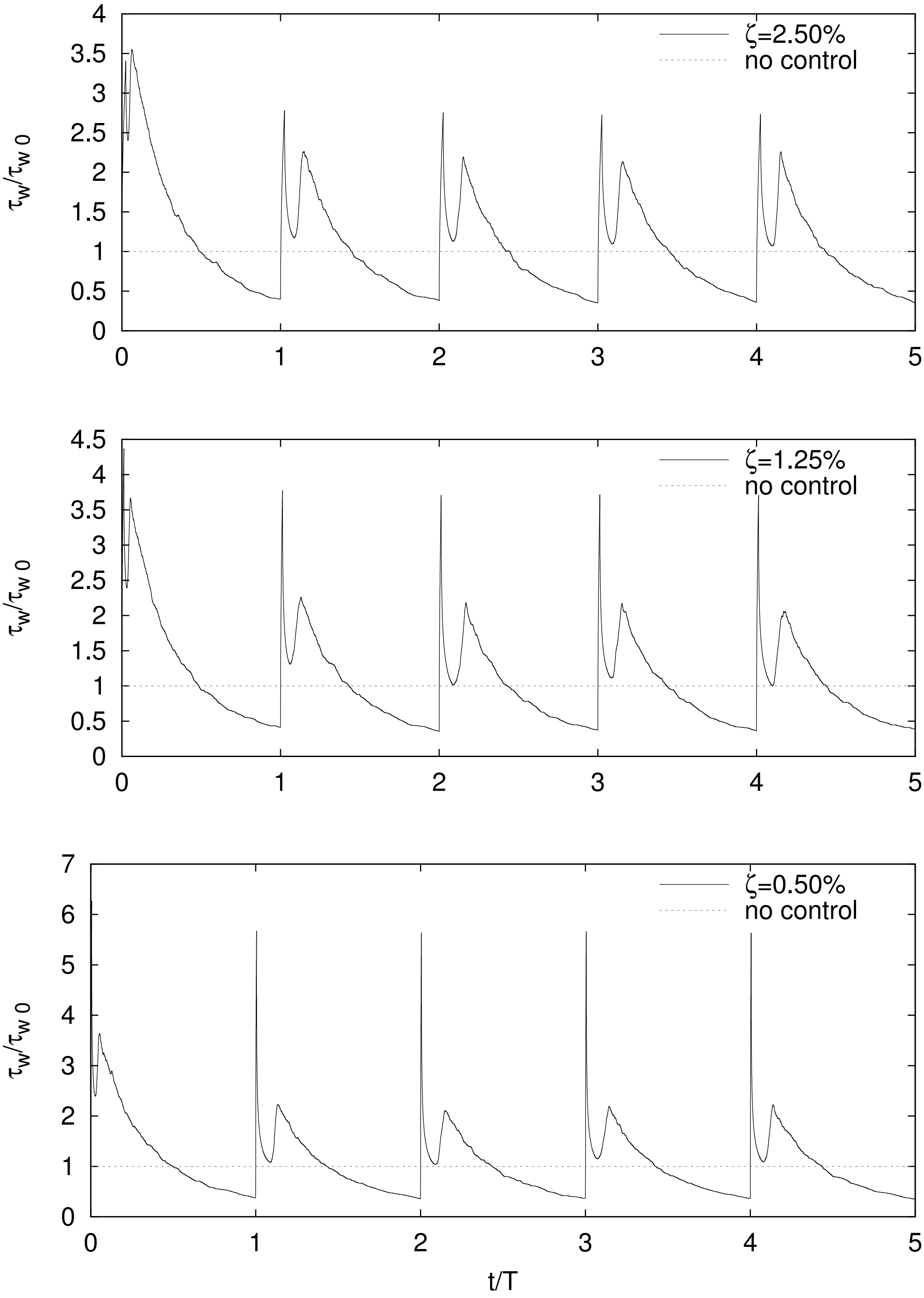

Figure A.10: Negative streamwise shear stress at $y = 2$, normalized with the uncontrolled field value $-\tau_{\mathrm{w}0}$ vs time normalized with the forcing period T. This figure shows its trend stress during time history for each couple of parameters (ζ,$T^{+} = 3600$).

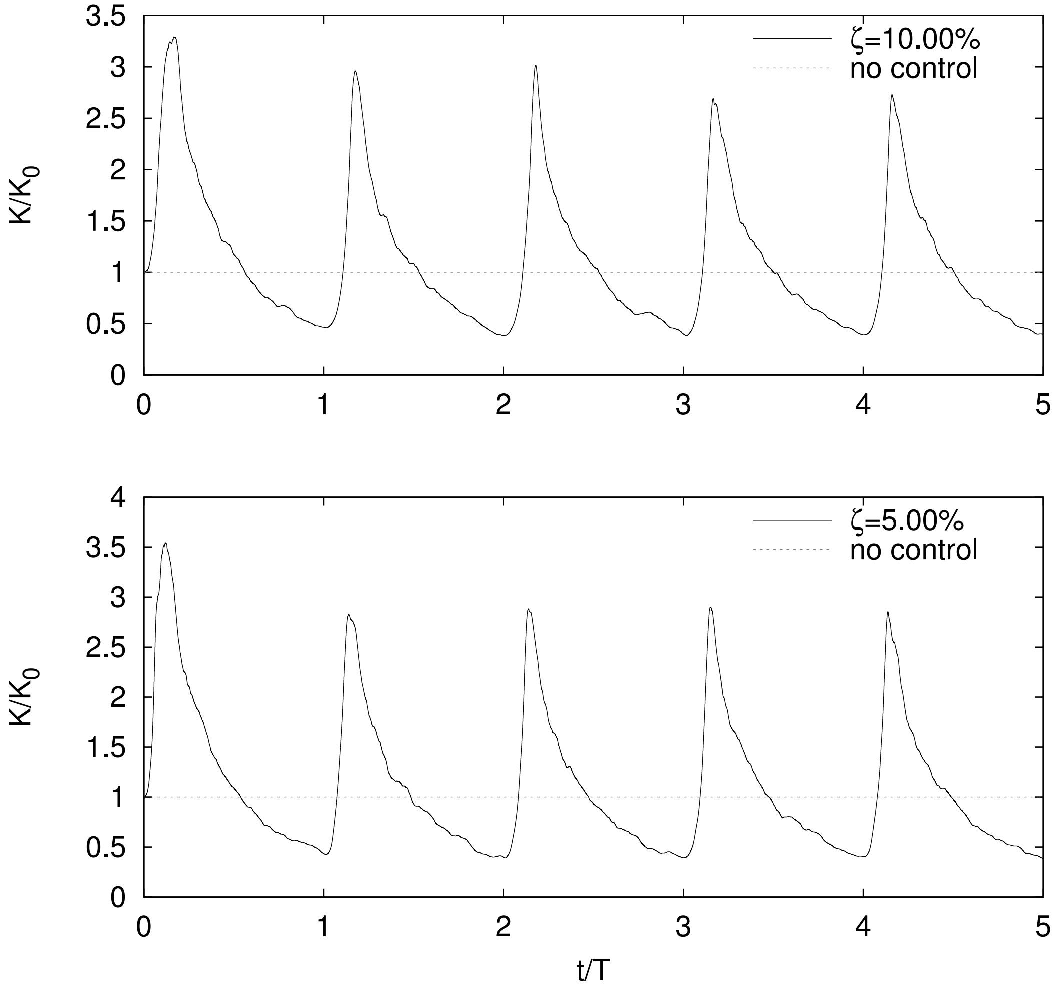

Figure A.11: Turbulent kinetic energy per unit mass integrated over the wall-normal direction $K = \int_0^2 k \, \mathrm{d}y$, normalized with the uncontrolled field value K_0 vs time normalized with the forcing period T. This figure shows its trend during time history for each couple of parameters (ζ,$T^+ = 3600$).

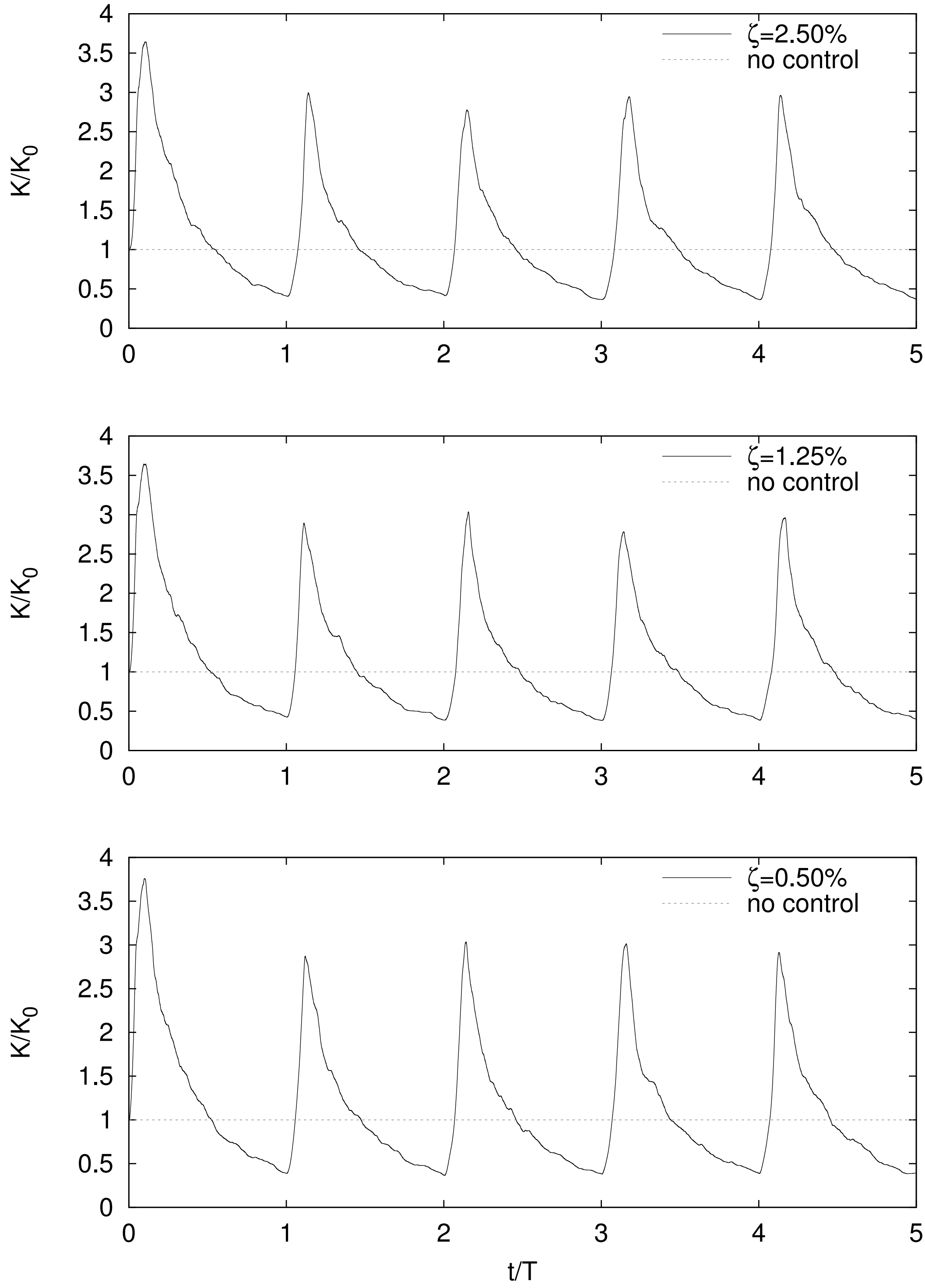

Figure A.12: Turbulent kinetic energy per unit mass integrated over the wall-normal direction $K = \int_0^2 k \, \mathrm{d}y$, normalized with the uncontrolled field value K_0 vs time normalized with the forcing period T. This figure shows its trend during time history for each couple of parameters (ζ,$T^+ = 3600$).

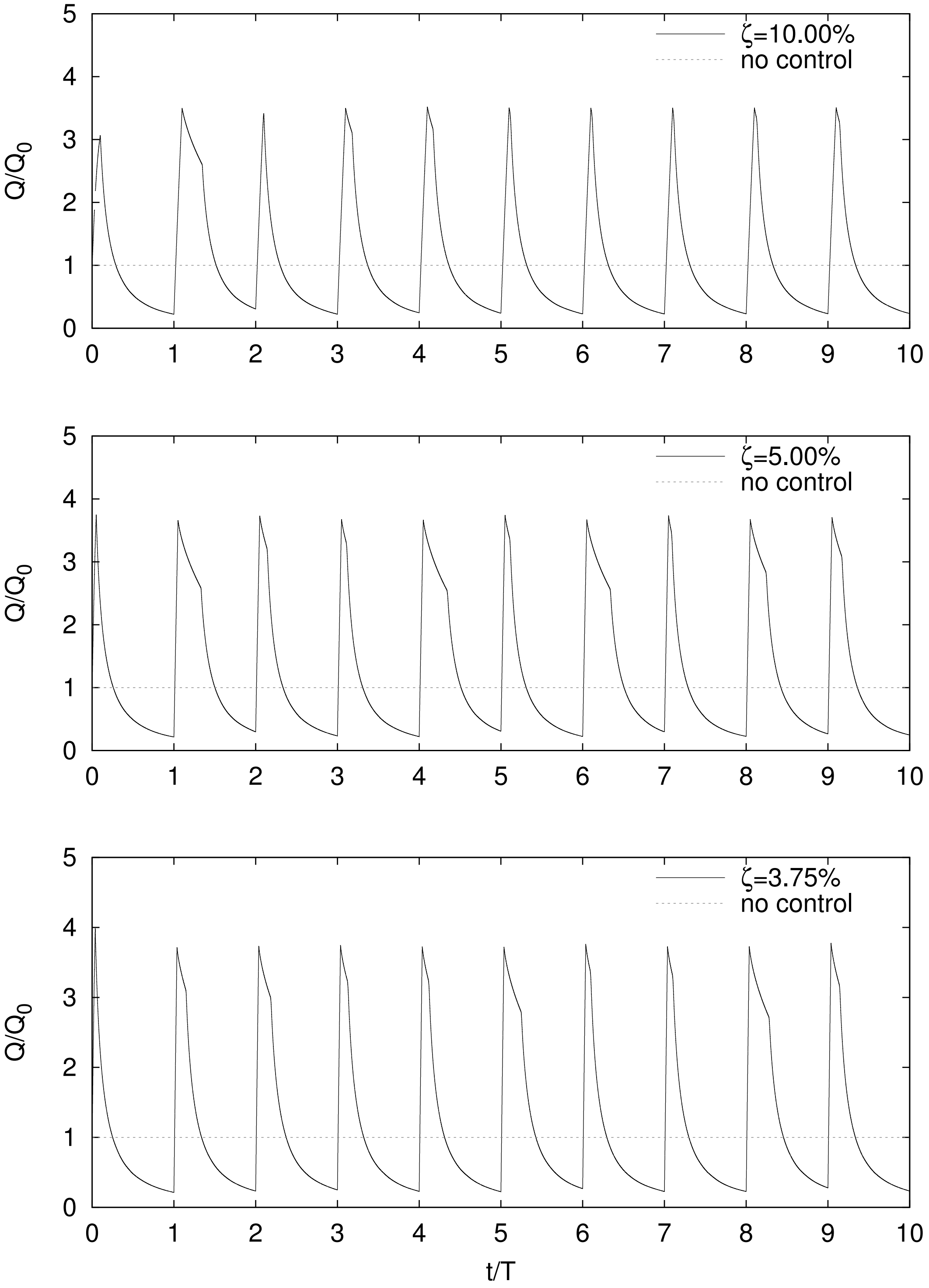

Figure A.13: Flow rate normalized with the uncontrolled field value Q_0 vs time normalized with the forcing period T. This figure shows its trend during time history for each couple of parameters (ζ,$T^+ = 10800$).

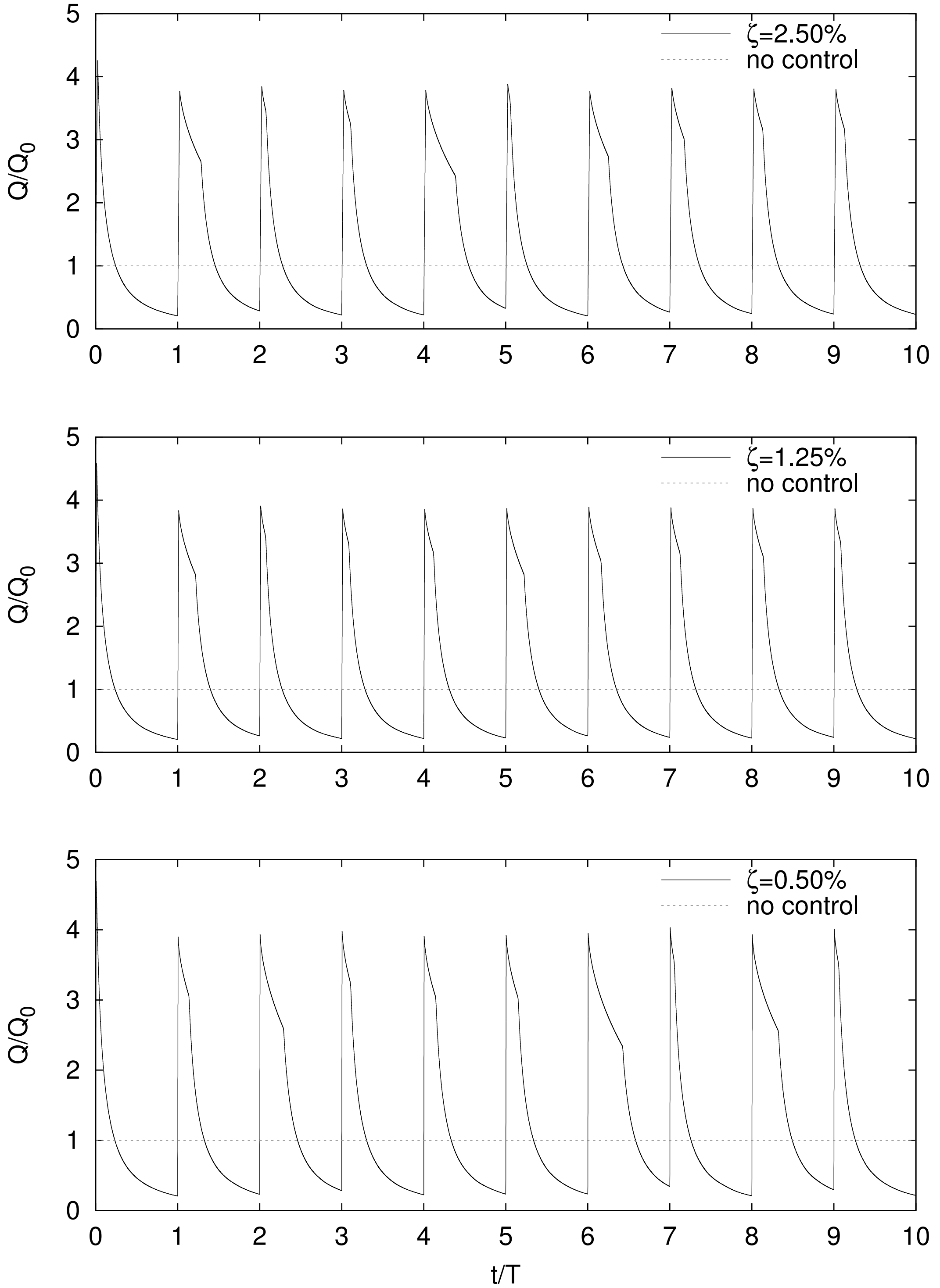

Figure A.14: Flow rate normalized with the uncontrolled field value Q_0 vs time normalized with the forcing period T. This figure shows its trend during time history for each couple of parameters (ζ,$T^+ = 10800$).

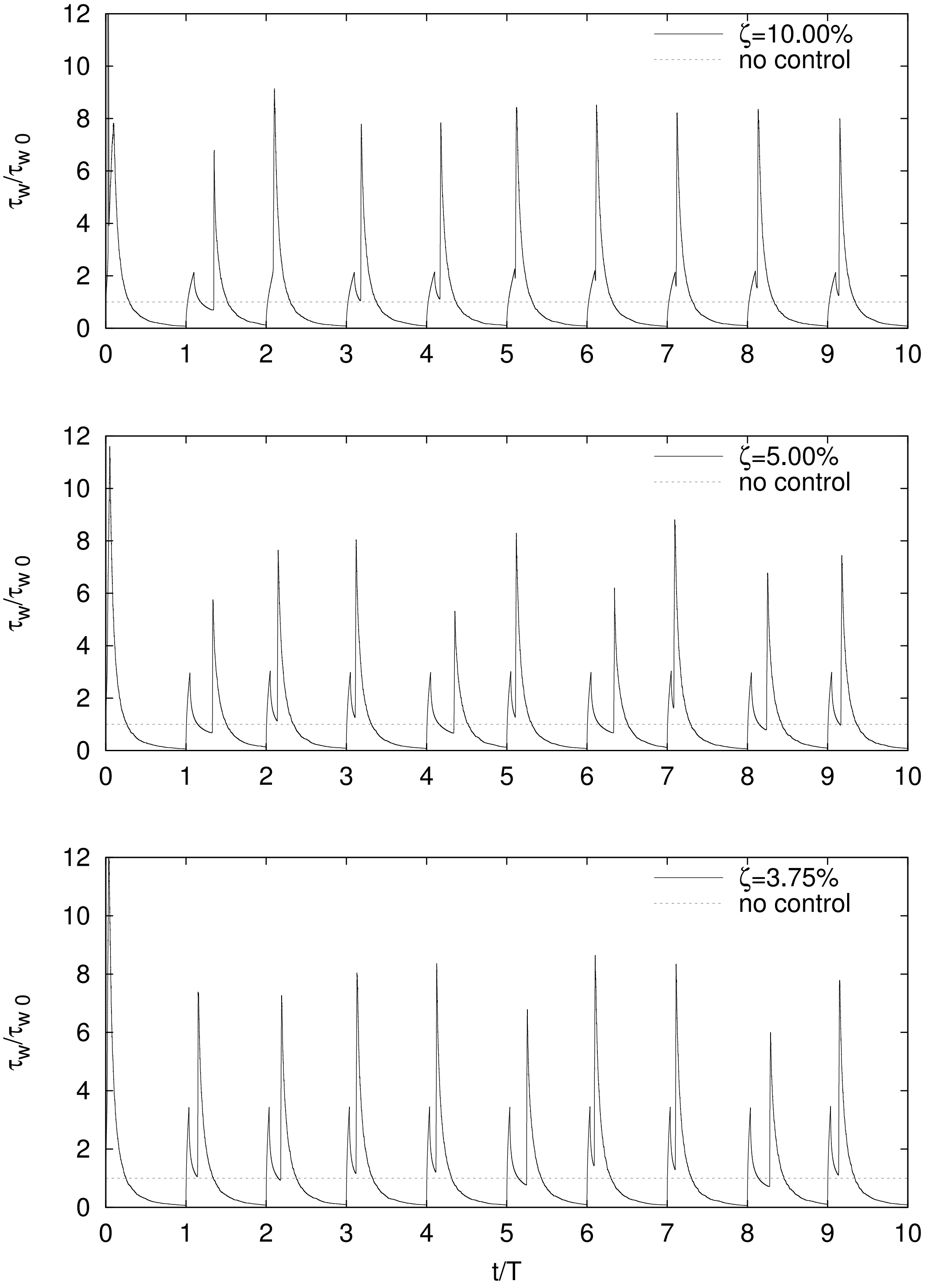

Figure A.15: Streamwise shear stress at $y = 0$, normalized with the uncontrolled field value τ_{w0} vs time normalized with the forcing period T. This figure shows its trend during time history for each couple of parameters (ζ,$T^+ = 10800$).

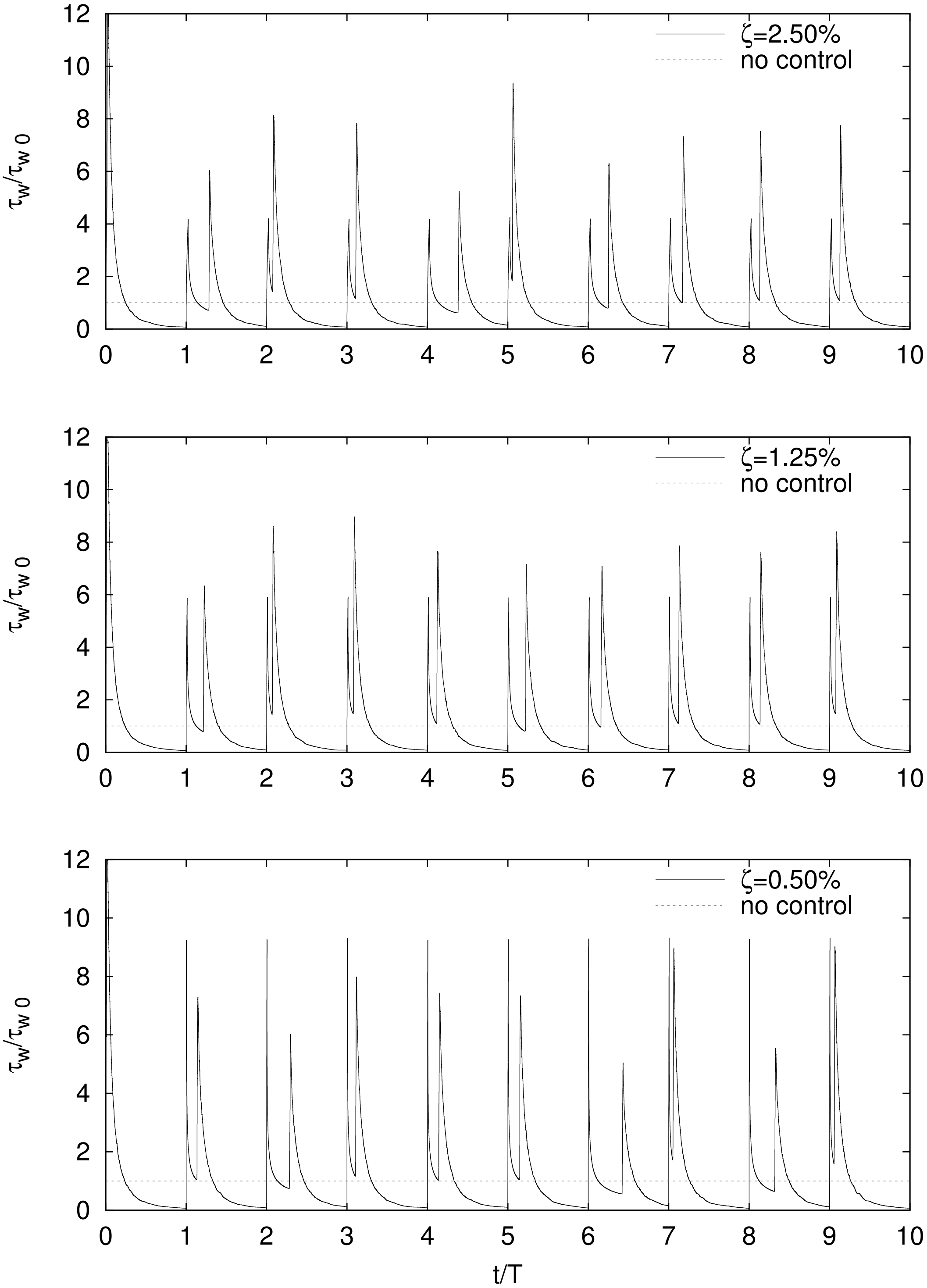

Figure A.16: Streamwise shear stress at $y = 0$, normalized with the uncontrolled field value $\tau_{\mathrm{w}0}$ vs time normalized with the forcing period T. This figure shows its trend during time history for each couple of parameters (ζ,$T^+ = 10800$).

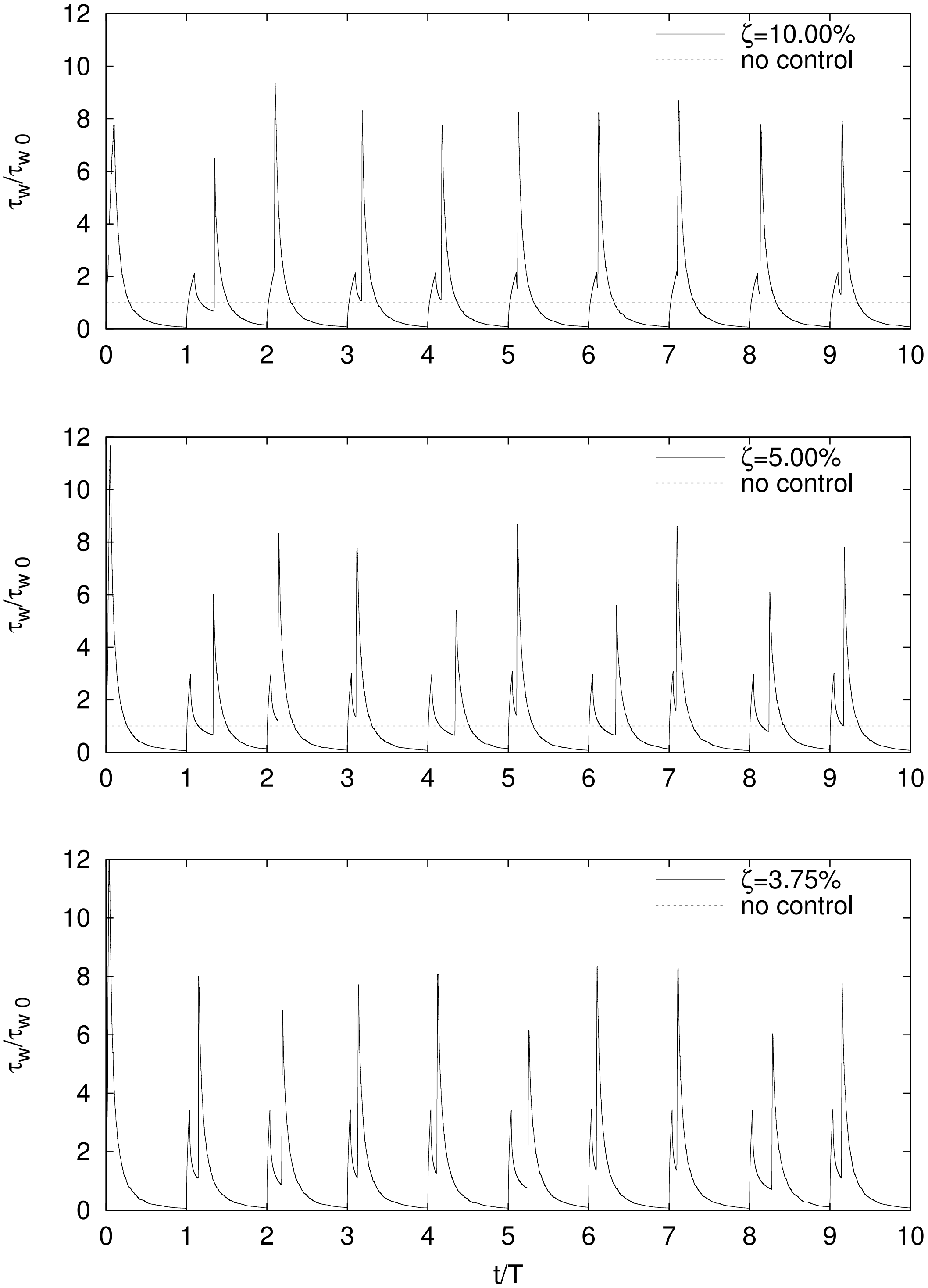

Figure A.17: Negative streamwise shear stress at $y = 2$, normalized with the uncontrolled field value $-\tau_{w0}$ vs time normalized with the forcing period T. This figure shows its trend during time history for each couple of parameters (ζ,$T^+ = 10800$).

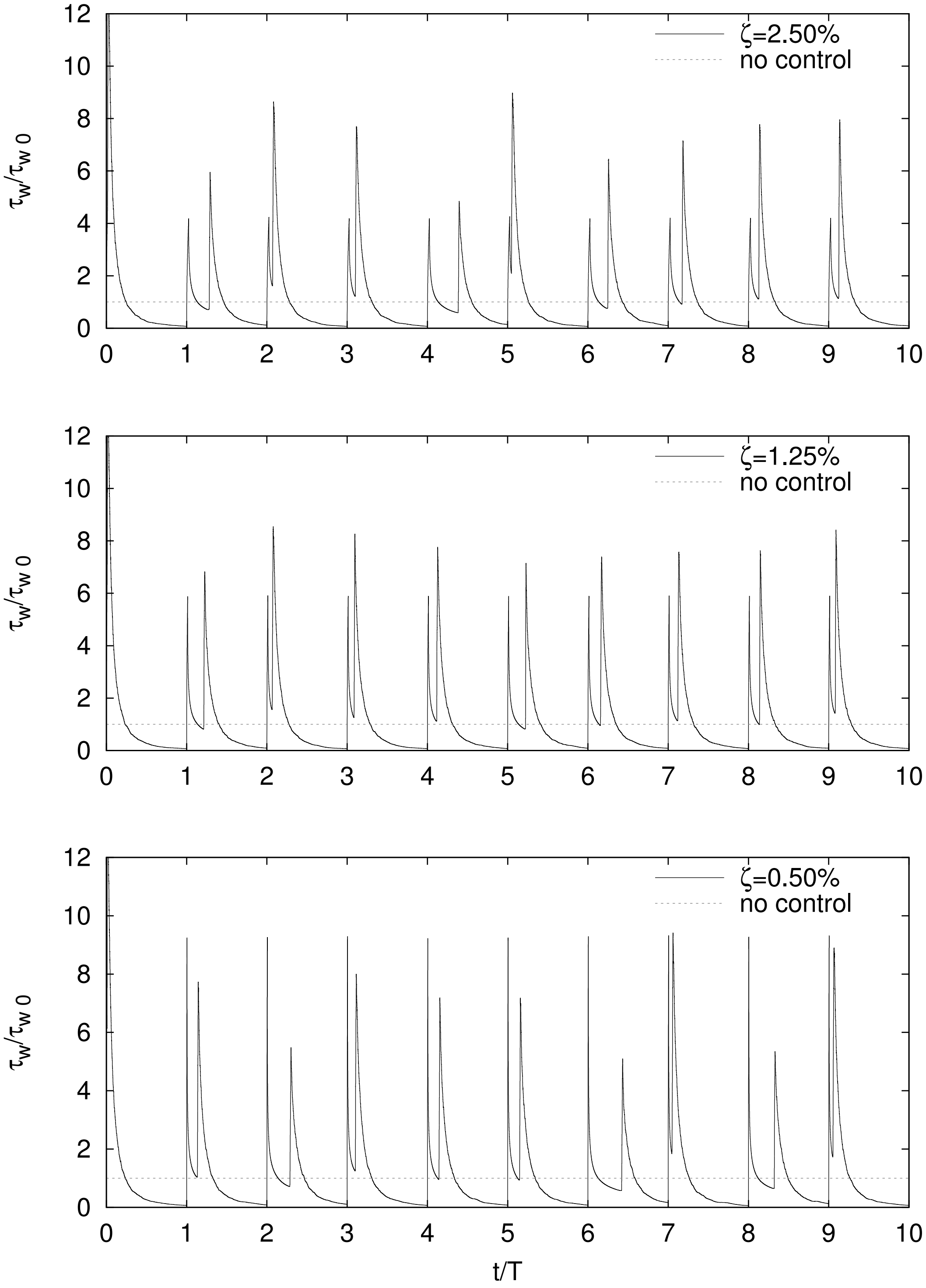

Figure A.18: Negative streamwise shear stress at $y = 2$, normalized with the uncontrolled field value $-\tau_{\mathrm{w}0}$ vs time normalized with the forcing period T. This figure shows its trend during time history for each couple of parameters (ζ,$T^{+} = 10800$).

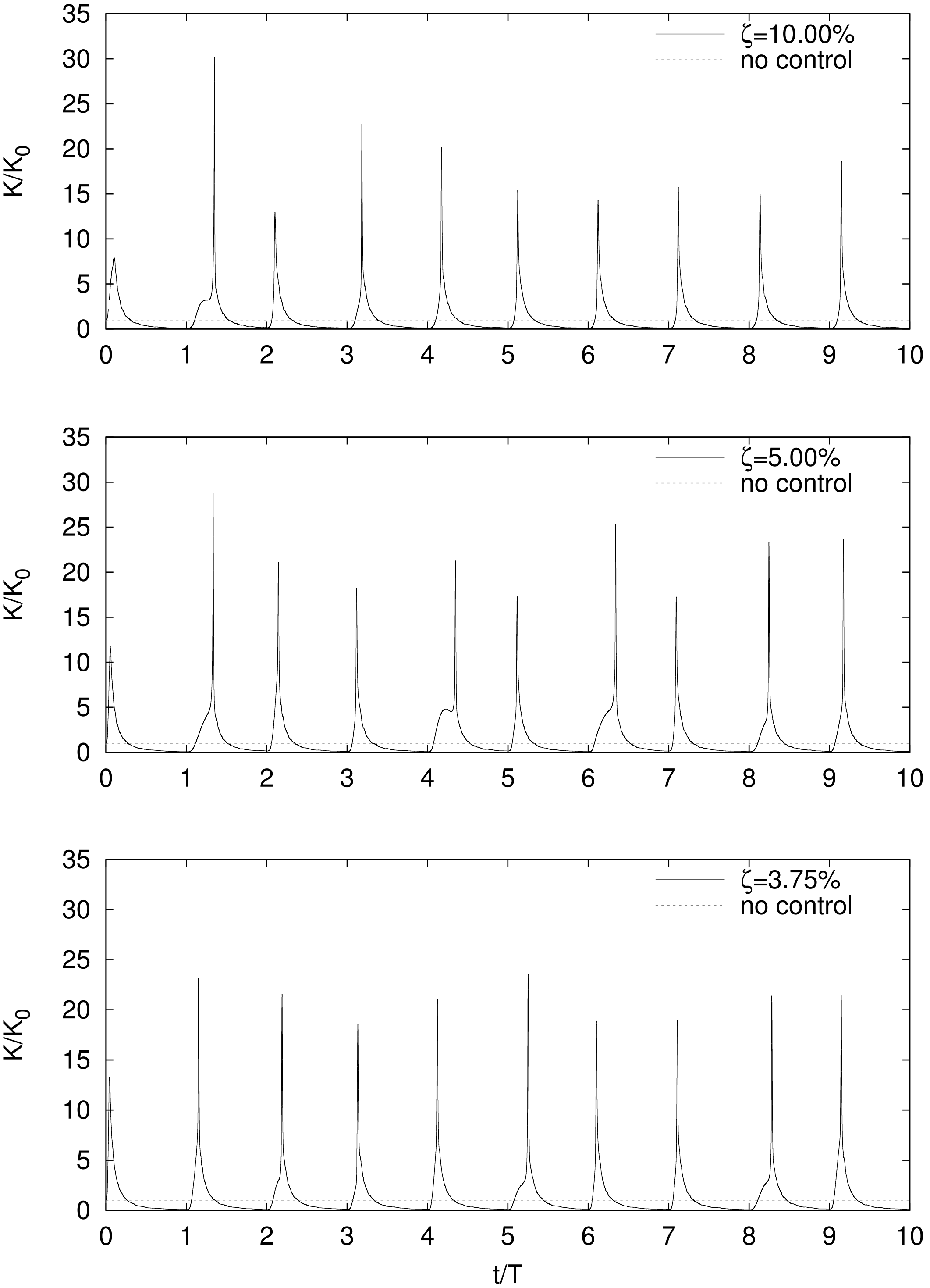

Figure A.19: Turbulent kinetic energy per unit mass integrated over the wall-normal direction $K = \int_0^2 k \, \mathrm{d}y$, normalized with the uncontrolled field value K_0 vs time normalized with the forcing period T. This figure shows its trend during time history for each couple of parameters (ζ,$T^+ = 10800$).

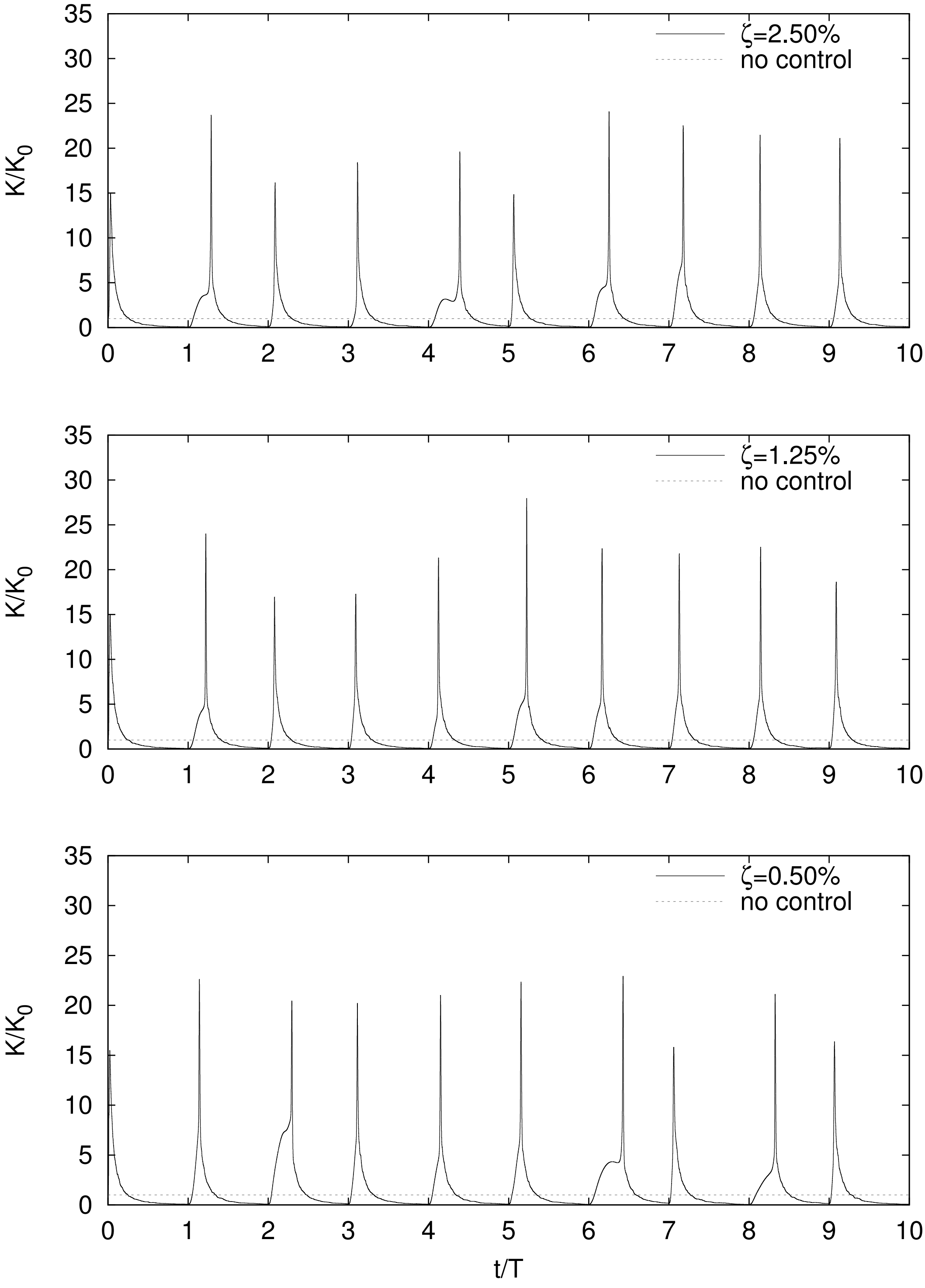

Figure A.20: Turbulent kinetic energy per unit mass integrated over the wall-normal direction $K = \int_0^2 k \, \mathrm{d}y$, normalized with the uncontrolled field value K_0 vs time normalized with the forcing period T. This figure shows its trend during time history for each couple of parameters (ζ,$T^+ = 10800$).

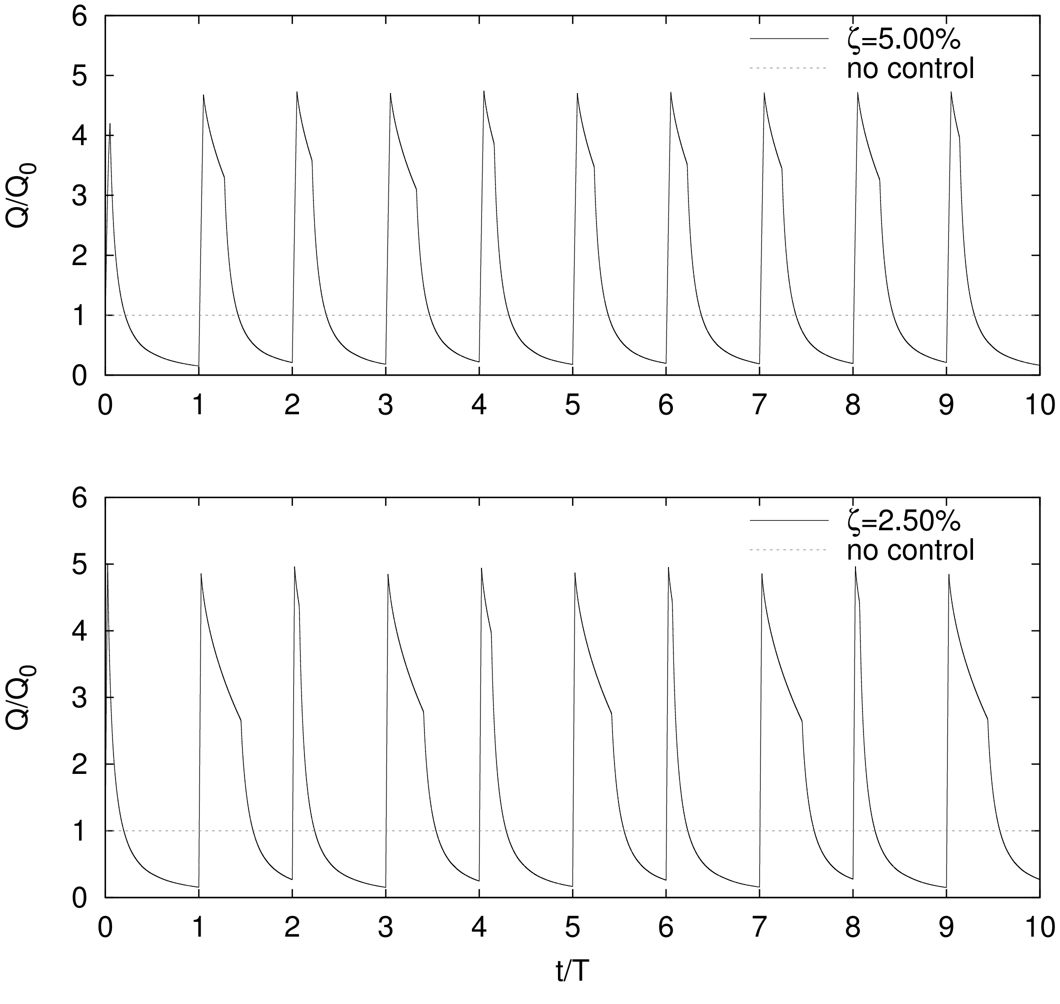

Figure A.21: Flow rate normalized with the uncontrolled field value Q_0 vs time normalized with the forcing period T. This figure shows its trend during time history for each couple of parameters (ζ,$T^+ = 14400$).

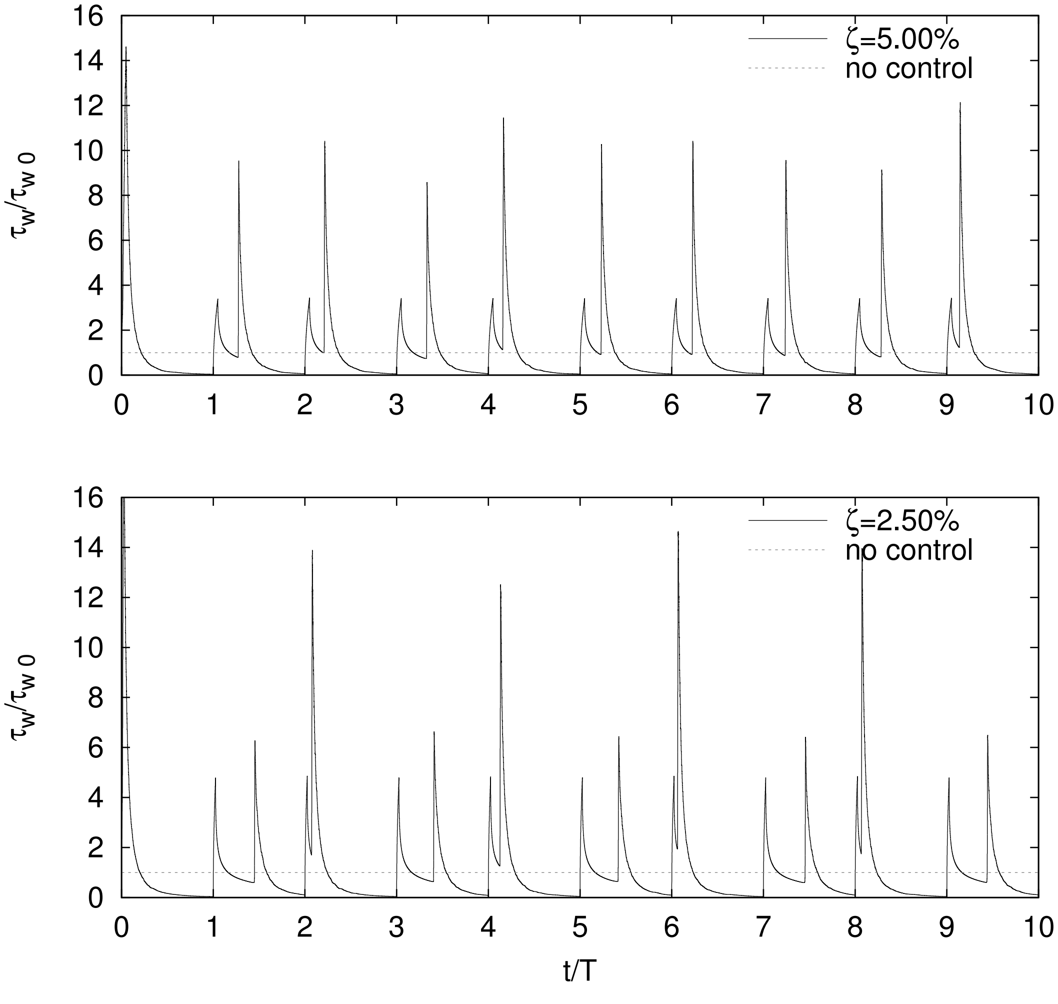

Figure A.22: Streamwise shear stress at $y = 0$, normalized with the uncontrolled field value $\tau_{\mathrm{w}0}$ vs time normalized with the forcing period T. This figure shows its trend during time history for each couple of parameters (ζ,$T^+ = 14400$).

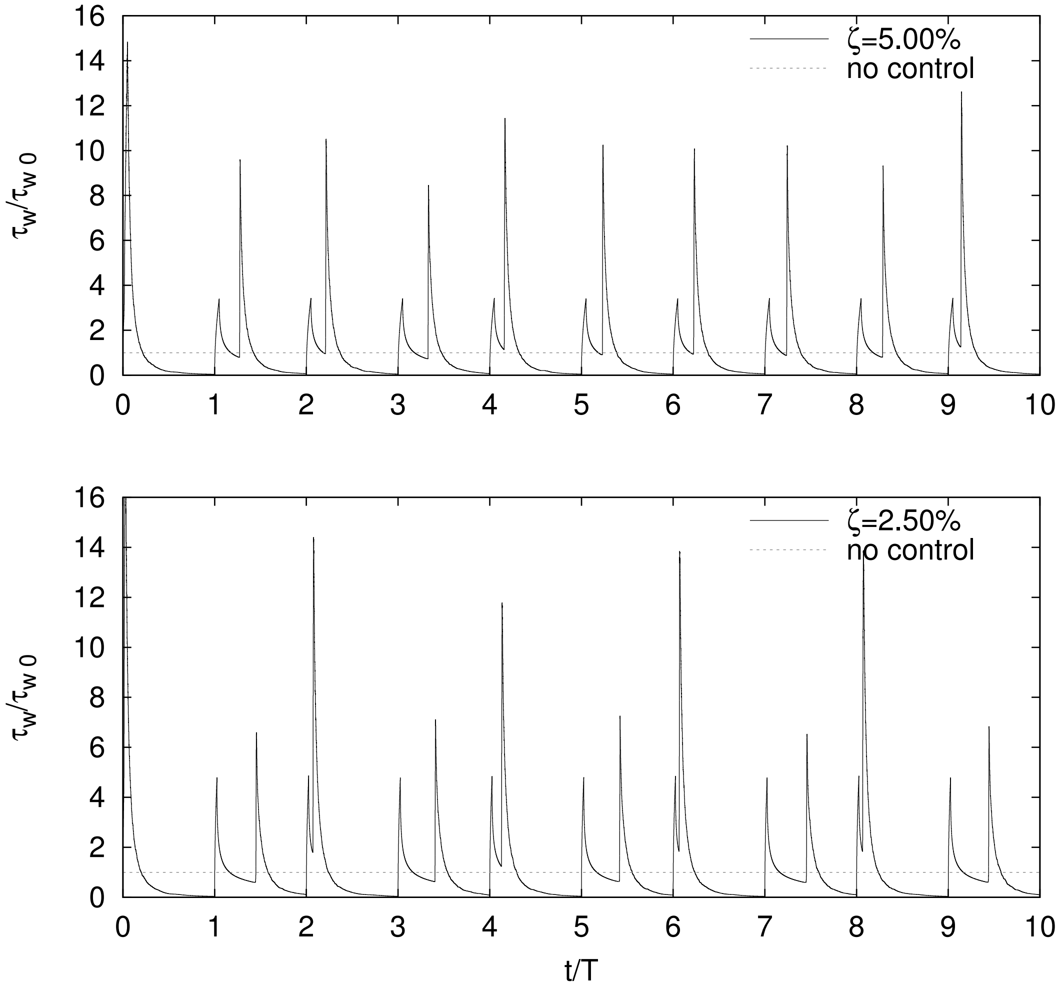

Figure A.23: Negative streamwise shear stress at $y = 2$, normalized with the uncontrolled field value $-\tau_{\mathrm{w}0}$ vs time normalized with the forcing period T. This figure shows its trend during time history for each couple of parameters (ζ,$T^+ = 14400$).

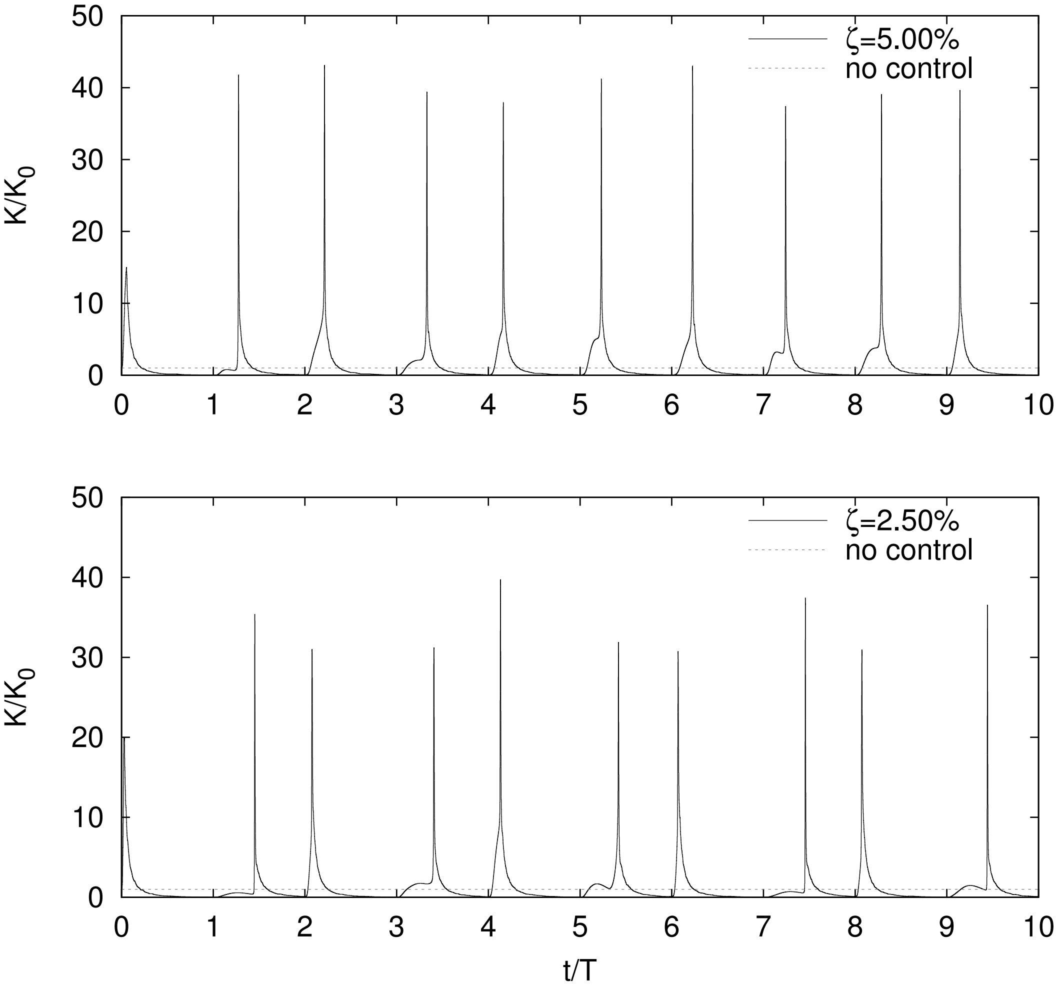

Figure A.24: Turbulent kinetic energy per unit mass integrated over the wall-normal direction $K = \int_0^2 k \, \mathrm{d}y$, normalized with the uncontrolled field value K_0 vs time normalized with the forcing period T. This figure shows its trend during time history for each couple of parameters (ζ,$T^+ = 14400$).

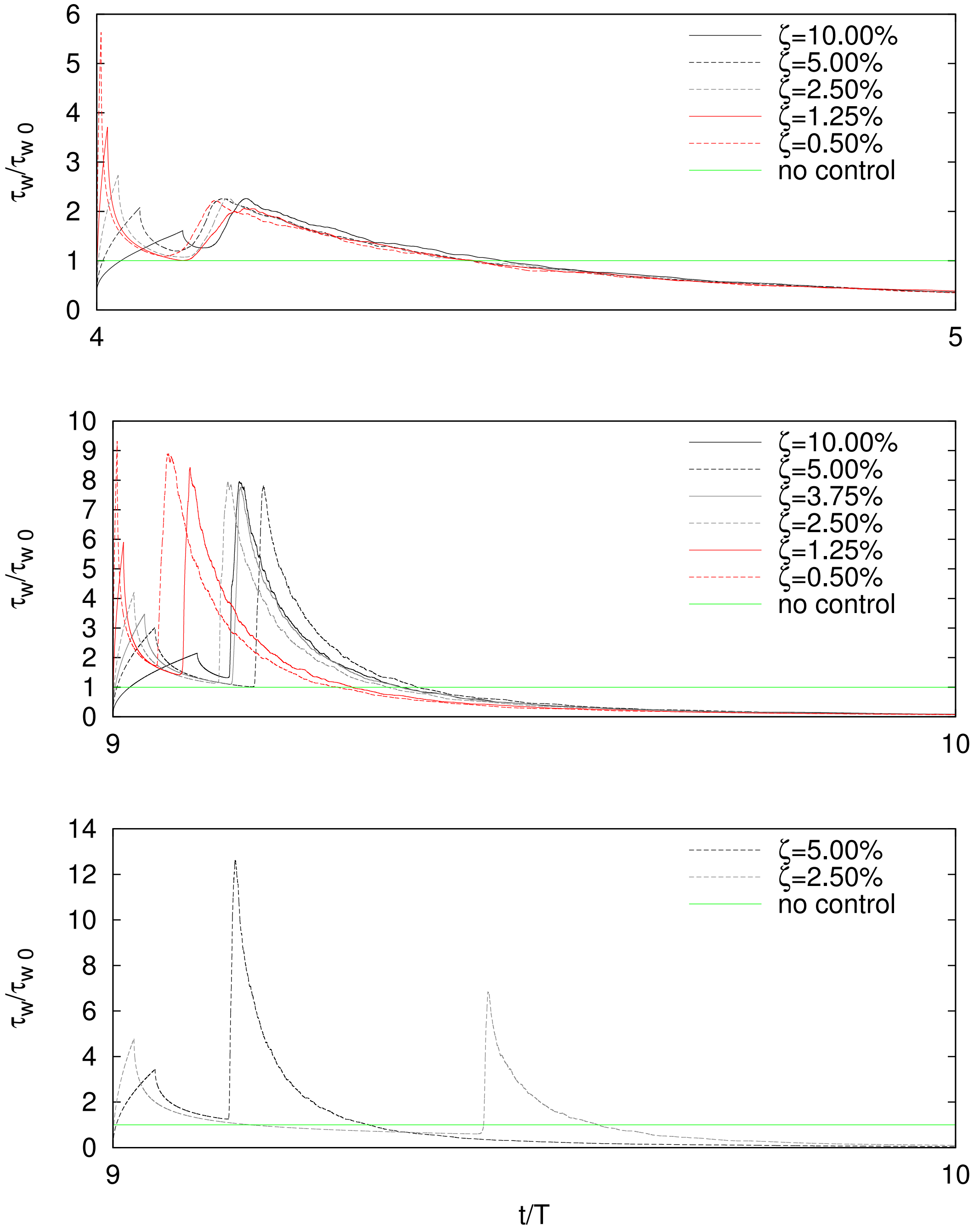

Figure A.25: Negative streamwise shear stress τ_{w} at $y = 2$, normalized with the uncontrolled field value $-\tau_{\mathrm{w}0}$ vs time normalized with the forcing period T. This figure shows a comparison (for one chosen cycle) of the effect of the duty-cycle ζ for each forcing period. Top: $T^+ = 3600$ during the V cycle. Middle: $T^+ = 10800$ during the X cycle. Bottom: $T^+ = 14400$ during the X cycle.

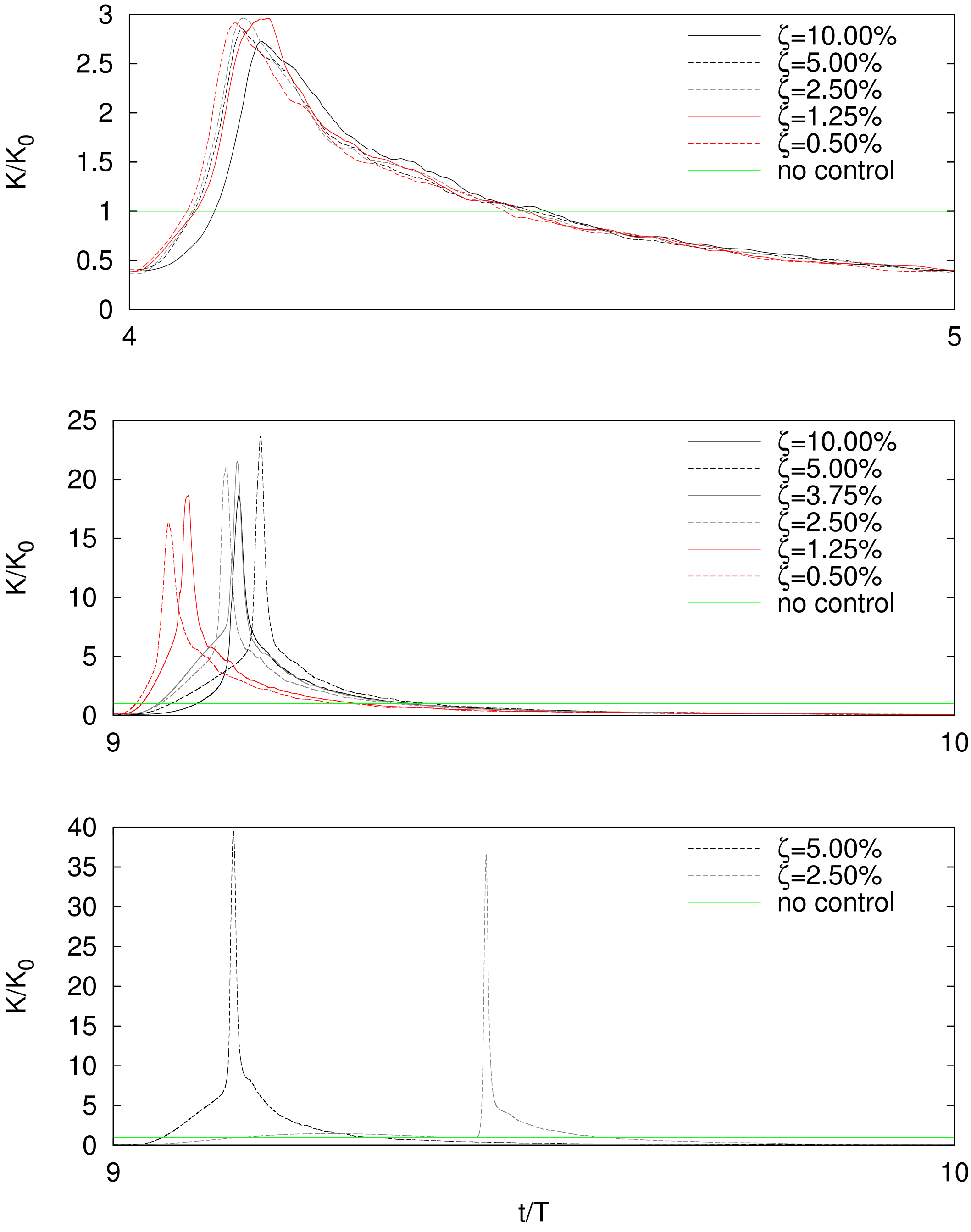

Figure A.26: Turbulent kinetic energy per unit mass integrated over wall-normal direction $K = \int_0^2 k \, \mathrm{d}y$, normalized with the uncontrolled field value K_0 vs time normalized with the forcing period T. This figure shows a comparison (for one chosen cycle) of the effect of the duty-cycle ζ for each forcing period. Top: $T^+ = 3600$ during the V cycle. Middle: $T^+ = 10800$ during the X cycle. Bottom: $T^+ = 14400$ during the X cycle.

Appendix B

Manipulation of the velocity profile

In this Appendix we briefly report some results obtained in a preliminary phase of the work, where, inspired from the Song's work in his PhD thesis [51], we have manipulated the mean velocity profile in an incompressible turbulent channel flow to suppress the turbulence self-sustain mechanism and eventually to *relaminarise* the turbulent flow. It has been done by introducing a body force in addition to the pressure gradient as flow driving forcing. This strategy can be considered as a spatial dual to the temporal technique just presented in this work; in fact both act not only on the flow inner layer, but also in the outer one, completely modifying the morphology of mean velocity profile.

In the following a brief description of problem and of numerical code used will be given. Then some results will be shown with final considerations about this technique.

B.1 Model problem

The channel flow is the same just presented in section 3.1. Here a streamwise y-dependent $\mathbf{F} = F(y)\hat{\mathbf{x}}$, where $\hat{\mathbf{x}}$ is the versor in streamwise direction, is added to the flow (see figure 3.1 for the axis' convention). So the dimensionless Navier-Stokes equations become:

$$\begin{cases} \dfrac{\partial \mathbf{u}}{\partial t} + (\mathbf{u} \cdot \boldsymbol{\nabla})\mathbf{u} = -\boldsymbol{\nabla} p + \dfrac{1}{Re}\Delta \mathbf{u} + \mathbf{F}, \\ \boldsymbol{\nabla} \cdot \mathbf{u} = 0. \end{cases} \tag{B.1}$$

with no slip boundary condition at wall.

At first, starting from a fully turbulent channel flow, a target velocity is freely chosen. Once target velocity profile $\mathbf{U}_\gamma = U_\gamma \hat{\mathbf{x}}$ is completely determined, the desired body force $\mathbf{F}$ is easily obtained by substituting $\mathbf{U}_\gamma$ in Eqs. (B.1). Here a family of profiles parametrized with a parameter γ is chosen as

$$U_\gamma = (1-\gamma)U_{lam} + \gamma U_{turb}, \tag{B.2}$$

with $0 \leq \gamma \leq 1$, so that for $\gamma = 0$ the target profile coincides with the parabolic velocity profile U_{lam} (laminar flow) and for $\gamma = 1$ it coincides with the fully turbulent mean velocity profile U_{turb}, as shown in figure B.1.

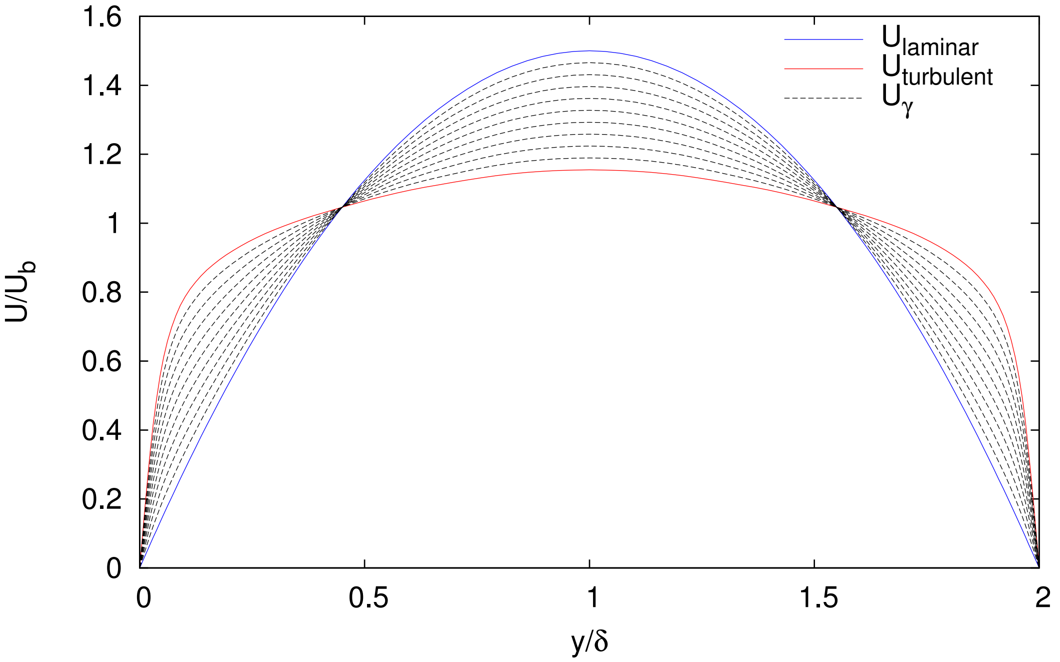

Figure B.1: Target velocity profile U_γ normalized with U_b vs wall-normal coordinate.

The mean velocity profile imposed represents the new laminar solution to Navier-Stokes equations (B.1). The body force acts on turbulent flow field deforming its mean velocity profile so that this tends to the target one. During this work a simulation, with the calculated body force implemented and with a parabolic profile as initial condition, has been run to verify if parabola tends to the target velocity profile.

B.2 Numerical method

DNS code used for these simulations is the same just described in Chapter 3. Simulations run with constant flow rate condition (CFR): streamwise flow rate per unit length Q is imposed , so that the bulk velocity U_b is fixed. In this way the Reynolds number Re_b based on U_b becomes the natural choice.

Unless otherwise indicated, in this appendix in all velocity/speed will be normalized with U_b, length with the half channel height δ, time with δ/U_b, pressure gradient with $\rho {U_b}^2/\delta$ and kinetic energy per unit mass with ${U_b}^2$.

Streamwise flow rate is imposed equal to 2, so that U_b is equal to unit. The initial field is a fully turbulent channel flow at $Re_b = 4000$. So, the simulations have been run at the same Reynolds number of the initial field. The computational domain has streamwise length of $L_x = 5\pi$, wall-normal height of $L_y = 2$ and spanwise width of $L_z = 2\pi$. The domain has been discretized with a Fourier expansion of 144×144 modes for the streamwise and spanwise directions, and 100 points in the wall-normal direction. In the present code, the stretching function used to generate the mesh in y-direction is again

$$y = \frac{\tanh a\overline{y}}{a}, \tag{B.3}$$

where a is an adjustable parameter used to modify the mesh deformation (here imposed equal to $a = 1.6$) and $\overline{y}$ is a mesh grid with constant spacing coming from lower to upper wall.

B.3 Results

In this section some results about this control technique will be reported. The target profile chosen for the simulation corresponds to the parameter $\gamma = 0.8$. The body force is turned on at time $t = 100$.

Figure B.2 shows that streamwise pressure gradient suddenly falls down when the body force acts on flow. It has to remember that for simulations run with CFR condition, decrease of (negative) streamwise pressure gradient is strictly linked to positive drag reduction rate. In this case the control technique is of active open-loop type, so that a control energy (Eq (1.12)) has to be considered to evaluate net drag reduction and, hence, energy saving rate.

Figure B.3 shows trend of turbulent kinetic energy integrated over wall-normal direction. This shows that when body force is turned on, turbulent kinetic energy falls down to a lower level. However the flow remains in the turbulent state. Song in his PhD thesis [51] has implemented a similar control for a turbulent pipe flow at $Re_b = 2000$. He observed that turbulence may either completely decay (*relaminarisation* of the turbulent flow) or survive at a lower kinetic energy level after the initial decrease in its intensity when body force is turned on, depending on the specific initial conditions.

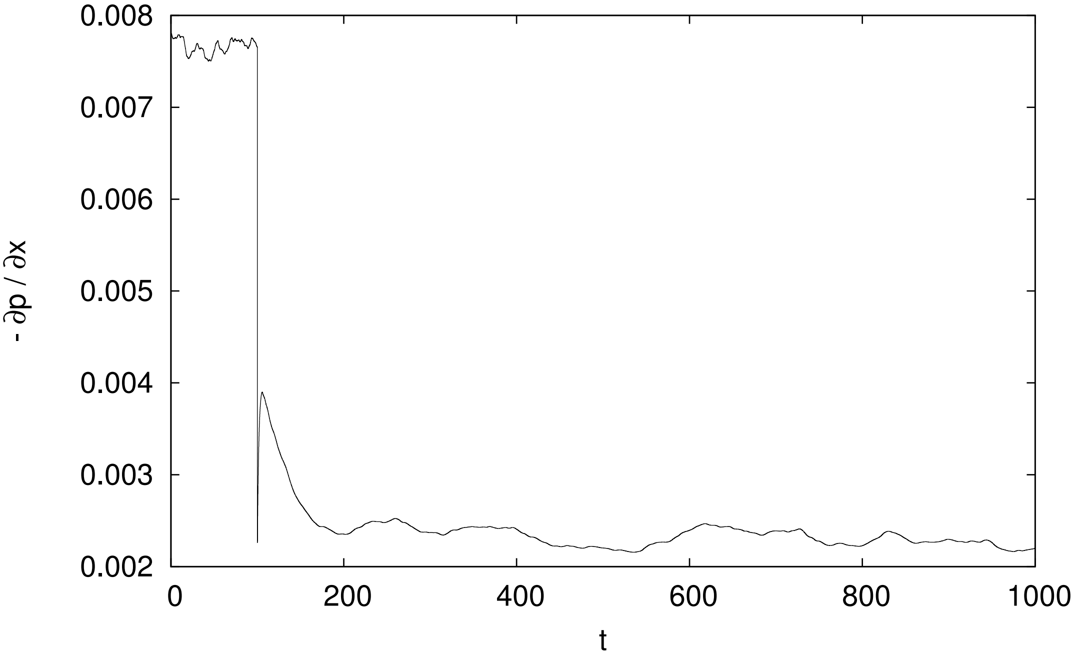

Figure B.2: The effect on the negative streamwise pressure gradient of the body force turning on.

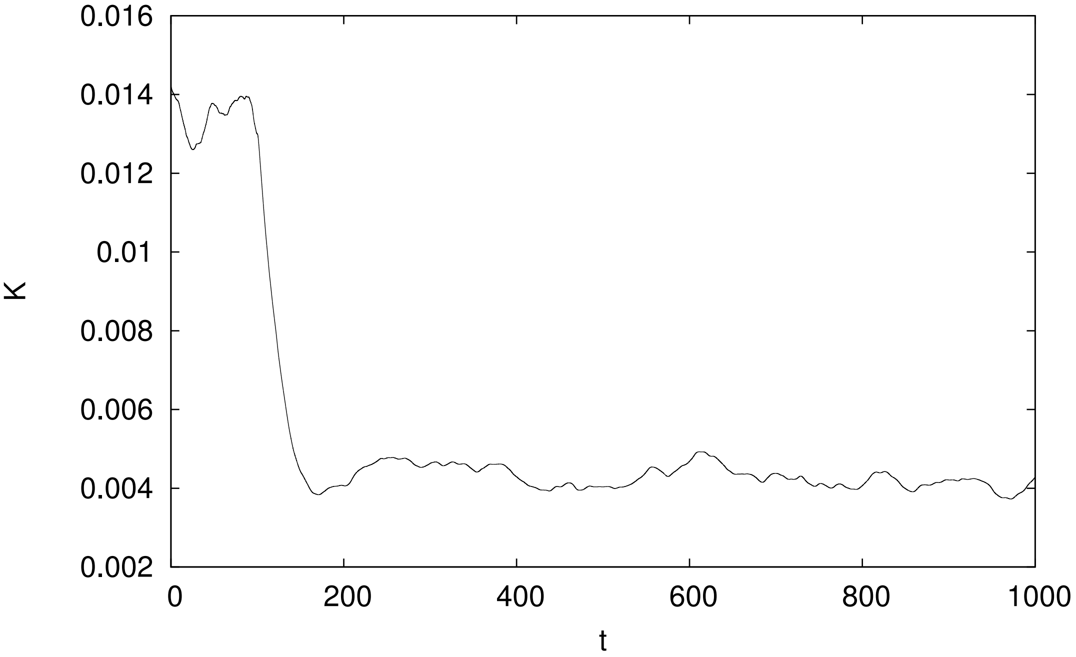

Figure B.3: The effect on the turbulent kinetic energy per unit mass, integrated over the wall-normal direction $K = \int_0^2 k \, \mathrm{d}y$, of the body force turning on.

Bibliography

[1] C. Ariyaratne, S. He, and A.E. Vardy. Wall friction and turbulence dynamics in decelerating pipe flows. *Journal of Hydraulic Research*, 48(6):810–821, 2010.

[2] N.S. Berman and W.K. George. Time scale and molecular weight distribution contributions to dilute polymer solution fluid mechanics. Technical report, Defense Technical Information Center, 1974.

[3] T.R. Bewley. A fundamental limit on the balance of power in a transpiration-controlled channel flow. *J. Fluid Mech.*, 632:443–446, 2009.

[4] K. Bhaganagar. Direct numerical simulation of unsteady flow in channel with rough walls. *Phys. Fluids*, 20(10):101508, 2008.

[5] H. Choi, P. Moin, and J. Kim. Active turbulence control for drag reduction in wall-bounded flows. *J. Fluid Mech.*, 262:75–110, 1994.

[6] Y.M. Chung. Unsteady turbulent flow with sudden pressure gradient changes. *International journal for numerical methods in fluids*, 47(8-9):925–930, 2005.

[7] J.H.M. Fransson, A. Talamelli, L. Brandt, and C. Cossu. Delaying transition to turbulence by a passive mechanism. *Physical review letters*, 96(6):064501, 2006.

[8] B. Frohnapfel, Y. Hasegawa, and M. Quadrio. Money versus time: evaluation of flow control in terms of energy consumption and convenience. *J. Fluid Mech.*, 700:406–418, 2012.

[9] K. Fukagata, K. Iwamoto, and N. Kasagi. Contribution of Reynolds stress distribution to the skin friction in wall-bounded flows. *Phys. Fluids*, 14(11): L73–L76, 2002.

[10] K. Fukagata, K. Sugiyama, and N. Kasagi. On the lower bound of net driving power in controlled duct flows. *Physica D*, 238:1082–1086, 2009.

[11] M. Gad-el Hak. *Flow Control – Passive, Active and Reactive Flow Management.* Cambridge University Press, Cambridge, 2000.

[12] D.A. Gilbrech and G.D. Coombs. Critical reynolds numbers for incompressible pulsating flow in tubes. *Developments in Theoretical and Applied Mechanics*, 1:292–304, 1963.

[13] J. Gray. Studies in animal locomotion vi. the propulsive powers of the dolphin. *J. Exp. Biol.*, 13(2):192–199, 1936.

[14] P. Hall. The stability of poiseuille flow modulated at high frequencies. In *Proceedings of the Royal Society of London A: Mathematical, Physical and Engineering Sciences*, volume 344, pages 453–464, 1975.

[15] Y. Hasegawa, M. Quadrio, and B. Frohnapfel. Numerical simulation of turbulent duct flows with constant power input. *J. Fluid Mech.*, 750:191–209, 2014.

[16] S. He and J.D. Jackson. An experimental study of pulsating turbulent flow in a pipe. *European Journal of Mechanics-B/Fluids*, 28(2):309–320, 2009.

[17] S. He and M. Seddighi. Turbulence in transient channel flow. *J. Fluid Mech.*, 715:60–102, 2013.

[18] S. He, C. Ariyaratne, and A.E. Vardy. Wall shear stress in accelerating turbulent pipe flow. *J. Fluid Mech.*, 685:440–460, 2011.

[19] K. Iwamoto, N. Sasou, and H. Kawamura. Direct numerical simulation of pulsating turbulent channel flow for drag reduction. In *Advances in Turbulence XI*, pages 709–711. Springer, 2007.

[20] K. Iwamoto, Y. Morino, and A. Murata. Direct numerical simulation for drag reduction by pulsating turbulent pipe flow. *Proc. of the Asian Symposium on Computational Heat Transfer and Fluid Flow*, 1:192–195, 2009.

[21] W.J. Jung, N. Mangiavacchi, and R. Akhavan. Suppression of turbulence in wall-bounded flows by high-frequency spanwise oscillations. *Phys. Fluids A*, 4 (8):1605–1607, 1992.

[22] N. Kasagi, Y. Suzuki, and K. Fukagata. MEMS-based feedback control of turbulence for drag reduction. *Annu. Rev. Fluid Mech.*, 41:231–251, 2009.

[23] J. Kim and J. Lim. A linear process in wall-bounded turbulent flows. *Phys. Fluids*, 12(8):1885–1888, 2000.

[24] B.E. Launder. Laminarization of the turbulent boundary layer in a severe acceleration. *J. Appl. Mech.*, 31(4):707–708, 1964.

[25] C. Lee, J. Kim, and H. Choi. Suboptimal control of turbulent channel flow for drag reduction. *J. Fluid Mech.*, 358:245–258, 1998.

[26] T. Lee, M. Fisher, and W.H. Schwarz. Investigation of the effects of a compliant surface on boundary-layer stability. *J. Fluid Mech.*, 288:37–58, 1995.

[27] C.R. Lodahl, B.M. Sumer, and J. Fredsøe. Turbulent combined oscillatory flow and current in a pipe. *J. Fluid Mech.*, 373:313–348, 1998.

[28] P. Luchini. Viscous sublayer analysis of riblets and wire arrays. *Appl. Sci. Res.*, 50:255–266, 1993.

[29] P. Luchini and M. Quadrio. A low-cost parallel implementation of direct numerical simulation of wall turbulence. *Journal of Computational Physics*, 211(2):551–571, 2006.

[30] H. Luo and T.R. Bewley. Accurate simulation of near-wall turbulence over a compliant tensegrity fabric. In *SPIE Paper 5757-17.*, 2005.

[31] M. Manna and A. Vacca. Resistance reduction in pulsatile turbulent pipe flow. *ASME J. Eng. Turb. Pow.*, 127:410–417, 2005.

[32] M. Manna, A. Vacca, and R. Verzicco. Pulsating pipe flow with large amplitude oscillations in the very high frequency regime. part 1. time-averaged analysis. *J. Fluid Mech.*, 700:246–282, 2012.

[33] Z.X. Mao and T.J. Hanratty. Studies of the wall shear stress in a turbulent pulsating pipe flow. *J. Fluid Mech.*, 170:545–564, 1986.

[34] Z.X. Mao and T.J. Hanratty. Influence of large-amplitude oscillations on turbulent drag. *AIChE journal*, 40(10):1601–1610, 1994.

[35] T. Mizushina, T. Maruyama, and Y. Shiozaki. Pulsating turbulent flow in a tube. *Journal of Chemical Engineering of Japan*, 6(6):487–494, 1974.

[36] R. Moser, J. Kim, and N.N. Mansour. Direct numerical simulation of turbulent channel flow up to $Re_\tau = 590$. *Phys. Fluids*, 11(4):943–945, 1999.

[37] S.B. Pope. *Turbulent Flows.* Cambridge Univ. Press, Cambridge, 2000.

[38] M. Quadrio and P. Luchini. A 4th order accurate, parallel numerical method for the direct simulation of turbulence in cartesian and cylindrical geometries. In *Proc. of the XV AIMETA Conf. on Theor. Appl. Mech*, 2001.

[39] M. Quadrio and P. Ricco. Critical assessment of turbulent drag reduction through spanwise wall oscillation. *J. Fluid Mech.*, 521:251–271, 2004.

[40] M. Quadrio, P. Ricco, and C. Viotti. Streamwise-traveling waves of spanwise wall velocity for turbulent drag reduction. *J. Fluid Mech.*, 627:161–178, 2009.

[41] B.R. Ramaprian and S.W. Tu. An experimental study of oscillatory pipe flow at transitional reynolds numbers. *J. Fluid Mech.*, 100(03):513–544, 1980.

[42] B.R. Ramaprian and S.W. Tu. Fully developed periodic turbulent pipe flow. part 2. the detailed structure of the flow. *J. Fluid Mech.*, 137:59–81, 1983.

[43] T. Sarpkaja. Experimental determination of the critical reynolds number for pulsating poiseuille flow. *Journal of Fluids Engineering*, 88(3):589–598, 1966.

[44] P.J. Schmid and D.S. Henningson. *Stability and transition in shear flows.* Springer Science & Business Media, 2001.

[45] A. Scotti and U. Piomelli. Numerical simulation of pulsating turbulent channel flow. *Phys. Fluids*, 13(5):1367–1384, 2001.

[46] M. Seddighi, S. He, P. Orlandi, and A.E. Vardy. A comparative study of turbulence in ramp-up and ramp-down unsteady flows. *Flow, turbulence and combustion*, 86(3-4):439–454, 2011.

[47] M. Seddighi, S. He, A.E. Vardy, and P. Orlandi. Direct numerical simulation of an accelerating channel flow. *Flow, Turbulence and Combustion*, 92(1-2): 473–502, 2014.

[48] L. Shemer. Laminar-turbulent transition in a slowly pulsating pipe flow. *Phys. Fluids*, 28(12):3506–3509, 1985.

[49] L. Shemer and E. Kit. An experimental investigation of the quasisteady turbulent pulsating flow in a pipe. *Phys. Fluids*, 27(1):72–76, 1984.

[50] B.A. Singer, J.H. Ferziger, and H.L. Reed. Numerical simulations of transition in oscillatory plane channel flow. *J. Fluid Mech.*, 208:45–66, 1989.

[51] B. Song. *Direct numerical simulation of transition to turbulence and turbulence control in pipe flow.* PhD thesis, Georg-August-Universität Göttingen, 2014.

[52] A. Souma, K. Iwamoto, and A. Murata. Experimental investigation of pump control for drag reduction in pulsating turbulent pipe flow. *Proc. of the sixth international symposium on turbulence and shear flow phenomena*, 2:761–766, 2009.

[53] J.C. Stettler and A.K.M. Hussain. On transition of the pulsatile pipe flow. *J. Fluid Mech.*, 170:169–197, 1986.

[54] S.F. Tardu and G. Binder. Wall shear stress modulation in unsteady turbulent channel flow with high imposed frequencies. *Phys. Fluids A: Fluid Dynamics*, 5(8):2028–2037, 1993.

[55] S.F. Tardu, G. Binder, and R.F. Blackwelder. Turbulent channel flow with large-amplitude velocity oscillations. *J. Fluid Mech.*, 267:109–151, 1994.

[56] D.P. Telionis. *Unsteady viscous flows*, volume 9. Springer, 1981.

[57] J.T. Tozzi and C.H. von Kerczek. The stability of oscillatory hagen-poiseuille flow. *J. Appl. Mech.*, 53(1):187–192, 1986.

[58] S.W. Tu and B.R. Ramaprian. Fully developed periodic turbulent pipe flow. part 1. main experimental results and comparison with predictions. *J. Fluid Mech.*, 137:31–58, 1983.

[59] R. Tuzi and P. Blondeaux. Intermittent turbulence in a pulsating pipe flow. *J. Fluid Mech.*, 599:51–79, 2008.

[60] S. Uchida. The pulsating viscous flow superposed on the steady laminar motion of incompressible fluid in a circular pipe. *Zeitschrift für angewandte Mathematik und Physik ZAMP*, 7(5):403–422, 1956.

[61] C.H. Von Kerczek. The instability of oscillatory plane poiseuille flow. *J.Fluid Mech.*, 116:91–114, 1982.

[62] A.W. Vreman and J.G.M. Kuerten. Comparison of direct numerical simulation databases of turbulent channel flow at reτ= 180. *Phys. Fluids (1994-present)*, 26(1):015102, 2014.

[63] E.L. Yellin. Laminar-turbulent transition process in pulsatile flow. *Circulation research*, 19(4):791–804, 1966.